8-30-2019

On the Pulsed Laser Ablation of Metals and Semiconductors

Todd A. Van Woerkom

ON THE PULSED LASER ABLATION OF METALS AND SEMICONDUCTORS

DISSERTATION

Todd A. Van Woerkom

AFIT-ENP-DS-19-S-030

DEPARTMENT OF THE AIR FORCE
AIR UNIVERSITY

AIR FORCE INSTITUTE OF TECHNOLOGY

Wright-Patterson Air Force Base, Ohio

AFIT-ENP-DS-19-S-030

ON THE PULSED ABLATION OF METALS AND SEMICONDUCTORS

DISSERTATION

Presented to the Faculty

Graduate School of Engineering and Management

Air Force Institute of Technology

Air University

Air Education and Training Command

in Partial Fulfillment of the Requirements for the

Degree of Doctor of Philosophy in Applied Physics

Todd A. Van Woerkom, B.A., M.S.

August 2019

AFIT-ENP-DS-19-S-030

ON THE PULSED ABLATION OF METALS AND SEMICONDUCTORS

DISSERTATION

Todd A. Van Woerkom, B.A., M.S.

Committee Membership:

Dr. Glen P. Perram
Chairman

Dr. Michael A. Marciniak
Member

Lt Col James L. Rutledge, PhD
Member

Dr. Patrick A. Berry
Member

Dr. John R. Bruzzese
Member

Abstract

Pulsed laser ablation is a rich field of research with numerous industrial, academic, and military applications. Decades of research have lead to deep understanding in many application-driven regimes, such as pulsed laser deposition of thin films. Consequently, comparison of ablation effects across disparate experimental regimes can be difficult, and unifying trends can be hidden under regime-specific effects. To attempt to address that problem, the aim of this dissertation is to study pulsed laser ablation over several orders of magnitude in pulse duration, fluence, and material properties. Chapter 1 provides a more detailed picture of the problem space, and Chapter 2 covers the phenomenology of the primary temporal regimes of laser ablation.

In Chapter 3, laser ablation of aluminum, silicon, titanium, germanium, and indium antimonide at 1064 nm in ambient laboratory air with pulse durations ranging from 100 picoseconds to 100 microseconds has been characterized with optical microscopy. Highly focused spots of 10 μm yields fluences of 0.004-25 kJ/cm^2 and irradiances spanning 4×10^6-10^{14} W/cm^2. Single pulse hole depths range from 84 nm to 147 μm. A quasi-one dimensional thermal model establishes a set of non-dimensional variables, h^*, f^*, and t^*, for hole depth, fluence, and pulse duration, respectively. For pulse durations shorter than the radial diffusion time, the hole depth exceeds the thermal diffusion length by a factor of 1 to 30 for more than 90% of the data. For pulses longer than this critical time, transverse heat conduction losses dominate and holes as small as 10^{-3} times the thermal diffusion depth are produced. For all cases, the ablation efficiency, defined as atoms removed per incident photon, is 10^{-2} or less, and is inversely proportional to volume removed for pulse durations less than 100 ns. At high fluences, more than 10-100 times ablation threshold, explosive boiling is identified as the likely mass

removal mechanism, and hole depth scales approximately as fluence to 0.4-0.5 power. The power-law exponent is inversely proportional to the shielding of the laser pulse by ejected material, and shielding is maximum at the 1 ns pulse duration and minimum near the 1 μs pulse duration for each material. Using the thermal scaling variables, the high-fluence behavior for each material becomes strikingly similar.

Chapter 4 builds on the non-dimensional variables from Chapter 3 by exploring shorter pulse durations, lower background pressures, and multi-mode beams. Low transverse order Gaussian beams at 1064 nm wavelength and 28 ps pulse duration were used to ablate Al, Si, Ti, Ge, and InSb in air, and Ge in vacuum. Crater depths and volumes, as well as volume of material above the surface were measured using a laser confocal microscope. Crater depths were found to plateau with increasing fluence on each material, and crater depths on Ge in vacuum were slightly higher than in air. Crater volume above and below the surface was found to increase linearly with fluence for all materials in air. In vacuum, the volume of material above the surface was less than in air, and increased at a lower rate with increasing fluence. The ratio of volume above the surface to volume below the surface was found to plateau for all materials to approximately 0.7 in air, and 0.4 for Ge in vacuum. The ablation efficiency was higher at low fluences, and decreased to approximately 0.004 for all materials at higher fluences. Simulations using the Directed Energy Illumination Visualization (DEIVI) tool showed that bulk melt flow out of the crater caused by the evaporation recoil pressure dominated at higher fluences. Plateauing of crater depth with fluence was caused by melt re-flow into the crater, which effects smaller crater widths more than larger ones, as evidenced by comparing multi-mode results to TEM_{00} simulations. Recondensation of evaporated material was identified as the main difference between craters formed in air versus vacuum, and the Knudsen layer jump conditions in DEIVI were modified to account for an estimated $\approx 20\%$ recondensation rate. The simulations showed a resulting reduction in evaporation, which

created less recoil pressure, driving less melt out of the crater. Higher resolution simulations and additional experimental data comparing different order modes are needed to further explore the effects of diverse spatial fluence distributions.

Finally, Chapters 5 and 6 investigate optical emission spectroscopy from the plume formed during laser ablation of aluminum and titanium. The long pulse ablation of aluminum wafers in ambient air using an Er:YAG laser at 2.94 μm wavelength is presented. Visible emission spectra collected during ablation are assigned to the $B^2\Sigma^+ \rightarrow X^2\Sigma^+$ molecular electronic transition of aluminum monoxide (AlO). A rovibronic model including self-absorption within the plume is developed to determine the molecular temperature. A 60.2 μs pulse at a fluence of 249.92 $\pm$ 40 J/cm^2, a temperature of 2843 $\pm$ 32 K and 3013 $\pm$ 30 K was found with the linear and nonlinear models, respectively. A greybody background, with an emissivity of approximately 1.3×10^{-6} was observed, implying a low volume mixing fraction of particulates in the plume. A linear fit of the $\Delta v = -1$ sequence was developed to rapidly analyze hundreds of spectra taken as a background pressure was varied from 400 mbar to 1000 mbar. The AlO temperature is approximately independent of background pressure. Finally, comparisons to other laser ablation studies at shorter wavelengths and shorter pulse durations are made wherever possible.

Ablation of titanium wafers in air is accomplished with 60-300 μs pulsed, 2.94 μm laser radiation. Titanium monoxide spectra are measured in the wavelength range of 500 nm to 750 nm, and molecular signatures include bands of the $C^3\Delta \rightarrow X^3\Delta$ α, $B^3\Pi \rightarrow X^3\Delta$ γ', and $A^3\Phi \rightarrow X^3\Delta$ γ transitions. The blackbody background signal was found to have a temperature between 2350 K and 2600 K from 1 to 1000 mTorr background pressure. With background pressures $P = 200-1000$ mTorr the total spectrally integrated emission intensity scaled as $P^{1/3}$. The spatially and temporally averaged spectra appear to be in qualitative agreement with previous temporally resolved studies that employed shorter wavelengths and shorter pulse durations than utilized in this work. Simulations in DEIVI

show that peak temperature and pressure in the plume are not sufficient to create significant atomic and ionic emissions seen in such other studies. A peak temperature of approximately 4000 K is inline with molecular temperatures at long time delays as measured by Parigger and Giacomo. A simple chemical kinetics model, using the temperature and evaporated Ti volume from DEIVI predicts temporal behavior of the total TiO emission intensity in ambient air that matches the measured signal relatively well.

Overall, the non-dimensional variables defined in Chapter 3 provide a simple and intuitive description of laser ablation effects covering pulse durations in the tens of picoseconds to the hundreds of microseconds and fluences up to thousands of times the ablation threshold. For a vast majority of the data collected in this dissertation, $f^* \gg 1$ and $t^* \ll 1$ resulted in $h^* \gg 1$, and the simple quasi-one dimensional model collapsed the dissimilar materials to a common trend. Conversely, if either $f^* \lesssim 1$ or $t^* \gtrsim 1$, then $h^* \lesssim 1$ and craters were much smaller in both depth and lateral extent. In this case, the spectroscopic signals measured in Chapters 5 and 6 were correspondingly weaker as well. Taken together, the broad set of experimental conditions studied in this dissertation combined with a simple quasi-one dimensional thermal model provide a more unifying view of pulsed laser ablation than might otherwise be expected.

Acknowledgements

I could not have achieved this without the help of numerous people to whom I will be forever indebted. I would like to thank my advisor, Dr. Glen Perram, for guiding me through my research and teaching me so much. My committee members, Dr. Mike Marciniak, Lt Col James Rutledge, Dr. Patrick Berry, and Dr. John Bruzzese, have provided invaluable contributions, leading me and this dissertation to be more well-rounded. I would especially like to thank Dr. Berry for allowing me to use his lab space in the Sensors Directorate.

I would like to thank my colleagues in the Sensors Directorate, many of whom have become close friends. Charles Phelps helped me overcome many roadblocks in my research by being the ideal technical sounding board. I enjoyed my time collaborating with the RYDH laser guys: Sean McDaniel, Ryan Feaver, Jonathan Evans, Ron Stites, Brad Deshano, Tom Harris, and Gary Cook. I would like to thank Leidos for paying my tuition, and my supervisor, Jim Louthain, for supporting my studies. I'd like to thank Brian Dolasinski for teaching me almost everything I know about lab work. I started at AFIT while working for InfoSciTex, so I would like to thank Mike Gilkey for supporting and encouraging my studies.

I could not have made it this far in life if it weren't for my loving parents and brother. And finally, I'd like to thank my wife and kids for supporting me throughout this endeavor. It has been a lot of work, and they deserve as much credit for this as I do.

Todd A. Van Woerkom

Table of Contents

Page

List of Figures

List of Tables

Symbols

α Absorption coefficient, cm^{-1}

C Specific heat capacity, J/(kg·K)

Δv Change in vibrational energy level associated with molecular electronic transition

η Ablation efficiency, atoms/photon

$f/\#$ f-number of a lens or optical system

f^* Non-dimensional fluence: applied fluence relative to the material's vaporization threshold

F Fluence, $\mathrm{J/cm}^2$

F_{th}, F_m Vaporization threshold fluence and melt fluence, $\mathrm{J/cm}^2$

h Crater depth of damage from single-mode laser ablation, m

h_m Maximum crater depth of damage from multi-mode laser ablation, m

h^* Non-dimensional hole depth: measured hole depth relative to the thermal diffusion length during the laser pulse duration

I Irradiance, $\mathrm{W/cm}^2$

κ Thermal diffusivity defined as $\frac{K}{\rho C}$, m^2/s

K Thermal conductivity, W/(m·K)

λ Wavelength, m

L Thermal diffusion length $\approx \sqrt{\kappa t}$, m

L_m Latent heat of melt or fusion, J/kg

L_v Latent heat of vaporization, J/kg

ρ Density, kg/m^3

P Pressure, Torr, atm, Pa, bar

r Radial coordinate, m

R Surface reflectivity

r_a Condensed matter atomic radius, m

τ_p, t_p Full-width at half-max of laser pulse temporal profile, s

t_ω, t_d Thermal diffusion time of a material relative to a length ω or d, s

T Temperature, K

T_m, T_v, T_c Melt, vaporization, and critical temperatures, K

t^* Non-dimensional time: pulse duration relative to the thermal diffusion time of the laser spot area

V, V_+, V_- Crater volume, volume of crater above surface, and volume of crater below surface, m

ω Spot radius (at $1/e$ point of Gaussian fit to transverse spatial extent) as a function of distance along propagation direction, m

ω_0 Value of ω at focus along direction of propagation, m

z Direction of laser propagation and also depth into material from surface, m

z_R Rayleigh range, m

1. Introduction and Problem Statement

Laser ablation is an incredibly active field, including research in fundamental physics (e.g. non-equilibrium thermodynamics), industrial (e.g. laser peening) and medical (e.g. laser dentistry) applications, and even security and defense applications (e.g. chemical detection and laser lethality). Over such a broad range of applications with varying degrees of precision required, it is often difficult to find unifying trends that allow researchers and practitioners to understand and compare effects across disparate physical regimes. Furthermore, differences in research goals, experimental apparatus, and theoretical approaches create barriers to creating a broad physical intuition capable of translating results from study to study. To that end, the fundamental goal of this dissertation is to build from a broad set of experimental and theoretical data to a narrower set of scaling relations, heuristics, and trends that provide a roadmap for understanding laser ablation across relevant regimes. Specifically, the objective is to quantify the effects of ablation including: crater morphology, ablation efficiency, and plume spectral emissions across metals and semiconductors using pulse durations spanning picoseconds to microseconds and fluences from ones to thousands of J/cm^2.

The laser ablation problem can be broken down into three independent groups of variables describing the laser, material, and environmental conditions. Key laser parameters are wavelength, pulse duration, pulse energy, and spot size. The primary material variables are the bulk optical and thermochemical properties. Environmental conditions of interest are the sample temperature, the interface conditions, and the background pressure above the sample.

For the purposes of this dissertation, the primary wavelength of interest is 1064 nm. This is due to the large body of literature available at this wavelength and the plethora of affordable optical equipment. While there is substantial literature on ultraviolet (UV) laser ablation as well, the results at 1064 nm are more easily translatable to longer wavelengths. This is because UV laser ablation involves significant photoionization of the plume, whereas the effect is much reduced at 1064 nm. Thus, interpreting results at longer wavelengths is more straight forward due to the laser-plume interaction consisting of mostly the same physical processes. Another reason is that mass removal is primarily thermal at longer wavelengths, where a photon is absorbed by an electronic state in the material that couples to a lattice vibration thereby raising the macroscopic temperature. Ultraviolet ablation often involves direct ejection of surface electrons (i.e. the photoelectric effect) that remove mass by Coulombic attraction with positive ions left behind.

The primary pulse durations of interest in the present study are 10's of picoseconds (ps) to 100's of microseconds (μs). Similar to the choice of wavelength, this is to narrow down the space to include only the processes which are "similar" enough to be able to meaningfully compare. While the goal of this dissertation is to create ways to interpret ablation effects across these wildly different regimes, some lines have to be drawn in order to derive tools simple enough to be of actual use. For that reason, femtosecond (fs) or ultrashort laser ablation is not included in this effort. Below the 10's of ps, the laser-material interaction is entirely different, and the laser-plume interaction is completely absent. Furthermore, there is extension published research on continuous wave (CW) laser ablation, especially in the laser welding and laser lethality communities. No attempt is made to include CW effects in the heuristics developed in this dissertation; there is enough physics in the 7+ decades of pulse duration between 100 ps and 100 μs.

Pulse energy and spot size are mainly combined to create fluence, but ablation ef-

fects do not just depend on fluence. As will be seen in Chapter 3, the fluence needs to be applied fast enough for mass removal to occur. And Chapter 4 will show that the spot size really does effect ablation, even if the fluence is the same. In this dissertation, pulse energies on the order of 10's of micro Joules (μJ) to 100's of milliJoules (mJ) are of interest. Only at the shortest pulse durations can μJ cause significant mass removal, and as pulse durations enter the ms regime, Joules of energy are typically required. The spot size (typically defined as the $1/e$ point of a Gaussian intensity or fluence distribution, which will be more rigorously defined as applicable in each chapter) is generally between 10 μm and 100's of μm. Smaller spot sizes make direct measurement of the intensity profile difficult, as well as complicate the damage measurements. Larger spots are not of interest mainly because the fluence would end up being too low to cause significant mass removal. The numerical aperture is also an important laser parameter, but it affects the laser-plume interaction more than crater formation in general. The experiments in this dissertation all use relatively low f/# lenses, but there is no direct comparison of different numerical apertures under otherwise identical conditions.

There are myriad parameters to describe a given material, so, again, a line has to be drawn somewhere. For this dissertation, thermochemical properties are of interest because they relate to phase change. The thermal ablation process includes the material changing from solid to liquid to gas, so any description must include (or at least mention) heat of fusion and heat of vaporization. Primarily, macroscopic properties (e.g. density, thermal conductivity, heat capacity, etc.) are pertinent to this effort, and quantum mechanical or electronic properties, are not. For example, crystal structure and electronic energy levels are beyond the scope of this dissertation. The thermochemical properties provide a way to compare laser characteristics relative to each material. For example, the laser fluence required to cause melting can be compared across each material, which can help with interpreting and presenting results across diverse materi-

als and laser conditions. Additionally, mechanical properties are not included, although some "mechanical" ablation effects, such as spalling or cracking, can occur primarily at ps or shorter time scales. Moreover, optical properties (absorption coefficient and reflectivity, specifically) are of interest as nominal discriminators between materials. For example, 1064 nm is approximately in band on germanium, but highly reflected by metals such as aluminum. Thus, the optical properties *at a particular laser wavelength* are of interest, and combining materials and wavelength creates a sort of contour in the problem space. This hints at the main purpose of the dissertation: to compare effects across disparate physical regimes, e.g. how does 1 μm ablation of germanium compare to 4 μm ablation of indium antimonide?

The environmental conditions are last, but not least. While the sample temperature is technically a state of the material, it is treated in this dissertation as an environmental condition since it is externally controlled as an independent variable. Temperatures of interest are from cryogenic (i.e. 77 K) to near the melting temperature of the material being studied. For practical purposes, experimental apparatuses have a limited range of operating conditions, and the highest temperature consistently available is approximately 700 K. The physical interface condition in this dissertation is the material in air (or vacuum), with no forced air flow over the sample, and the sample oriented with its surface normal parallel to the ground. Laser ablation of solids submersed in liquid is an active field of research, but not considered here. Ablation of layered materials, or ablation occurring at the interface between two solid materials is also beyond the scope of this dissertation. However, even just considering a material in air (or some gas) encompasses a wide range of phenomena. Chapter 2 will discuss this more, but consider an evaporated aluminum atom ($\approx$ 27 AMU) colliding with a 1 atmosphere (atm) background of diatomic nitrogen ($\approx$ 28 AMU) versus a 10^{-3} atm background of diatomic helium ($\approx$ 8 AMU). The background gas of interest is normal air, e.g. not an inert gas, with

pressures between approximately 10^{-9} atm ($\approx 10^{-6}$ Torr and $\approx 10^{-4}$ Pascal) and ambient air pressure. Thus ultra high vacuum and ablation in pressurized backgrounds are not included in this dissertation.

The format of this dissertation is as follows: Chapter 2 is an overview of the various physical regimes of laser ablation applicable to this dissertation. High-level phenomenology is discussed and results from subsequent chapters are previewed. A detailed literature review of relevant prior work is presented in each chapter as needed. Chapter 3 covers the largest single experiment of this dissertation, which was the laser ablation of 5 different materials at 7 pulse durations and 7 different fluence levels. Chapter 4 presents a laser ablation experiment that builds on Chapter 3 by going to a shorter pulse duration and using a more complex spatial fluence distribution. While the experiment covered in Chapter 3 is done in ambient air, Chapter 4 investigates background pressure effects from 10^{-6} to 760 Torr. Chapters 3 and 4 have not been published yet, but are ready to be submitted to a peer-reviewed journal. Chapters 5 and 6 cover aluminum monoxide and titanium monoxide emission spectroscopy of the plume, respectively. Chapter 5 was presented as a poster by Dr. Glen Perram at the 2018 High Power Laser Ablation Conference, and was published as a paper in the Journal of the Optical Society of America B in October 2018. Parts of Chapter 6 were presented as a poster at the 2018 International Conference on Spectroscopic Lineshapes by Dr. Christian Parigger, and is expected to be published in the associated conference proceedings. A poster comparing aluminum and titanium emission spectroscopy was accepted to the 2018 SciX Conference, but was not presented due to scheduling conflicts. Chapter 7 concludes the dissertation and discusses potential future research directions building on this work. Finally, while Chapters 3-6 are going to be published or already have been published with co-authors, Mr. Van Woerkom is the primary author and principal investigator on all of them.

2. Ablation Phenomenology

There are myriad physical processes involved in laser ablation, which can typically be discussed in terms of the dominant effects in a particular temporal regime. The purpose of this chapter is to present a mostly qualitative overview of the temporal regimes relevant to this dissertation and discuss how the effects within those regimes change as a function of laser parameters and material conditions. The figures are from experiments performed as a part of this dissertation, and the descriptions of various physical effects are cited as appropriate. Figure 1 shows the temporal regimes of pulsed laser ablation using damage images observed in this work. The fluence was approximately 15 kJ/cm^2 at each pulse duration, resulting in an irradiance, $I \approx 10^8 - 10^{14}$ W/cm^2.

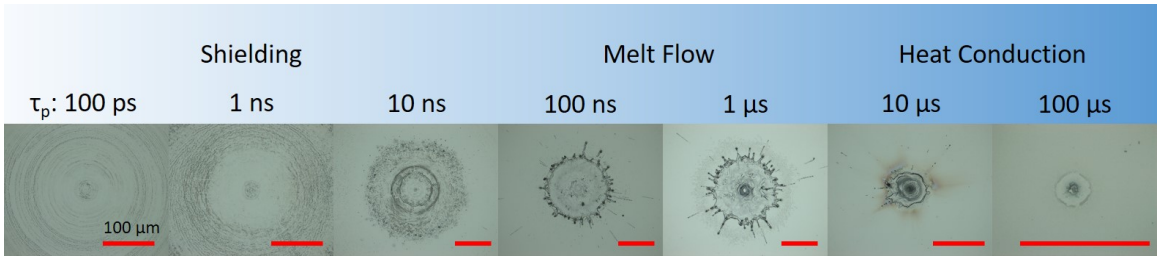

Figure 1. Examples of dominant phenomenological temporal regimes in laser ablation. $\lambda = 1064$ nm, τ_p: varied, $\omega_0 \approx 10$ μm, $F \approx 15$ kJ/cm^2, Material: Ge, $P = 1$ atm, $T = 300$ K. Red bars are 100 μm length in each image.

The optical images of damage effects are taken from laser ablation of Ge in air at 1064 nm wavelength with s spot size of 10 μm (unless otherwise stated, wavelength is 1064 nm and the spot size for all cases discussed in this chapter is 10 μm). The laser pulse duration, τ_p, is taken as the full-width half-max (FWHM) of the temporal profile. The details of that experiment are in Chapter 3. The red bar in each image is 100 mum, and the dominant physical processes are listed at the top. For the purposes of the following discussion, the pulse durations of interest are between 100 picoseconds (ps) and 100 microseconds (μs). The occurrence of ablation depends on both the energy incident on

the surface and the timescale over which it is applied. To facilitate direct comparison, the fluence values here are nearly the same at each pulse duration, so that the discussion is more focused on the temporal aspects of ablation.

2.1 Shielding Regime

Shielding in this context is typically defined as significant laser energy being absorbed by the plume of ejected material, and manifests itself in damage effects by a plateauing of crater depth with increasing fluence[1]. The plume typically consists of atomic and ionic species early in its evolution, where high temperatures ($> 10^4$ K) and pressures ($> 10^9$ Pa) in the shock front prevent molecule formation[1]. The plume becomes ionized either by photoionization or collisions between the ejected atoms and the background gas[2]. Photoionization dominates at shorter wavelengths, e.g. ultraviolet, whereas collisional ionization occurs more at longer wavelengths where it would take many photons to ionize an atom in the plume[2].

Laser light is absorbed in the plume by inverse Brehmsstrahlung absorption, which has a cross section that scales as λ^3, and thus affects infrared light more than ultraviolet[2]. In some cases, however, the elctron density is lower after ablation with longer wavelengths, which would decrease the amount of laser enrgy absorbed in the plume[3]. The absorption of laser light by the plume can increase the kinetic energy of the plume, resulting in very high (Mach 40) forward-directed (i.e. towards the laser source) streaming speeds, and increased lateral expansion[1]. In the shielding regime, additional pulse energy gets absorbed in the plume, rather than removing more mass[4]. Shielding occurs in vacuum and at ambient background pressure, and the higher pressure confines the plasma at the surface, thus increasing the laser-plasma interaction[5].

Figure 2 shows craters formed in the present study on Si (for reference, Figure 1 showed ablation of Ge) with fluences from $\approx 0.03 - 15$ kJ/cm^2 in the shielding regime. As

can be seen, the lateral extent of surface damage, most of which is superficial, is almost 2000 μm, or 2 mm, in diameter for the highest fluence. The extent of the central feature, i.e. the crater, remains approximately the same, while the hole depth grows slightly. The surface damage shows virtually no signs of melt displacement, and re-deposited (or re-condensed) material appears to have been in the vapor phase.

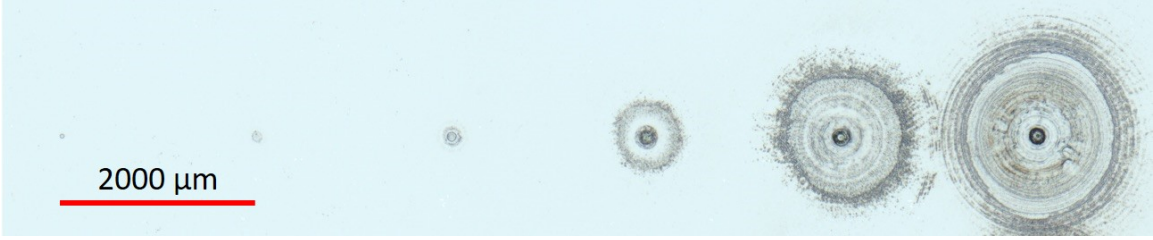

Figure 2. Craters from laser ablation in the shielding regime. $\lambda = 1064$ nm, $\tau_p = 100$ ns, $\omega_0 \approx 10$ μm, F: varied, Material: Si, $P = 1$ atm, $T = 300$ K.

At the high irradiances caused by short pulse laser ablation, structural effects, such as cracking can occur as shown in Figure 3.

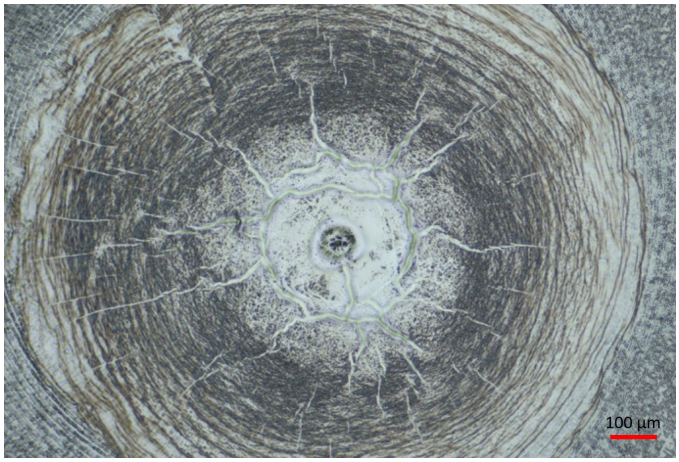

Figure 3. Structural cracks formed on InSb in the shielding regime. $\lambda = 1064$ nm, $\tau_p = 1$ ns, $\omega_0 \approx 10$ μm, $F \approx 3$ kJ/cm^2, Material: InSb, $P = 1$ atm, $T = 300$ K.

Chapter 3 will show that shielding effects peak in the 1-100 ns regime, and fall off dramatically on either side. At shorter pulse durations, the pulse is largely over before

the highly absorbing plume is formed[6]. For longer pulse durations, if the pulse energy is held constant, the intensity can be insufficient to evaporate and ionize significant material during the pulse[7]. In the shielding regime, the plume content is almost entirely atomic and ionic species, dominated by continuum emissions at short time delays after ablation[8]. At longer time delays (tens of microseconds) when the plume temperature decreases, molecules can form, and if there is oxygen in the background gas, oxides can form as well[8]. Temporally- and spatially-resolved emission spectroscopy of the plume (see [9, 10, 11]), as well as plume imaging (see [12, 13, 14]), provide details of the plume evolution in the shielding regime.

2.2 Melt Flow Regime

As the pulse duration increases into the hundreds of nanoseconds, a significant portion of the laser pulse interacts with liquid phase material, and bulk melt flow effects can become significant[1]. Figure 4 shows crater scaling with increasing fluence in the present study.

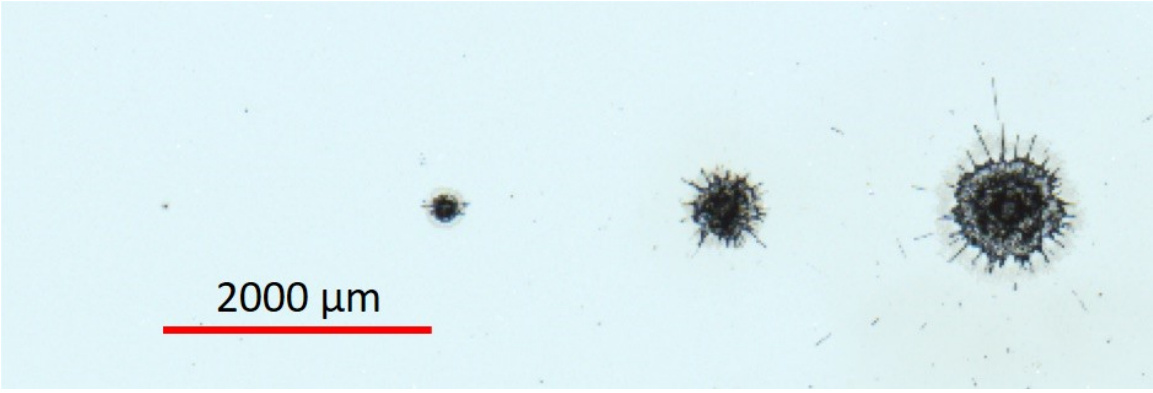

Figure 4. Craters from laser ablation in the melt flow regime. λ = 1064 nm, τ_p = 1 μs, $\omega_0 \approx$ 10 μm, F: varied, Material: Si, P = 1 atm, T = 300 K.

In the melt flow regime, as the fluence is increased, the evaporation rate increases, which in turn increases the recoil pressure on the melt layer, driving bulk flow[1]. At very

high fluences, significant melt ejection and splatter can occur[1]. Figure 5 shows such effects on InSb after laser ablation with a 100 ns pulse, where the spot size was again approximately 10 μm, and the overall image is approximately 456 μm across.

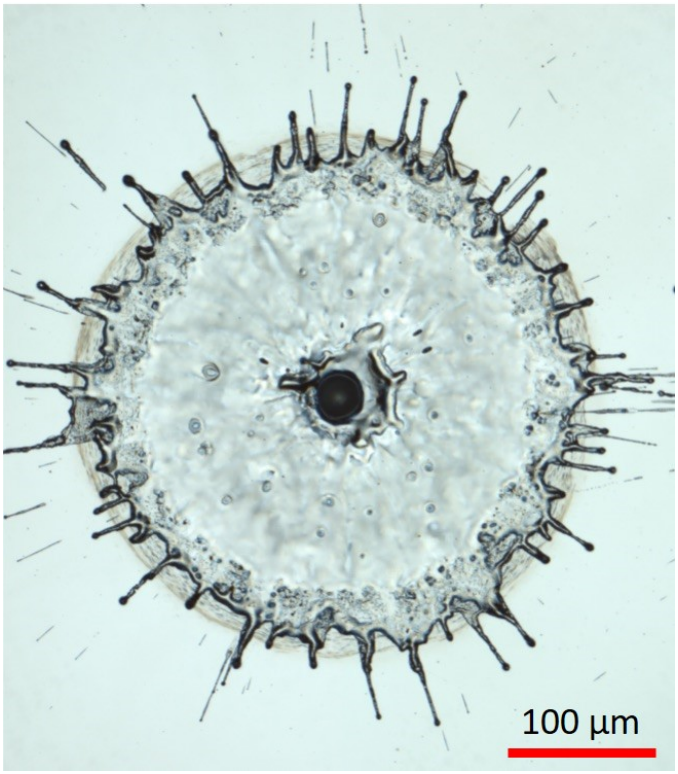

Figure 5. Significant splatter in the melt flow regime. $\lambda = 1064$ nm, $\tau_p = 100$ ns, $\omega_0 \approx 10$ μm, $F \approx 3$ kJ/cm^2, Material: InSb, $P = 1$ atm, $T = 300$ K.

The interconnected effects of recoil pressure and melt displacement can cause significant crater formation long after the pulse has ended[1]. It will be shown in Chapter 3 that the melt flow regime of laser ablation is where the largest craters are formed in this study. At shorter wavelengths on metals, the absorption coefficient, α, can be as high as 10^6 cm^{-1} or more, and the laser light will be absorbed more at the surface which can cause more efficient evaporation[15]. Semiconductors, however, can be weakly absorbing over a large wavelength range and strongly absorbing near their bandgap[16]. Thus, the optical properties of the material affect how deep the laser energy is deposited, and

determines whether the heat source is treated as a boundary source (i.e. applicable to metals) or a volume heat source (i.e. more applicable to dieletrics and semiconductors)[17]. However, even at slightly elevated temperatures, most semiconductors have additional absorption processes, such as free-carrier absorption, that rapidly increase the coupling of laser light to the material[16]. So the absorption coefficient must be considered with wavelength and temperature dependence when interpreting experimental results.

In the melt flow regime, there is still a plume of ejected material, though typically not as hot or highly ionized as in the shielding regime. Streaming speeds can still be large since laser energy will likely be absorbed at the shorter pulse durations and higher fluences, but not as high as the shielding regime. The atomic and ionic signals are less than those in the shielding regime, and molecular plume content can form more easily due to the lower temperatures and slower streaming speeds. The same spectroscopic and imaging techniques can be used in this regime to characterize the plume evolution.

2.3 Heat Conduction Regime

At pulse durations long compared to the thermal timescale of the material ($\tau \approx L^2/\kappa$, where L is a characteristic length and κ is the thermal diffusivity), significant energy is lost to heat conduction[1]. While the melt volume can still be significant, evaporation is reduced, and therefore recoil-pressure-induced melt displacement is correspondingly subdued[1]. Figure 6 shows craters from this study with increasing fluence in the heat conduction regime. In this regime, since the material has time to conduct the laser energy away as heat, craters scale poorly with fluence under most conditions[1]. Figure 6 shows 10 μs ablation on Si, with no visible melt flow effects. However, the amount of melt displacement also depends strongly on material parameters. At a constant irradiance, the melt displacement effects would be more significant on InSb than Si, even in the heat conduction regime, due to its lower melt temperature and lower heat of fusion.

Figure 7 shows melt effects on InSb when the pulse is long compared to the thermal diffusion timescale.

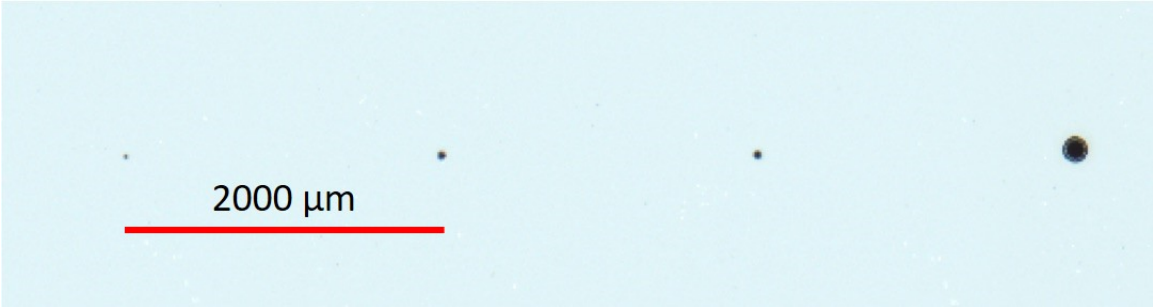

Figure 6. Craters from laser ablation in the heat conduction regime. $\lambda = 1064$ nm, $\tau_p = 10$ μs, $\omega_0 \approx 10$ μm, F : varied, Material: Si, $P = 1$ atm, $T = 300$ K.

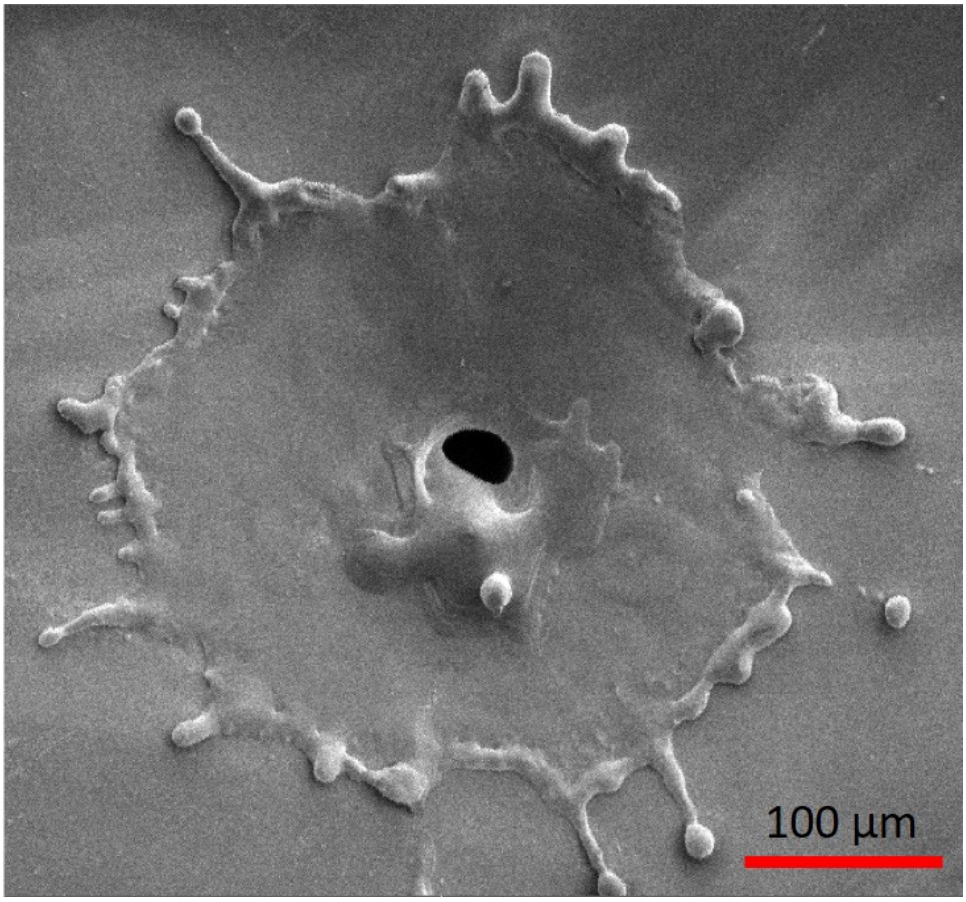

Figure 7. Melt flow effects in the heat conduction regime. $\lambda = 1064$ nm, $\tau_p = 10$ μs, $\omega_0 \approx 10$ μm, $F \approx 17$ kJ/cm^2, Material: InSb, $P = 1$ atm, $T = 300$ K.

This scanning electron microscope (SEM) image of InSb shows considerable melt effects, some of which flowed back into the crater. It will be shown in Chapter 4 that melt re-flow into the crater can cause diminishing hole depth with increasing fluence. Another notable effect that can occur in the heat conduction regime is extrusion formation due to the thermocapillary effect[1]. Figure 8 shows such an extrusion formed in this work on Ge at a fluence of 3 kJ/cm^2.

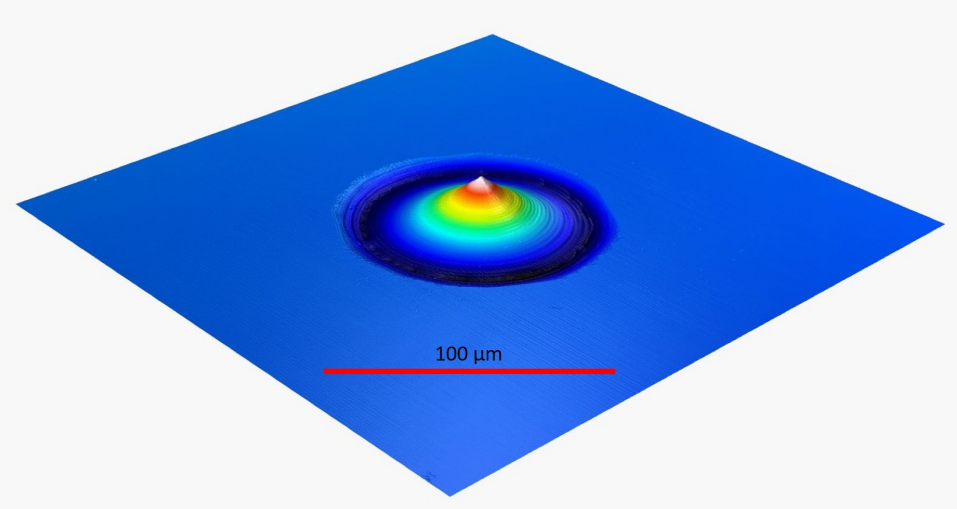

Figure 8. Extrusions formed during laser ablation in the heat conduction regime. $\lambda = 1064$ nm, $\tau_p = 100$ μs, $\omega_0 \approx 10$ μm, $F \approx 3$ kJ/cm^2, Material: Ge, $P = 1$ atm, $T = 300$ K.

Similar extrusions are seen on materials with liquid phase densities higher than their solid phase density. As the molten material cools, it expands up out of the surface[1]. In the heat conduction regime, there is often a very weak or non-existent plume, due to less evaporation occurring. It will be seen in Chapters 5 and 6 that aluminum monoxide (AlO) and titanium monoxide (TiO) emissions can still be seen while there is little to no evidence of atomic or ionic emissions, suggesting comparatively lower plume temperatures and pressures. In this regime, the signal is often too weak for spatially or temporally resolved measurements, so average measurements are necessary to study the plume. Unfortunately, average measurements do not provide the same quality and

quantity of insights as the resolved measurements that can be made in the shielding and conduction regimes.

2.4 Spatial and Temporal Beam Shape

To end this chapter, a brief discussion of the beam profile is necessary. Typically laser ablation or laser-induced breakdown spectroscopy experiments use a Gaussian profile in both space and time[1, 8]. Gaussian temporal profiles are common in many laser systems, such as the ubiquitous Q-switched Nd:YAG, and a reasonable approximation of hyperbolic secant profiles that can be produced by mode-locked lasers[18]. However, some laser systems, such as flashlamp-pumped Er:YAG, have very non-Gaussian temporal distributions that can complicate attempts to compare results to other damage experiments[19]. Other Q-switched and gain-switched laser systems can exhibit the classic giant pulse temporal profile which begins with a large narrow spike followed by a much longer envelope of relaxation oscillations[20]. Again, care must be taken to compare ablation results between lasers with dramatically different temporal profiles.

Spatial beam profiles require the same attention. Often only the spot size is given, and that is not always a commonly agreed-upon parameter[18]. For example, the spot size can refer to the half width at the $1/e$ point of a Gaussian fit to the spatial intensity profile (the approach this dissertation will mostly use), or it can refer to the $1/e^2$ point. Non-Gaussian spatial distributions can often be approximated by a Gaussian, with most of the deviation occurring in the tails[21]. Typically a Gaussian TEM_{00} mode will have a higher peak fluence than multi-mode or non-Gaussian fluence distributions, resulting in narrower craters[22]. The spatial distribution of laser energy can induce complicated melt flow effects, even if the pulse duration is short, as will be seen in Chapter 4.

3. Laser Ablation of Metals and Semiconductors with 100 ps to 100 μs Pulses

Laser ablation of aluminum, silicon, titanium, germanium, and indium antimonide at 1064 nm in ambient laboratory air with pulse durations ranging from 100 picoseconds to 100 microseconds has been characterized with optical microscopy. Highly focused spots of 10 μm yields fluences of 0.004-25 kJ/cm^2 and irradiances spanning 4×10^6-10^{14} W/cm^2. Single pulse hole depths range from 84 nm to 147 μm. A quasi-one dimensional thermal model establishes a set of non-dimensional variables for hole depth, fluence, and pulse duration. For pulse durations shorter than the radial diffusion time, the hole depth exceeds the thermal diffusion length by a factor of 1 to 100 for more than 90% of the data. For pulses longer than this critical time, transverse heat conduction losses dominate and holes as small as 10^{-3} times the thermal diffusion depth are produced. For all cases, the ablation efficiency, defined as atoms removed per incident photon, is 10^{-2} or less, and is inversely proportional to volume removed for pulse durations less than 100 ns. At high fluences, more than 10-100 times ablation threshold, explosive boiling is identified as the likely mass removal mechanism, and hole depth scales approximately as fluence to 0.4-0.5 power. The power-law exponent is inversely proportional to the shielding of the laser pulse by ejected material, and shielding is maximum at the 1 ns pulse duration and minimum near the 1 μs pulse duration for each material. Using the thermal scaling variables, the high-fluence behavior for each material becomes strikingly similar.

3.1 Introduction

Laser ablation has been an intense area of research for over 40 years, with applications including materials processing, thin film deposition and characterization, space debris remediation, and optical component damage testing[23, 24, 25, 26, 27]. Most of

the recent research has utilized short wavelengths (<1064 nm) and short pulse durations < 100 ns. Depending on experimental conditions, mass removal may occur via several different mechanisms, including normal evporation, direct ion and electron emission, or explosive boiling. Normal evaporation occurs when the energy deposited is sufficient to raise the temperature of the material to the boiling temperature. At moderate fluence, $< 10\,J/cm^2$, nanosecond pulses lead to electron and positive ion emission[28]. This electronic ablation mechanism can delay the onset of thermal effects, leading to a dynamic ablation threshold[28]. In contrast, explosive boiling or the phase explosion mechanism, induces sample transparency and leads to a deeper, superheated layer, droplet formation, and significantly greater mass removal.

The threshold for explosive boiling is considerably higher than typical ablation conditions, occuring at 440 J/cm^2 in Si for a 355 nm, 44 ns laser (11.5 GW/cm^2)[29], and at 66 J/cm^2 in Si for a 266 nm, 3 ns laser (22 GW/cm^2)[30]. Phase explosion has also been observed at a considerably lower threshold, for example, in Al at 5 J/cm^2 for a 1064 nm, 5 ns laser (1 GW/cm^2)[31], matching computational efforts [32, 33], and in graphite, niobium and YBCO at 15-22 J/cm^2 for a 1064 nm, 3 ns laser (5-7GW/cm^2)[34]. The threshold fluence probably depends on pulse duration and wavelength, increasing at longer wavelengths and longer pulse durations[35, 36]. For example, explosive boiling has not been observed in Si at 1064 nm for fluences as high as 40 J/cm^2[35]. Material ejected during explosive boiling in Si occurs near the critical temperature[31, 35]. Explosive boiling in titanium has been investigated at irradiances between 1.397 and 1.450 GW/cm^2, finding that droplet size and ejected distance both increased with increasing pulse durations from 200 to 250 ns[37].

The ablation process of converting incident photons to ejected atoms is inefficient. Bauer, et al. showed that the ablation efficiency, defined as photons/atom, was 35-170 for UV ablation of Ti at 25 ns pulse duration[5]. Even at low fluences above the ablation

threshold, significant shielding of the laser due to ejected material can occur, and additional laser energy primarily goes into the initial shock front energy and velocity [14]. At fluences as high as 2000 J/cm^2, ablation efficiency, defined as the hole volume relative to the laser pulse energy, μm^3/J, of picosecond and nanosecond Nd:YAG lasers on aluminum increased as wavelength decreased[36]. That study also showed that the hole depth saturated with fluence, but the hole volume grew linearly.

Substantial modeling efforts have tried to capture the diverse physical processes present during laser ablation. For example, Zhang, et al. showed that phase explosion is the dominant mass removal mechanism in aluminum ablation by 1064 nm 5 ns pulses at fluences above 10 J/cm^2[33]. Furthermore, plasma shielding plateaus as fluence increases, and that the ablation rate (ablation depth per pulse) increases as background pressure decreases[33]. For silicon ablation, Bulgakova et al., demonstrated that reflectivity decreased with increasing fluence, heat conduction losses decreased with increasing fluence, and the energy absorbed by the plume eventually plateaus as a function of fluence[4]. Coupling the melt-phase flow and plume expansion dynamics provides a useful tool to augment experimental investigations[38].

Most of the prior work is performed on a single material, with few comparisons across metal and semiconductor materials in a single apparatus. Aluminum and silicon have been studied extensively from a mass removal and hole depth perspective. Numerous studies have investigated aluminum combustion and aluminum monoxide emissions during laser ablation[39, 40] including Chapter 5 of this dissertation. Titanium ablation research has been conducted primarily as a means to study titanium monoxide emissions[41]. Bartoli et. al. studied thermal-based ablation of semiconductor materials and developed an extensive model that has been anchored with a few specific experimental data points[17, 42]. The theoretical and measured damage thresholds for germanium and silicon matched very well at 0.69 μm and 1.06 μm wavelength[42]. The

Bartoli model and experiments also do not predict or discuss mass removal and mass re-deposition effects, and specifically that model does not include explosive boiling.

This experiment aims to investigate laser ablation for pulse durations of 100 ps to 100 μs on aluminum, silicon, germanium, titanium, and indium antimonide at a wavelength of 1064 nm. The materials were chosen to provide a comparison of metals (aluminum and titanium) to indirect semiconductors (silicon and germanium) to direct and compound semiconductors (indium antimonide) spanning a wide variety of material thermal and optical properties. A wide range of irradiances, 4×10^4 to 4×10^{14} W/cm^2, is enabled by a variable pulse duration, excellent beam quality Nd:YAG laser. We seek an appropriate choice of non-dimensional scaling factors to describe laser ablation across diverse materials and experimental conditions.

3.2 Apparatus and Methodology

The experimental setup and representative beam profile is shown in Figure 9. A Spectral Energies QuasiModo laser operating at 1064 nm was used to ablate the samples because of its unique capability of providing continuously varied pulse durations from 100 picoseconds to 100 microseconds [43]. The laser consists of a quasi-continuous wave (CW) source (Figure 9(a)), with portions of the desired pulse duration picked using an electro-optic modulator (EOM) in an arbitrary waveform generator (Figure 9(b)). The pulse is then sent through a diode-pumped amplifier bank (Figure 9(c)) consisting of two single-pass diode-pumped amplifier stages and one double-pass amplifier. Finally, the beam is focused through a pinhole in a vacuum cell to maximize beam quality. The temporal pulse shapes are Gaussian, with the duration being defined as the full-width at half-maximum (FWHM), and typical shot-to-shot variation in pulse duration was less than 1% for all configurations. The pulse energy from the laser was a constant 100 mJ. Fluence on the sample was controlled by two half waveplates on rotation stages

and polarizing beamsplitting cubes (Figure 9(d)), providing a dynamic range of over 10^3. The pulse energy at the sample was measured and averaged over many pulses to get the pulse energy as a function of angle of the half waveplates. A 50.8 mm diameter, 60 mm focal length lens (Figure 9(e)) was used to focus the beam onto the sample mounted on a 3-axis MTN stage system from Newport (Figure 9(f)). The spot size, defined here as the half-width at the 1/e point of a Gaussian fit of the measured spatial beam profile (in x and y), was measured at the sample location (in z) with a pinhole. A full 3-dimensional beam profile was measured to characterize the spot size as a function of focus (Figure 9(g)). The beam quality is good, with $M^2 \approx 1.6$ or better. The spot size was the smallest at 8.8 μm for the 100 μs configuration, and the largest at 11.3 μm at the 10 ns configuration, with no clear dependence on pulse duration. Typical measurement uncertainty in the spot size was 1 μm.

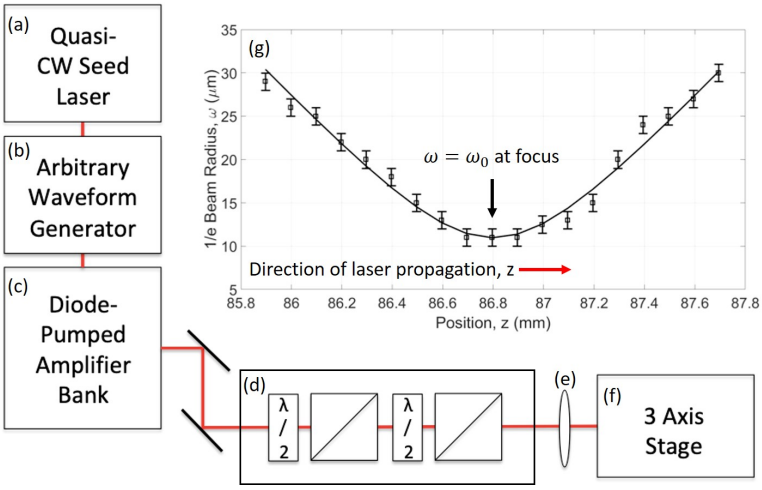

Figure 9. Experimental setup and representative spatial beam profile

The aluminum, titanium, silicon, and germanium wafers were 25.4 mm diameter and 0.5 mm thick, with single-side polished from MTI Corp. The indium antimonide wafers were the same dimensions, but purchased from University Wafer. Each sample was ablated with one shot per test site. A row of shots for each test case (e.g. pulse energy and pulse duration) was performed to provide statistical significance to the hole

measurement. The post-ablation samples were analyzed with a Zeiss laser confocal microscope, with better than 10 nm accuracy and sub-micron repeatability in the vertical and lateral directions.

3.3 Results

Figure 10 shows an example laser confocal microscope image of laser damage on germanium with a 60 mJ pulse and a pulse duration of 1 μs. With a spot size (defined as the half-width at the 1/e point of a Gaussian fit of the spatial beam profile) of 10.9 μm, this corresponds to a fluence of 16 kJ/cm^2 and an irradiance of 16 GW/cm^2. Images like this were taken at 5 locations in each row of damage spots on each material. The high lateral and vertical resolution and multiple objectives of the laser confocal microscope enables the accurate measurement of not only hole depth, but also crater width, volume, and splatter and material redeposition at distances up to 800 μm from the laser spot center. Crater features varied significantly over the experimental conditions. Low fluence shots for each pulse duration created shallow craters (typically 1 μm or less) whose spatial extent approximately matching the radial beam profile. Pulse durations less than 10 ns showed very little splatter, while for longer pulse durations, splatter features increased dramatically in both volume and distance from center spot. Some shots showed evidence of phase explosion, which includes rough craters with peaks and valleys and redeposited droplets[30, 44].

From the laser confocal image, depth profiles were determined as shown in Figure 11. The crater depth is the minimum value of h, and the crater volume is the volume below the $h = 0$ line. For the 1 μs case on Ge shown in Figure 10, the crater depth is 21.26 μm and the crater volume is almost 81,000 μm^3. For comparison, the 13.99 J/cm^2 10 ns case on Ge produced a crater depth and volume of 1.12 μm and 266 μm^3, respectively.

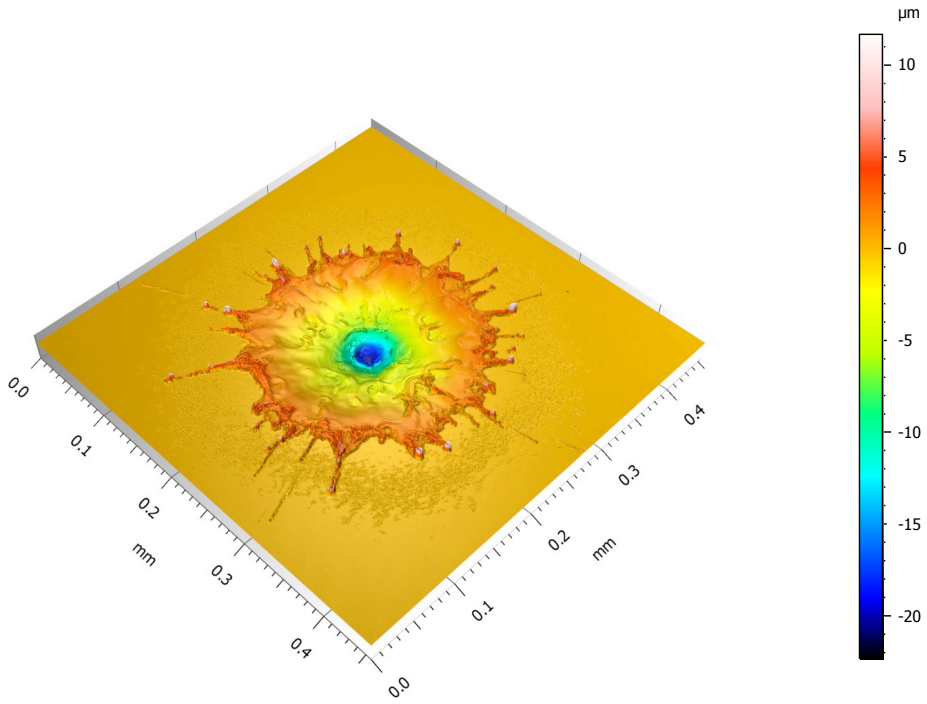

Figure 10. Laser confocal microscope image of laser-induced damage. $\lambda = 1064$ nm, $\tau_p = 1$ μs, $\omega_0 \approx 10$ μm, $F \approx 16$ kJ/cm^2, Material: Ge, $P = 1$ atm, $T = 300$ K.

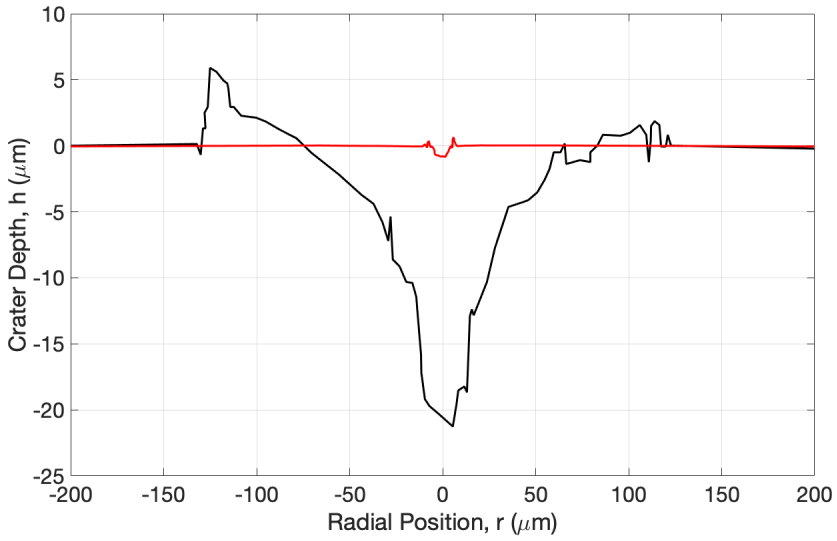

Figure 11. Depth profile of laser-induced damage. $\lambda = 1064$ nm, (-) $\tau_p = 1$ μs and (-) $\tau_p = 10$ ns, $\omega_0 \approx 10$ μm, (-) $F \approx 16$ kJ/cm^2 and (-) $F \approx 14$ J/cm^2, Material: Ge, $P = 1$ atm, $T = 300$ K.

Typical statistical uncertainty from averaging maximum hole depth of multiple shots

was < 10%. The two main sources of error in fluence were uncertainty in the spot size, and the z location of the target. The three-axis stages had a bidirectional position uncertainty of less than a micron. For a spot radius of 10 μm, this led to an approximately 10% uncertainty in spot radius, or a 20% uncertainty in fluence (neglecting pulse-to-pulse energy jitter of < 1%). Gaussian beam propagation with $M^2 = 1.6$, $\lambda = 1064$ nm, and an effective $f/\# = 1.7$ yields a predicted diffraction-limited spot size of 2 μm and a Rayleigh range of $z_R = 25$ μm. A deviation in focus of $\Delta z = 10$ μm increases the spot size by nearly 10%.

3.3.1 Crater Depth

Figures 12-16 show the hole depth for aluminum, silicon, titanium, germanium, indium antimonide, and aluminum, respectively. For all cases, the wide variation and sparseness in ablation conditions preclude a careful examination of the ablation threshold (either for normal ablation or explosive boiling). Hole depths on Al ranged from 861 nm at a fluence of 126.9 J/cm^2 and a pulse duration of 9.3 ns to 76.78 μm at a fluence of 16.1 kJ/cm^2 and pulse duration of 1 μs. Low fluence shots at all pulse durations showed signs of slight melt displacement and resolidifcation. Higher fluence shots in the 100 ns and 1 μs cases showed significant melt displacement up to 100 μm from the center. The 10 μs shots showed less melt displacement, but several large droplets re-solidified less than 50 μm from crater center. Lutey found that the threshold for explosive boiling increased approximately as the square root of pulse duration between 1 and 20 ns[32]. Assuming the trend holds to even longer pulse durations, the threshold for explosive boiling at 1 μs would be less than 100 J/cm^2, so most of the data presented here likely corresponds to explosive boiling.

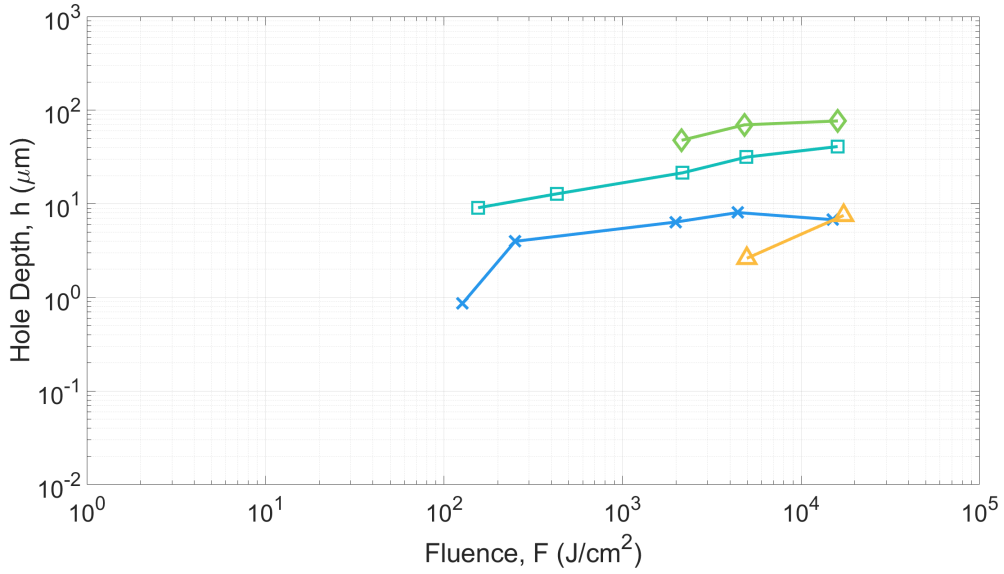

Figure 12. Hole depth from laser ablation with $\lambda = 1064$ nm, $\tau_p = 10$ ns (X), 100 ns (□), 1 μs (◊), 10 μs (△), $\omega_0 \approx 10$ μm, F : varied, Material: Al, $P = 1$ atm, $T = 300$ K

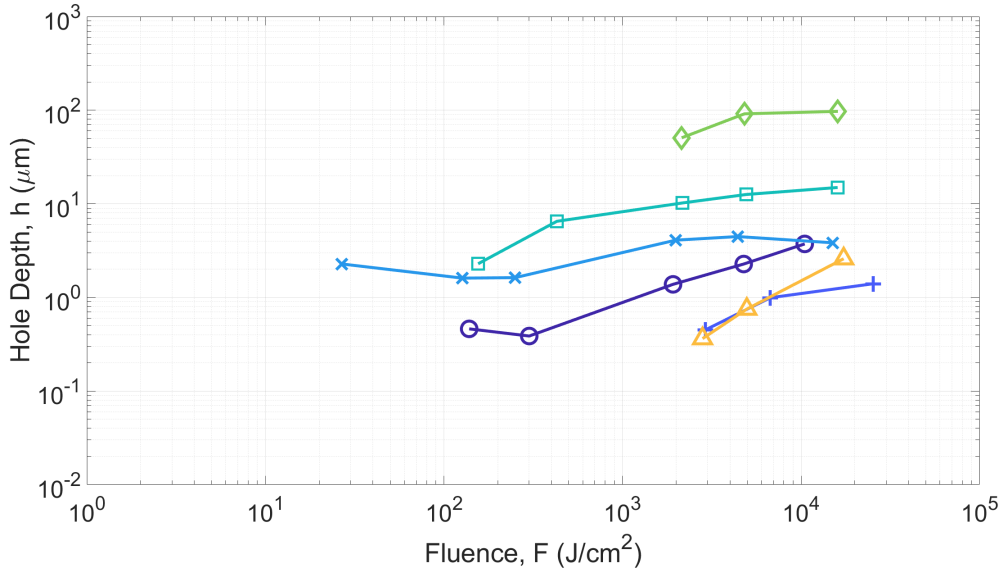

Figure 13. Hole depth from laser ablation with $\lambda = 1064$ nm, $\tau_p = 100$ ps (○), 1 ns (+), 10 ns (X), 100 ns (□), 1 μs (◊), 10 μs (△), $\omega_0 \approx 10$ μm, F : varied, Material: Si, $P = 1$ atm, $T = 300$ K.

For silicon, hole depths ranged from a minimum of 363 nm at a fluence of 2.8 kJ/cm^2 and a pulse duration of 9.2 μs to a maximum of 97.2 μm at a fluence of 16.1 kJ/cm^2

and a pulse duration of 1 μs. For the 100 ps and 1 ns configurations, the craters show very little melt displacement and surface deformations usually much larger than the beam's spatial extent. High-fluence shots between 10 ns and 1 μs show significant melt displacement and evidence of splatter is seen up to 150 μm from the crater center. The 1 μs 16.1 kJ/cm^2 case shows signs of multiple occurances of radial melt displacement, resulting in distinctly seperate melt re-solidification regimes. This is consistent with the "alternation of explosions" discussed by Martynyuk with regards to long pulse (i.e. not Q-switched) laser-induced phase explosion[45]. The ablation threshold at 1064 nm and a pulse duration of 20 ns is approximately 20 J/cm^2[42] and the threshold for explosive boiling at a 355 nm, 44 ns laser pulse is 440 J/cm^2[29], thus it is likely that explosive boiling is the primary mass removal mechanism for most of the experimental conditions in this study.

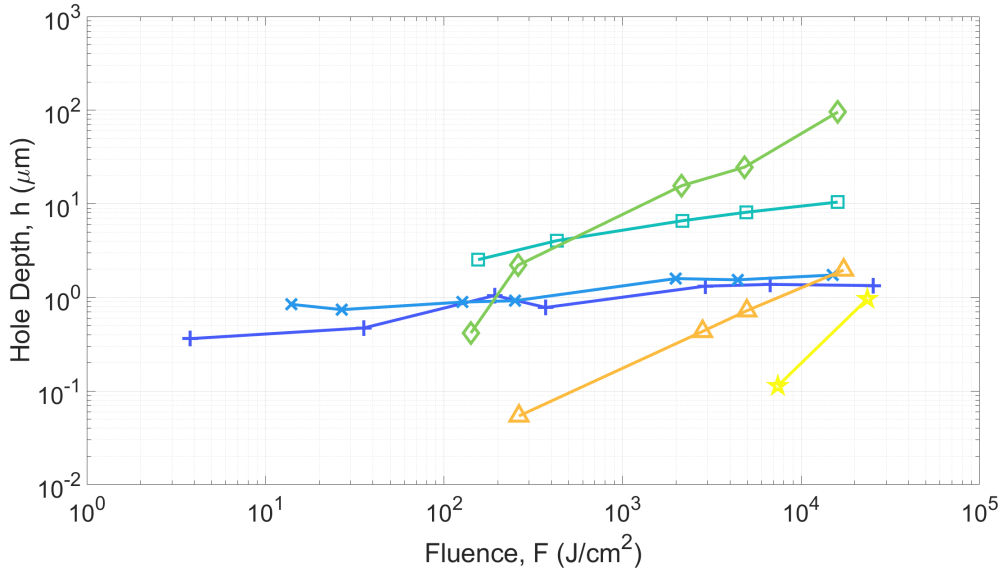

Figure 14. Hole depth from laser ablation with $\lambda = 1064$ nm, $\tau_p = 1$ ns (+), 10 ns (X), 100 ns (□), 1 μs (◇), 10 μs (△), 100 μs (★), $\omega_0 \approx 10$ μm, F : varied, Material: Ti, $P = 1$ atm, $T = 300$ K.

On titanium, the hole depths ranged from 85.4 nm at a fluence of 262.96 J/cm^2 and pusle duration of 9.19 μs to 95.75 μm at a fluence of 16.1 kJ/cm^2 and pulse duration of

1 μs. Like silicon, the shorter pulse durations resulted primarily in surface deformation, and no melt displacement. The 10 ns also resulted in only surface deformation, with the features seen nearly 300 μm from the center. The 100 ns and 1 μs configurations showed signficant melt displacement, up to 150 μm from crater center. These cases showed the same multiple melt displacement events that were seen on silicon, as well. Celen reported explosive boiling in titanium at 1064 nm and 200 ns at a fluence of 214 J/cm^2[37], so it is again expected that most of the data presented here corresponds to mass removal by explosive boiling.

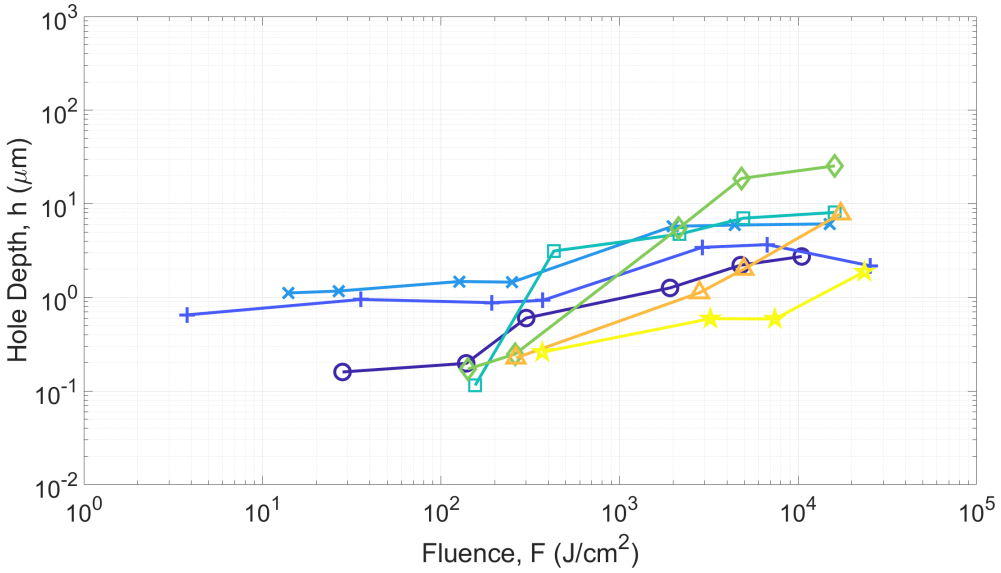

Figure 15. Hole depth from laser ablation with $\lambda = 1064$ nm, $\tau_p = 100$ ps (∘), 1 ns (+), 10 ns (X), 100 ns (□), 1 μs (◊), 10 μs (△), 100 μs (★), $\omega_0 \approx 10$ μm, F : varied, Material: Ge, $P = 1$ atm, $T = 300$ K.

For germanium, the hole depths ranged from a minimum of 135 nm at a fluence of 155.4 J/cm^2 and a pulse duration of 90.5 ns to a maximum of 25.46 μm at a fluence of 16.1 kJ/cm^2 and pulse duration of 1 μs. Again the 100 ps and 1 ns cases showed wide area surface deformation, rather than crater formation. The 10 ns through 1 μs cases showed significant melt displacement as well as repeated melt displacement events. Additionally, the 100 ns and 1 μs cases showed splatter deposited beyond the re-solidified melt.

There is apparently no published literature on explosive boiling in germanium, but assuming its threshold is on the order of 10-100 times the normal ablation threshold, it is likely that a significant number of experimental conditions produced explosive boiling.

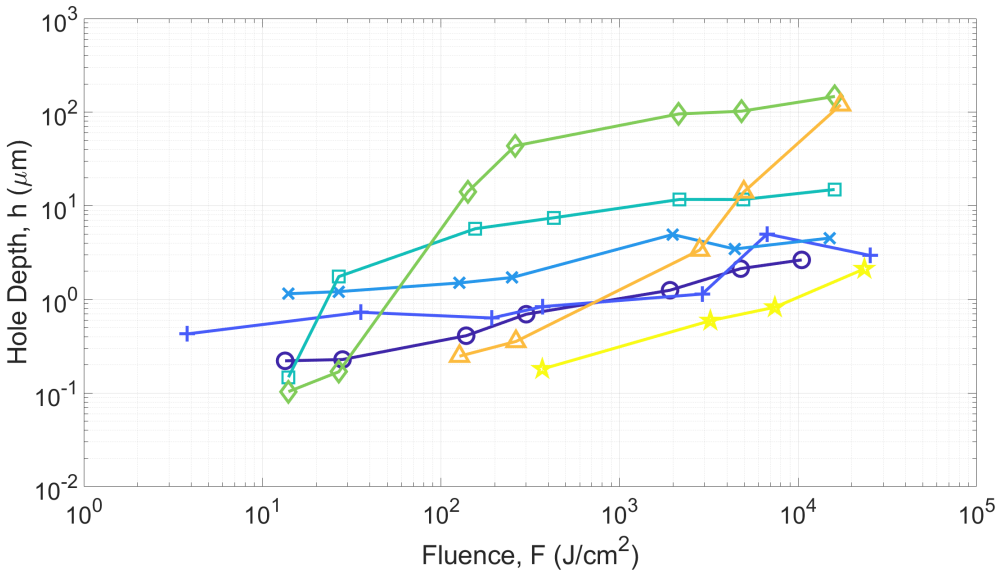

Figure 16. Hole depth from laser ablation with $\lambda = 1064$ nm, $\tau_p = 100$ ps (∘), 1 ns (+), 10 ns (X), 100 ns (□), 1 μs (◊), 10 μs (△), 100 μs (★), $\omega_0 \approx 10$ μm, F : varied, Material: InSb, $P = 1$ atm, $T = 300$ K.

Hole depths on InSb ranged from 197 nm at a fluence of 369.4 J/cm^2 and a pulse duration of 95.2 μs to 147.4 μm at a fluence of 16.1 kJ/cm^2 and pulse duration of 1 μs. The 100 ps and 10 ns cases showed shallow craters with surface deformation at distances up to 800 μm from center. The 1 ns case was particularly striking with surface deformation seen over 1 mm from crater center, much further than on any other material in the current study. The 100 ns and 1 μs cases produced a comparatively large area of re-solidified melt nearly 400 μm across, with additional droplets splattered even further.

Table 1 shows the highest fluence where no measurable damage occurred for each pulse duration on each material. In some instances, there was visual evidence of damage, but it was not measurable, i.e. the feature depth was comparable the surface roughness. In the table, a dash corresponds to a pulse duration where no measurable damage

occurred for any fluence, and an asterisk denotes cases where the lowest fluence tested produced measurable damage. Due to the coarseness of the steps in fluence, a more detailed analysis of the ablation threshold is prohibited. As mentioned above, an in-depth graphical analysis of crater morphology will occur in a separate publication.

Table 1. Highest tested fluence, F (J/cm^2), that caused no measurable damage.

τ_p	Al	Si	Ti	Ge	InSb
100 ps	-	28	-	13	*
1 ns	-	371	*	*	*
10 ns	27	14	*	*	*
100 ns	27	27	27	27	*
1 μs	260	260	27	27	*
10 μs	2806	263	127	127	27
100 μs	-	-	3227	127	127

3.3.2 Volume Removed and Ablation Efficiency

In addition to hole depth, the volume removed was measured with the laser confocal microscope. Figure 17 shows the crater volume for all experimental cases on Ge. As with hole depth, the largest volume removed occurs at the 1 μs pulse duration. Typical uncertainties in volume measurements were approximately 10%. Crater volume scaled with fluence similarly to depth, with both measurements strictly increasing within experimental uncertainty for almost all cases. Increasing crater volume also coincided with increased splatter size and distance from center of the crater. The volume removed discussed here only includes mass removed from below the surface of the material, and does not include melt displaced above the surface or redeposited matter.

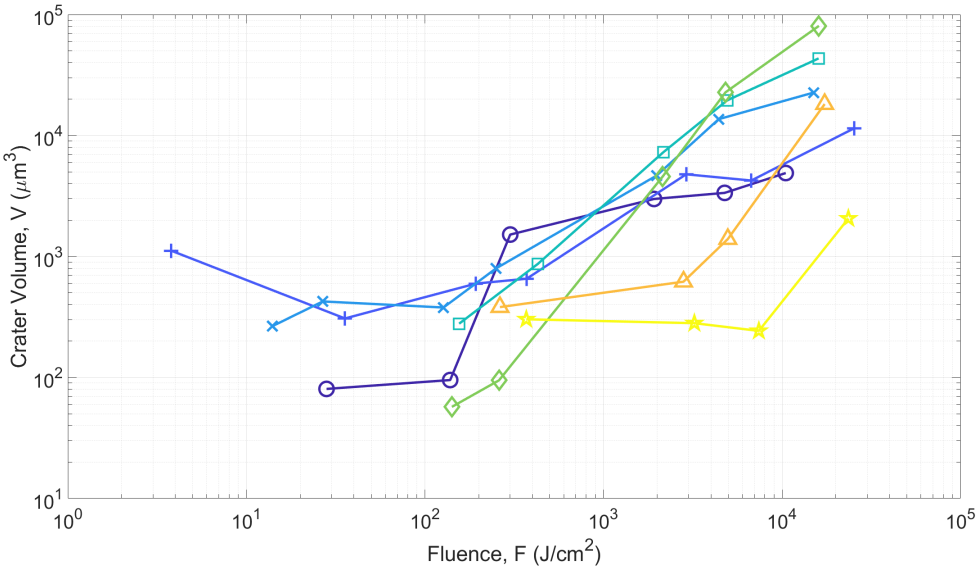

Figure 17. Hole volume from laser ablation with λ = 1064 nm, τ_p = 100 ps (○), 1 ns (+), 10 ns (X), 100 ns (□), 1 μs (◇), 10 μs (△), 100 μs (★), $\omega_0 \approx 10$ μm, F : varied, Material: Ge, $P = 1$ atm, $T = 300$ K.

From the volume, the ablation efficiency defined as atoms removed per incident photon was characterized. On germanium, for pulse durations less than 100 ns, the ablation efficiency decreased with increasing fluence, while for the 100 ns and 1 μs cases, ablation efficiency increased as fluence increased. For 10 μs and 100 μs, there are fewer data points and the trend is not as clear. The other materials followed similar trends where data was available. Figures 18 and 19 show the ablation efficiency and volume removed for the 10 ns and 1 μs pulse durations on germanium, respectively. Table 2 summarizes the minimum and maximum volume removed and ablation efficiency for each material. The maximum ablation efficiency corresponded to the maximum volume removed, which occurred at 1 μs for each material. The minimum ablation efficiency corresponded to the minimum volume removed for each material, occurring at 10 ns on Al, 10 μs for Si and Ti, 100 ns for Ge, and 100 μs on InSb.

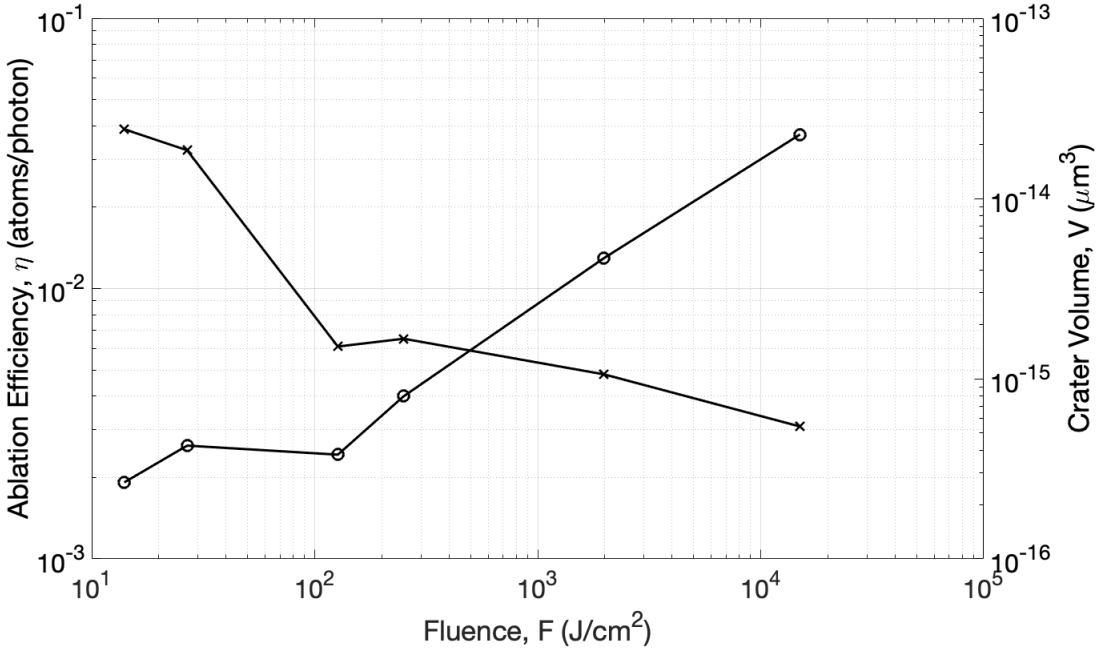

Figure 18. Ablation efficiency (×, left axis) and crater volume (∘, right axis). λ = 1064 nm, τ_p = 10 ns, $\omega_0 \approx 10$ μm, F : varied, Material: Ge, P = 1 atm, T = 300 K.

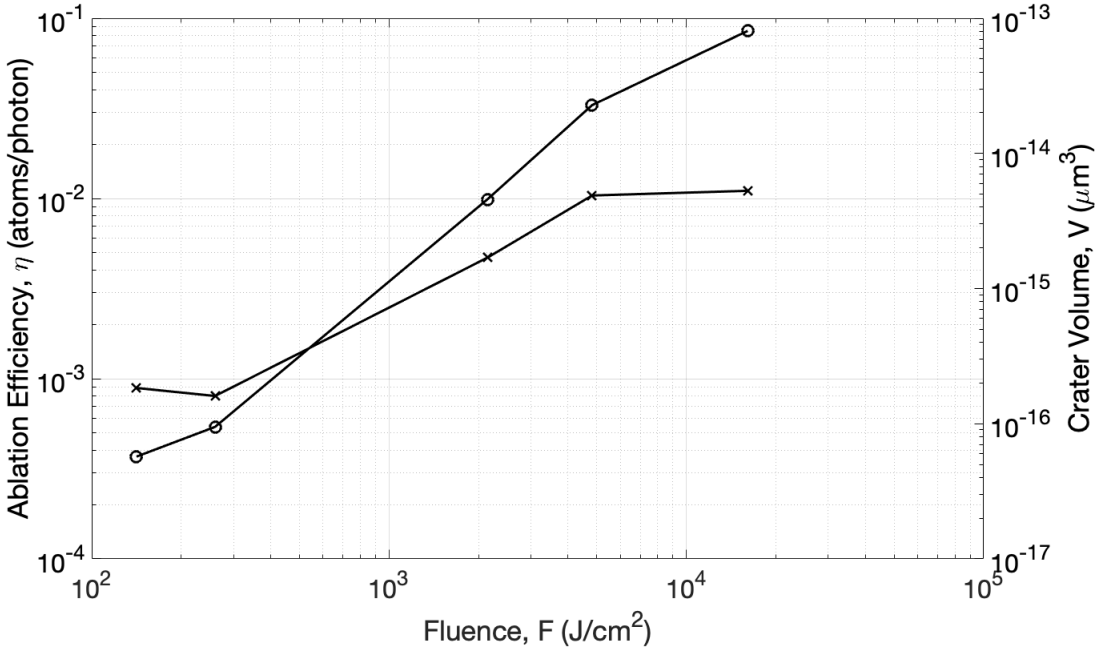

Figure 19. Ablation efficiency (×, left axis) and crater volume (∘, right axis). λ = 1064 nm, τ_p = 1 μs, $\omega_0 \approx 10$ μm, F : varied, Material: Ge, P = 1 atm, T = 300 K.

Table 2. Volume removed and ablation efficiency

Material	Min Vol (μm^3)	Max Vol (μm^3)	Min Eff	Max Eff
Al	347	96,000	1.3×10^{-2}	1.8×10^{-2}
Si	82	61,000	9.7×10^{-5}	9.6×10^{-3}
Ti	2	101,000	2.3×10^{-5}	1.9×10^{-2}
Ge	302	81,000	4.6×10^{-3}	1.0×10^{-2}
InSb	126	361,000	3.9×10^{-4}	1.7×10^{-2}

It is worth mentioning that there are alternative definitions of ablation efficiency that might be of use. For example, in describing the efficiency of a laser, the ratio of output energy to input energy is typically used. In the present case, the values in Table 2 for maximum efficiency can also be converted to output energy (i.e. the mass removed converted to energy via the heat of vaporization) relative to input energy (i.e. laser pulse energy) from atoms per photon. The resulting ablation efficiencies for Al, Si, Ti, Ge, and InSb are: 4.1%, 2.1%, 7.1%, 2.4%, and 6.5% assuming vaporization is the primary mass removal mechanism. The relatively low efficiency implies that well above the ablation threshold, most of the energy does not go into removing mass, but likely into plume kinetic energy as in Reference [14] for short pulse durations, or conducted away into the material for long pulse durations. Without plume imagery or time-dependent temperature measurements, it is beyond the scope of this dissertation to ascertain where specifically the rest of the laser energy went.

3.4 Discussion

The thermal response of a material to the absorbed laser energy is well-developed in References [20, 46]. Thermal response generally controls ablation for pulse durations exceeding the electronic relaxation time, which is typically on the order of 1 ps

for most materials[1], and should broadly apply to the current study. Given the high-dimensionality and relative sparseness of the collected data set, scaling factors were sought first to identify trends rather than attempt to accurately capture the many physical mechanisms involved. For a semi-infinite slab illuminated by a flat-top beam, including axial (z- direction) and radial (r-direction) thermal diffusion, the temperature rise at the center of the beam ($r = 0$) evolves as:

$$\Delta T(z,t) = \left(\frac{2I(1-R)}{K}\sqrt{\kappa t_p}\right)\left[\text{ierfc}\left(\frac{z}{\sqrt{4\kappa t_p}}\right) - \text{ierfc}\left(\frac{\sqrt{z^2+\omega_0^2}}{\sqrt{4\kappa t_p}}\right)\right] \tag{1}$$

where I being the incident irradiance in W/m^2 and R the reflectivity, K is the thermal conductivity in W/(m·K), κ is the thermal diffusivity equal to $K/\rho C$ with units m^2/s, ρ is the material density in kg/m^3, C is the specific heat capacity with units J/(kg·K), t_p is the pulse duration, z is depth into the material, and ω_0 is the beam extent in the radial direction[20, 46]. The function ierfc is the integral of the complementary error function. Radial (transverse) heat conduction is accounted for by the second term, whereas the first term alone is appropriate for a uniform illumination with no radial diffusion. Convection and radiative heat transfer contribute less than 0.3% and 1%, respectively for the current experimental conditions.

Note that Equation 1 does not include phase changes or temperature dependent properties and is intended to illustrate fundamental thermal scaling. Furthermore, it does not include liquid-phase material parameters, such as viscosity. Again, for the purposes of this chapter, first order scaling parameters are sought. Chapter 4 will discuss the liquid-phase effects in more detail. Since the material absorptivity is not included in Equation 1, it is assumed that the incident radiation is absorbed entirely at the surface.

The relative sizes of the thermal diffusion length, L (see definition below), the absorption depth, α^{-1}, and the spot size, ω_0, determine the dimensionality of the prob-

lem. For example, if $\omega_0 \gg L \gg \alpha^{-1}$, then the problem is primarily one-dimensional (i.e. $\omega_0 > \max(L, \alpha^{-1})$) and energy is absorbed at the surface and then conducted deeper into the material (i.e. $L > \alpha^{-1}$)[17]. If $\omega_0 \gg \alpha^{-1} \gg L$, then the problem is still one-dimensional, but the energy is deposited over a length larger than the thermal diffusion length, and the absorption depth becomes the primarily depth scale. Finally, if either $L > \omega_0$ or $\alpha^{-1} > \omega_0$, then the problem is not one-dimensional.

Figure 20 shows the relevant length scales, L and α^{-1}, for the materials and pulse durations in the current study with the absorption properties for 1064 nm wavelength and a spot size of $\omega_0 \approx 10$ μm. For all materials, $\omega_0 > L$ up to approximately 1 μs, and for all materials except Si, $\omega_0 > \alpha^{-1}$ (for all pulse durations, since the absorption coefficient is not a function of time). For Si, however, the nominal absorption depth at 1064 nm wavelength is orders of magnitude larger than both the thermal diffusion depth and the spot size.

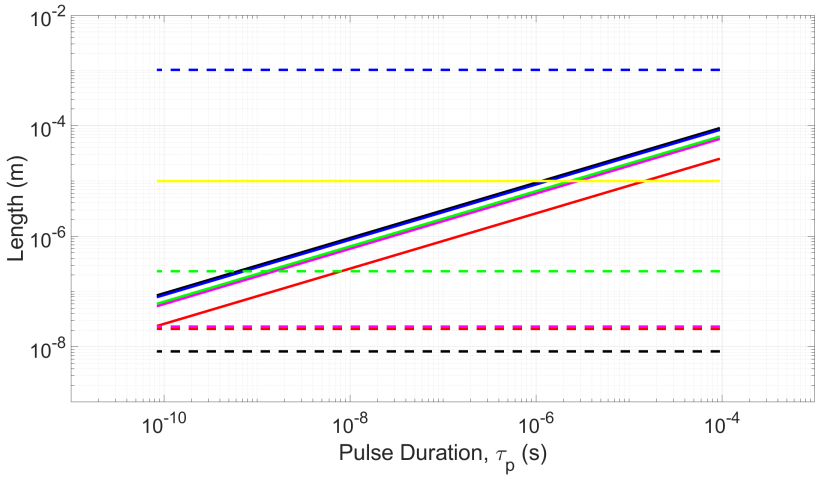

Figure 20. Relevant length scales, L (solid lines) and α (dashed lines), for Al (-), Si (-), Ti (-), Ge (-), and InSb (-) at $\lambda = 1064$ nm. Spot size is $\omega_0 \approx 10$ μm (-)

The absorption coefficient of Si increases dramatically with rising temperature[47]. For the highly energetic pulses used in this study, temperature increases induced on the leading edge of the pulse will lead to the rest of the pulse being absorbed much closer to

the surface, and the quasi-one dimensional approximation becomes more reasonable. Thus, for the purposes of this experiment, it is assumed that $\omega_0 > \alpha^{-1}$ and the energy is effectively absorbed at the surface for all conditions on all materials.

As for the thermal diffusion length during longer pulse durations (e.g. $\tau_p > 1$ μs), even though the thermal diffusivity of most materials tends to decrease with temperature (leading to a decrease in thermal diffusion length), the application of a quasi-one dimensional model is no longer rigorously correct. However, the purpose of this approach is not to formulate a rigorous, predictive model of laser ablation, rather, the goal is to provide the simplest data transformation in order to discern common features and trends in the measured data. To that end, the quasi-one dimensional approach will be used for the remainder of this dissertation.

Table 3. Material parameters and relevant physical scales

	Al	Si	Ti	Ge	InSb
m (AMU)	27	28	48	73	237
ρ (kg/m^3)	2700	2329	4500	5323	5775
L_v (J/kg)	10.5×10^6	1.28×10^7	8.85×10^6	4.58×10^6	1.8×10^6
L_m (J/kg)	3.87×10^5	1.8×10^6	4.55×10^5	4.78×10^5	8.03×10^4
K (W/m/K)	210	124	17	60.2	18
C (J/kg/K)	900	740	528	322	144
κ (m^2/s)	8.64×10^{-5}	7.19×10^{-5}	7.15×10^{-6}	3.51×10^{-5}	2.16×10^{-5}
ν (mPa·s)	1.3	0.57	3.0	0.74	1.16
T_m (K)	933	1687	1941	1211	800
T_v (K)	2743	3538	3560	3106	2127
T_c (K)	6700	5160	5850	8900	5925
F_{th} (J/cm^2), $t_p = 100$ns	7.14	6.42	3.31	3.18	1.45
L (μm), $t_p = 100$ns	2.94	2.73	0.82	1.87	2.07
t_ω (μs), $\omega_0 = 10\mu$m	1.15	1.34	14.83	2.85	2.34

The material parameters and physical scales relevant to the current study are given

in Table 3. Here, m is the atomic mass, ρ is the density, L_v is the latent heat of vaporization, L_m is the latent heat of fusion (melting), K is the thermal conductivity, C is the specific heat capacity, $\kappa = K/\rho C$ is the thermal diffusivity, ν is the viscosity, T_m is the melt temperature, T_v is the vaporization temperature, and T_c is the critical temperature. For the current study, several physical scales are presented as well: F_{th} is the fluence threshold for vaporization for a 100 ns pulse duration, $L = \sqrt{\kappa t}$ is the thermal diffusion length, and $t_\omega = \omega_0^2/\kappa$ is the thermal diffusion time relative to the incident spot size. The latent heat of vaporization and vaporization temperature for InSb are estimated by averaging the respective parameters for indium and antimony.

The transverse heat conduction is insignificant for shallow depths $z \ll \omega_0$ such that in Equation 1, $\sqrt{z^2+\omega_0^2} \approx \omega_0$ and

$$\text{ierfc}\left(\frac{\omega_0}{\sqrt{4\kappa t_p}}\right) \ll 1 \tag{2}$$

or

$$t_p \ll \frac{\omega_0^2}{\kappa} \equiv t_w. \tag{3}$$

For a nominal spot size of 10 μm on germanium, $t_w = 2.85$ μs. Thus for pulse durations less than t_w, radial diffusion is expected to be negligible during the pulse, but for pulse durations greater than this value, conduction losses in the material are expected to reduce mass removed. Radial diffusion is fastest for Al, but slow for Ti.

The energy required to vaporize a volume, V, of material assuming that all energy goes into raising the temperature of the volume and causing phase changes is

$$E = \rho\left[C\left(T_m - T\right) + L_m + C\left(T_v - T_m\right) + L_v\right]V. \tag{4}$$

The temperature near the surface and within the laser spot (i.e. for some $\delta z \ll \omega_0$) after

the pulse duration, t_p, is derived from Equation 1:

$$\Delta T(\delta z, t_p) = \left(\frac{2I(1-R)}{\sqrt{\pi}K} \sqrt{\kappa t_p} \right). \tag{5}$$

where the transverse heat conduction term in Equation 1 has been dropped because only shallow depths into the material are of concern for this threshold calculation (i.e. $z \ll \omega_0$). Equation 5 assumes nominal solid-phase material parameters, but for a first-order threshold calculation, this is sufficient. Zero reflection at the surface (the reflectivity of almost all materials decreases with increasing temperature) and no shielding of the surface by the ionized plume (i.e. the shielding would not occur until the fluence is above threshold anyway) are assumed. Multiplying the right hand side of Equation 5 by the density and specific heat results in the energy density required to vaporize a unit volume of material:

$$\frac{2\rho C I}{\sqrt{\pi}K} \sqrt{\kappa t_p} = \rho \left[C \left(T_v - T_0 \right) + L_m + L_v \right] \tag{6}$$

which can be solved for I to find the vaporization threshold irradiance

$$I_{\text{th}} = \frac{\sqrt{\pi}}{2} \rho L_v \sqrt{\frac{\kappa}{t_p}} \left[C\Delta T + L_m + L_v \right]. \tag{7}$$

According to Table 3, the heat of fusion, L_m, is typically an order of magnitude less than L_v for the materials of interest, so for an approximate threshold, it can be ignored. The energy required to raise the temperature, $\rho C \Delta T$, can also be left out because it is typically much less than the heat of vaporization. For example, for silicon at an initial temperature of 300 K, the energy required to raise the temperature to the vaporization point is $\rho C \Delta T = 5.4 \times 10^9$ J/m^3, or 22% of ρL_v, which can be ignored for a first-order threshold calculation. With these assumptions, the irradiance and fluence thresholds simplify to:

$$I_{\text{th}} = \rho L_v \sqrt{\frac{\kappa}{t_p}} \tag{8}$$

$$F_{\text{th}} = I_{\text{th}} t_p = \rho L_v \sqrt{\kappa t_p}. \tag{9}$$

The fluence thresholds for a 100 ns pulse shown in Table 3 were calculated using Equation 9. In order to interpret effects across different materials, fluences, and pulse durations shown in Figures 13-12, non-dimensional scaling factors were developed. The non-dimensional hole depth is

$$h^* = \frac{h}{L} = \frac{h}{\sqrt{\kappa t_p}} \tag{10}$$

where h is the measured hole depth, and L is the thermal diffusion length during the pulse duration, t_p. This allows comparison of hole depth relative to both different materials (e.g. different κ) and different pulse durations. Hole depth was chosen as the primary response variable because the thermal model is quasi-one dimensional. The non-dimensional pulse duration is

$$t^* = \frac{t_p}{t_\omega} = \frac{\kappa t_p}{\omega_0^2} \tag{11}$$

where t_p is again the pulse duration, and t_ω is the time it takes for heat to diffuse a length equal to the spot radius, ω_0. Values for t_ω assuming a 100 ns pulse duration an a spot radius (1/e) of 10 μm are shown in Table 3. And finally, the non-dimensional fluence is

$$f^* = \frac{F}{F_{\text{th}}} = \frac{F}{\rho L_v \sqrt{\kappa t_p}}. \tag{12}$$

where F is the incident fluence and F_{th} is the fluence threshold of the material at a particular pulse duration, ρ is the density, and L_v is the latent heat of vaporization. Example

values of F_{th} assuming a 100 ns pulse duration are shown in Table 3. Intuitively, f^* is a measure of the excess fluence. Note that $f^* = 1$ is the threshold for evaporation, and the threshold for explosive boiling, or any other mass removal mechanisms, will likely occur at higher values of f^*.

The hole depth relative to the thermal diffusion length, h^*, increase with fluence above threshold, f^*, for all materials as shown in Figure 21. The thermal analysis significantly improves the correlation of the data and simplifies the material dependence. The current study emphasizes fluences of $10 - 10^5$ times the normal ablation threshold, and approximately $0.5 - 10^4$ times the threshold for phase explosion. Significant mass is removed, with hole depths approaching 100 times the thermal diffusion length.

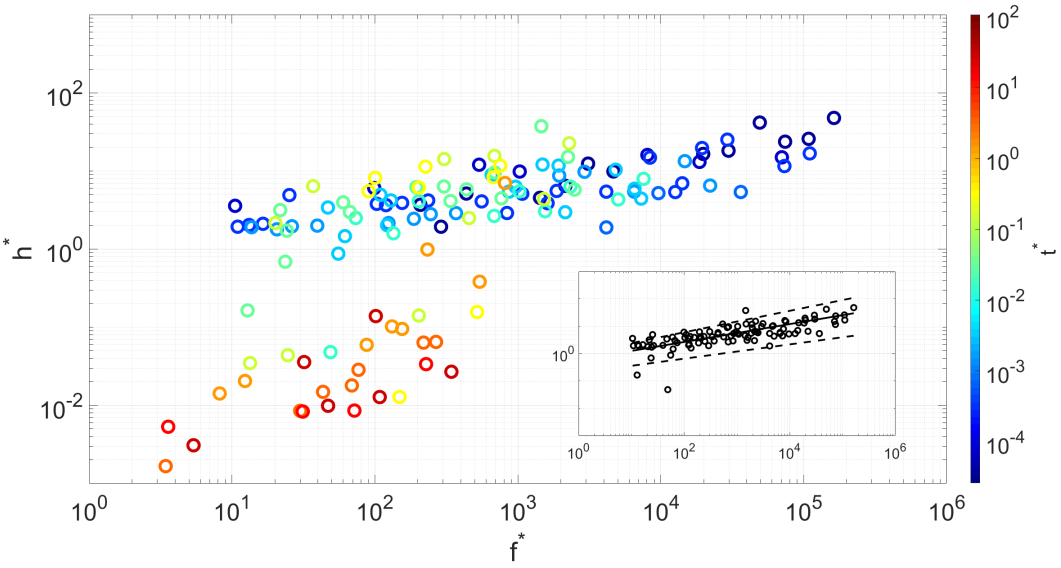

Figure 21. Non-dimensional hole depth as a function of non-dimensional fluence. $\lambda = 1064$ nm, τ_p : varied, $\omega_0 \approx 10$ μm, F : varied, $P = 1$ atm, $T = 300$ K. Inset: power-law fit of $f^* > 10$ and $t^* < 0.1$ data.

There are two prominent clusters of data in Figure 21. First, for $t^* \gg 1$, almost all of the data points have $h^* \ll 1$, the scatter is significant, and there is no clear trend with increasing f^*. Second, for $t^* \ll 1$, the hole depths are much greater than the thermal diffusion length, the scatter in the data is reduced, and the scaling with fluence appears

to follow a power law form. This implies that somewhere in $0.1 < t^* < 10$ is a temporal transition point between two distinct physical regimes.

Considering only data with $t^* < 0.1$ and $f^* > 10$, corresponding roughly to the onset of explosive boiling, it is found that h^* does indeed follow a power law of the form $h^* = af^{*b}$ with $a = 0.18 \pm 0.08$ and $b = 0.47 \pm 0.06$. The uncertainty in the fit parameters correspond to the 95% confidence intervals. Lutey found a similar power law depending on the value of the shielding coefficient used in the model when fitting to experimental data at 5 ns on Al from [31], with the power found to be between approximately 0.5 and 0.8[32].

Figure 22 shows h^* versus t^* for all materials and pulse energies. The distinct regimes based on the pulse duration relative to the radial diffusion time of $t^* \ll 1$ and $t^* \gg 1$ are again clearly visible. A vast majority (more than 90%) of the data resides in two quadrants of the graph. First, for $t^* \ll 1$, most holes have $h^* > 1$, physically corresponding to the situation where heat being deposited by the laser faster than it can be conducted away from the laser spot. In this regime, for sufficiently high f^*, explosive boiling is the dominant mass removal mechanism, which requires that a volume be heated to near the critical temperature for long enough to allow homogenous nucleation to facilitate ejection of the super-heated layer. Thus, the faster the heat is deposited and the slower the heat is conducted away, the larger the h^* is expected to be. Second, for $t^* \gg 1$, almost all of the data has $h^* < 1$. Heat is conducted away from the laser spot area before temperature rises sufficiently to cause mass removal. Thus, for shorter pulse durations (relative to the time it takes heat to conduct a length comparable to the spot size), the heat transfer is more more one-dimensional, whereas for longer pulse durations, transverse heat transfer becomes important.

It is interesting to note that for all materials, the largest absolute hole depth (e.g. not necessarily the largest h^*) occurred near $t^* \approx 1$. For Al, Si, Ti, Ge, and InSb this occurred

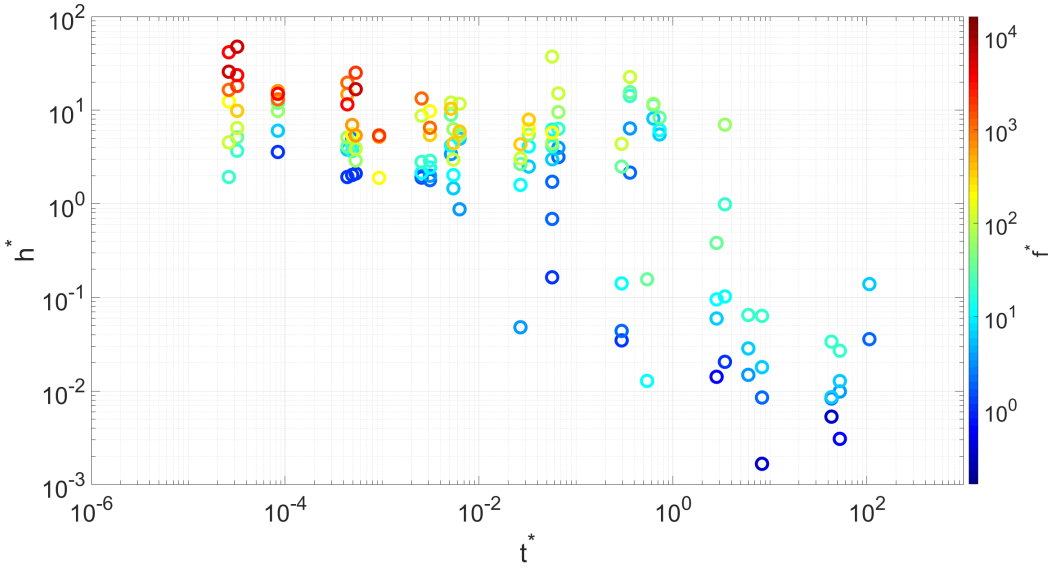

Figure 22. Non-dimensional hole depth as a function of non-dimensional pulse duration. $\lambda = 1064$ nm, τ_p: varied, $\omega_0 \approx 10$ μm, F : varied, $P = 1$ atm, $T = 300$ K.

at a t^* value of 0.73, 0.63, 0.11, 0.3, and 0.36, respectively. As mentioned above, the decrease in hole depth for $t^* \gg 1$ is due to heat conduction away from the laser spot. However, the decrease in hole depth (as opposed to the increase in h^*) with $t^* \ll 1$ requires explanation. Martynyuk found that the time to heat the surface to near the critical temperature needed to be less than 10^{-5} s in order to induce transparency in the surface liquid layer and superheat the material beneath[45]. Due to induced transparency, the heated depth can be many times the thermal diffusion length (in terms of the incident pulse duration), and $t^* \approx 1$ corresponds (in this quasi-one dimensional model) to the maximum thermal diffusion length before heat conduction losses become dominant. Thus, maximum hole depth is expected in the broad neighborhood of $t^* \approx 1$.

Figure 23 shows the shielding parameter as a function of t^* for each material. As t^* becomes much less than 1, the shielding of the material by ejected material increases. By using the power-law fit described above on each material, and identifying the b in $h^* = af^{*b}$ as being inversely proportional to the shielding coefficient from Reference [32], then b^{-1} can be interpreted as a measure of shielding. It can be seen that the

shielding peaks at a value of $t^* < 1$ and decreases as $t^* \to 1$ and reaches a minimum in the neighborhood of $t^* \approx 1$. The shielding also begins to decrease as t^* decreases from the peak (e.g. for $t^* < 0.066$ for InSb). Since shielding effects are still expected to be significant into the low 10's of picoseconds pulse durations[36], this is likely due to less mass being removed at a constant fluence as pulse duration decreases. It is possible that less mass is removed for a given fluence as pulse duration decreases due to the spoiling of the homogeneous nucleation process in explosive boiling[45]. For very short pulses (e.g. 1 ns or less), the surface liquid layer is not completely transparent before the pulse ends, and the heating of the sub-surface layer does not occur. The material removed in that case mostly consists of the unstable liquid layer being directly dissociated from the surface[45]. Thus, less mass is removed at shorter pulse durations, which produces less shielding as evidenced by the decrease in the shielding parameter, b^{-1}.

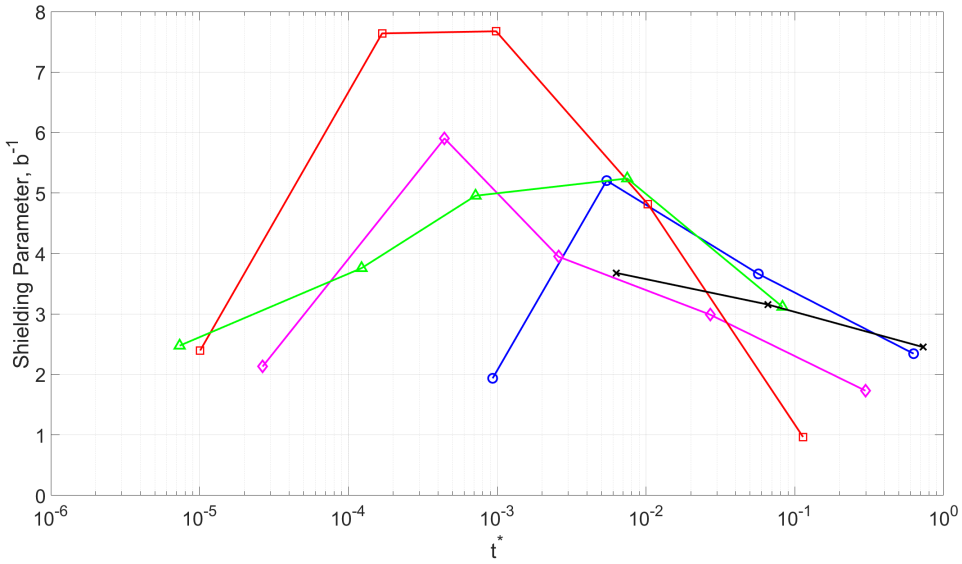

Figure 23. Shielding coefficient for $\lambda = 1064$ nm, τ_p : varied, $\omega_0 \approx 10$ μm, F : varied, Material: Al (×), Si (○), Ti (□), Ge (♢), and InSb (△), $P = 1$ atm, $T = 300$ K.

3.5 Conclusion

Five materials (two metals, two indirect semiconductors, and one compound semiconductor) were ablated across seven decades in pulse duration (84 ps to 100 μs) and fluence (0.004-25 kJ/cm^2), and craters were measured using a laser confocal microscope. Crater depths ranged from a minimum of 85.4 nm on Ti with a fluence of 263 J/cm^2 at a pulse duration of 9.19 μs to a maximum of 147.4 μm on InSb at 16.1 kJ/cm^2 at 1 μs. Crater volume was found to increase with increasing fluence, but the ablation efficiency, defined as atoms removed per incident photon, actually decreased with increasing fluence for pulse durations less than 100 ns. Overall, ablation efficiency was between 10^{-5} and 10^{-2} for all materials. Thermal scaling of the data using a simple quasi-one dimensional heat transfer approach were introduced to analyze the data. A clear trend with respect to t^* was seen in that for $t^* \ll 1$, holes were made that were deeper than the thermal diffusion depth at that pulse duration. For $t^* \gg 1$, it appears that transverse heat conduction dominates, and holes much shallower than the thermal diffusion depth are made. Moreover, for $t^* < 0.1$ and $f^* > 10$, explosive boiling appears to be the dominant mass removal mechanism for all materials. The non-dimensional hole depth scales as fluence to approximately the 0.4-0.5 power, consistent with other experimental and numerical investigations. Further, the power-law exponent is related to the shielding of the laser pulse by ejected material, and this shielding reaches a maximum at some $t^* < 1$ for each material. The shielding is found to be at a minimum near $t^* \approx 1$, and decreases again at the shortest pulse durations due to less mass being removed. The craters made by explosive boiling are strikingly similar once transformed by the scaling variables, indicating a more universal behavior that is less dependent on specific material properties, e.g. semiconductor versus metal. Additional crater morphology analysis is needed to possibly identify changes in mass removal mechanism, specifically to investigate the spoiling of the homogeneous nucleation process in explosive boiling as pulse duration

decreases. This formalism allows the comparison of laser ablation data across different materials at the same wavelength and background pressure. More data needs to be collected in order to extrapolate damage data across various wavelengths and background pressures, and specifically, more data at lower fluence levels are needed to connect this study to typical ablation investigations.

4. Picosecond Laser Ablation of Metals and Semiconductors with Low Transverse Order Gaussian Beams

In order to expand the non-dimensional scaling variables derived in the previous chapter (e.g. to lower values of t^*), a separate experiment was performed in which low transverse order Gaussian beams at 1064 nm wavelength and 28 ps pulse duration were used to ablate Al, Si, Ti, Ge, and InSb in air, and Ge in vacuum. Crater depths and volumes, as well as volume of material above the surface were measured using a laser confocal microscope. Crater depths were found to plateau with increasing fluence on each material, and crater depths on Ge in vacuum were slightly higher than in air. Crater volume above and below the surface was found to increase linearly with fluence for all materials in air. In vacuum, the volume of material above the surface was less than in air, and increased at a lower rate with increasing fluence. The ratio of volume above the surface to volume below the surface was found to plateau for all materials to approximately 0.7 in air, and 0.4 for Ge in vacuum. The ablation efficiency, defined as atoms removed per incident photon was higher at low fluences, and decreased to approximately 0.004 for all materials at higher fluences. Simulations using the Directed Energy Illumination Visualization tool showed that bulk melt flow out of the crater caused by the evaporation recoil pressure dominated at higher fluences. Plateauing of crater depth with fluence was caused by melt re-flow into the crater, which effects smaller crater widths more than larger ones, as evidenced by comparing multi-mode results to TEM_{00} simulations. Recondensation of evaporated material was identified as the main difference between craters formed in air versus vacuum, and the Knudsen layer jump conditions in DEIVI were modified to account for an estimated $\approx 20\%$ recondensation rate. The simulations showed a resulting reduction in evaporation, which created less recoil pressure, driving less melt out of the crater. Higher resolution simulations and additional experimental data comparing different order modes are needed to further explore the effects of di-

verse spatial fluence distributions.

4.1 Introduction

Laser ablation encompasses a wide variety of phenomena that depend on material parameters as well as laser wavelength, pulse duration, and fluence. Mass removal at short wavelengths (e.g. ultraviolet) and short pulse durations (< nanoseconds) occurs primarily by electronic means, and thermal effects are minimal[28]. Longer wavelengths (compared to the work function of the material) remove mass by raising the temperature of the material to the vaporization point, resulting in potentially significant melt flow effects and resolidification[48]. As pulse duration decreases, the material is heated faster, and phase explosion or explosive boiling, can occur resulting in significantly more mass removed than simple evaporation[45].

Numerous studies have investigated how mass removal changes as pulse duration decreases[48, 36, 49]. Yoo et al studied explosive boiling in silicon with 3 ns pulses at 266 nm wavelength, and found a steep increase in crater depth and volume at an irradiance of 2.2×10^{10} W/cm^2[30]. The homogeneous nucleation time was estimated to be 300-400 ns, matching laser shadowgraph images of droplet ejection[30]. Leitz et al studied laser ablation of steel in air from femto- to microseconds pulse durations, finding that explosive boiling was the primary mass removal mechanism for femto- and picosecond pulses, and craters were marked by jagged features and re-solidified droplets[44].

As the laser pulse duration becomes comparable to or shorter than the electron-phonon relaxation time, modeling approaches have been developed to describe non-thermal effects. In the hundreds of femtoseconds regime, a two-temperature model can be used to describe the ablation process, where photons are absorbed by electrons in the material, leading to high electron temperatures that couple to the bulk material on timescales longer than the pulse duration[48]. Some molecular dynamics simulations of

ps laser ablation show that phase explosion is the dominant mass removal mechanism, and for pulse durations shorter than the mechanical equilibrium time of the material, mass removal is enhanced by stress confinement[50, 51]. Lorazo et al performed molecular dynamics simulations of fs and ps ablation of Si, and showed that although homogeneous nucleation occurred in the super-heated volume, the vapor and liquid phases equilibrated on a timescale of 1-10 ps[52]. In that study, it was found that mass was removed not by phase explosion, but by bulk fragmentation of the near-critical material into liquid droplets[52]. Although these different microscopic mass removal processes involve very different physical phenomena, the macroscopic effect is bulk mass removal in liquid phase. Evidence of liquid-phase material will present as droplets, splatter, and re-solidified melt displacement in optical and laser confocal microscopy.

When vaporization is the primary mass removal mechanism and occurs when the laser pulse is still on, plasma shielding can occur in which laser photons are absorbed by free electrons in the ionized plume of ejected material. It was found in Chapter 3 that at a constant fluence, shielding was maximal with pulse durations between 1 and 100 ns. With a pulse duration of 100 ps, Lorazo et al found that only approximately 3% of the incident laser energy was shielded. In the shielding regime, however, as discussed in Chapter 1, additional photon energy is converted preferentially to plume expansion velocity rather than more mass removal[14, 5]. Thus, the ablation efficiency will decrease after a certain fluence as more energy goes into the plume. In contrast, the liquid phase mass removal processes discussed above typically occur after the laser pulse is over. Thus, the ablation efficiency can decrease after a certain fluence, but it is not due to additional energy going into the plume. Instead, the additional photon energy is converted to some secondary effect in the material.

Laser ablation using non-TEM_{00} spatial energy distributions is of interest to numerous fields including material processing, microfabrication, laser-induced breakdown

spectroscopy, and laser dentistry[53, 54, 22, 19]. Lednev et al studied crater differences between single mode and multi-mode Gaussian beams, including the effect on Beam profile impact on crater[22]. That study found that for equal pulse energies, the multi-mode crater was approximately 10 times wider but nearly 5 times shallower than the single mode crater, and marked by ripples associated with the spatial distribution of energy[22]. After 100 shots, crater volume for the multi-mode case was found to be approximately 3 times larger than the single-mode case, and the volume in the rim above the surface was 1-3 times smaller[22]. Vadillo et al found that craters with almost completely flat bottoms could be formed using a flat-top irradiance profile[55], and Cabalin and Laserna showed that annular-shaped beams lead to ringed craters were very little splatter or melt displacement[56].

Multi-mode illumination will induce complex temperature gradients in the material, causing non-uniform evaporation. Furthermore, multi-mode beams are typically difficult to quantify unless only a small number of modes are present. Thus, low-order Gaussian modes, of the form TEM_{lm}, provide a non-uniform fluence distribution that is also exactly quantifiable. Additionally, for single-mode irradiation, the recoil pressure from evaporation drives the melt flow radially out from the crater center where the evaporation rate and recoil pressure are the largest. It is expected that melt flow effects from the TEM_{lm} modes will be significantly more complex.

This paper investigates the crater morphology from 28 ps laser ablation of Al, Si, Ti, Ge, and InSb in air, and Ge in vacuum, using low-order Gaussian mode beams. Shielding is negligible for the 28 ps pulse duration in this study, and mass removal is expected to be largely dependent on liquid phase material properties. As such, this set of materials provides a wide variety of thermo-chemical properties to investigate liquid-phase mass removal with complex fluence distributions. In order to study the complex interplay between fluence distribution, melt flow effects, and ambient background pressure,

the Directed Energy Illumination Visualization (DEIVI) tool created by the Air Force Research Laboratory will be used. DEIVI is a two-dimensional finite element model that couples condensed phase phenomena with plume gas dynamics[38].

4.2 Apparatus and Methodology

An Ekspla PL2251A-10 modelocked Nd:YAG laser with a diode-pumped solid state master oscillator and flashlamp-pumped regenerative amplifier operating at 1064 nm produced 28 ps full-width $1/e$-max Gaussian pulses at 10 Hz. Typical shot-to-shot variation in pulse duration was less than 1%, and the pulse energy from the laser was constant at approximately 30 mJ split equally between TEM_{40} and TEM_{02} modes. Fluence on the sample was controlled by three half waveplates on rotation stages and polarizing beam-splitting cubes, providing a dynamic range of over 10^4, although ultimately the damage threshold of the cryostat window limited the maximum fluence. The measured pulse energy at the sample was varied from 37 μJ to 1.833 mJ and averaged over many pulses to get the pulse energy as a function of angle of the half waveplates. The beam was focused onto the sample with a 50.8 mm diameter, 100 mm focal length aspheric lens. The location of the focus along the direction of propagation, z, was found by performing a 3-dimensional beam scan using a 25 μm pinhole and detector mounted on a 3-axis MTN stage system from Newport using 1 μm steps in x and y and 100 μm steps in z. An MTI Instruments Protrak-G laser with 9.4 μm axial resolution was used to measure the offset between the beam profiling setup and the wafer surface in the cryostat. With a Rayleigh range of just over 10 mm, the uncertainty in spot size was due to the uncertainty in stage position during the measurement of the beam's lateral extent, resulting in a total fluence uncertainty of approximately 7% or less. The spatial shot-to-shot jitter, both radially and axially, was negligible.

The samples where held in an ARS LN-400 cryostat. The wafer temperature was

measured and controlled using a Lakeshore 336 temperature controller. All tests were performed at ambient room temperature, but data was also collected on Ge with wafer temperature ranging from 77 to 700 K. The background pressure was controlled using a Pfeiffer Hi-Cube Eco 2 turbo pump with a thermocouple vacuum gauge and manual bellows valve. The ultimate vacuum of the system was approximately 1.2×10^{-4} Pa, and the uncertainty on the pressure measurement was approximately 20%. The pressure in the cryostat was ambient air for each material, but data was also collected on Ge with pressures ranging from 2.2×10^{-3} to 6.4 Pa.

The silicon, titanium, and germanium wafers were 25.4 mm diameter and 0.5 mm thick, with single-side polished from MTI Corp. The aluminum and indium antimonide wafers were the same dimensions, but purchased from University Wafer. Each sample was ablated with one shot per test site. The samples were stored in a desiccator prior to use. No thermal cycling was performed in the cryostat, and an oxidation layer is assumed to be present. Over 700 laser shots were performed, and a row of 13 shots for each test case (i.e. pulse energy and pressure) was used to provide statistical significance to the crater measurements. The post-ablation samples were analyzed with a Zeiss laser confocal microscope, with better than 10 nm accuracy in the axial direction and sub-micron accuracy in the radial direction. Uncertainty in crater depth and volume is reported as the standard deviation of measurements made on multiple craters formed under the same conditions.

4.3 Results

4.3.1 Laser Spatial Energy Distribution

At the lowest pulse energy, each material showed surface features matching the spatial energy distribution of the incident beam. The spatial extent of the laser spot was characterized by examining the damaged area on Si wafers. Figure 24 shows craters

formed on Si that match the TEM_{40} and TEM_{02} Gaussian modes.

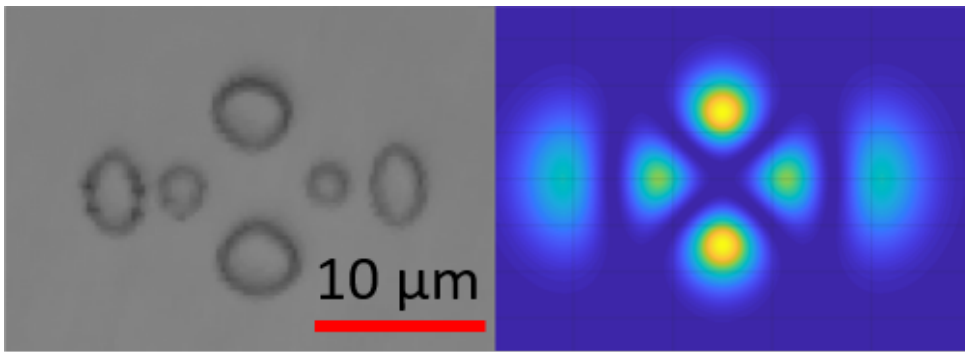

Figure 24. Measured crater (left) and simulated Gaussian TEM_{40} and TEM_{02} transverse spatial modes (right). $\lambda = 1064$ nm, $\tau_p = 28$ μs, $\omega_0 \approx 6.7$ μm, $F \approx 3.1$ J/cm^2, Material: Si, $P = 1$ atm, $T = 300$ K.

The spatial extent is approximately 21 μm in x and 10.5 μm in y measured center-to-center of the craters. The corresponding TEM_{00} beam waist in x and y, ω_0, was found to be 6.7 μm by matching the calculated fluence distribution to the measured crater pattern. The central peak of both modes is not visible because of the Gouy phase difference $\Delta\phi = (l+1) - (m+1) = 2$ causes destructive interference. For higher mode spots, ω_0 can still be interpreted as the standard deviation of the spatial energy distribution, but it is no longer useful as a measure of overall extent. A rectangle with sides $2\omega_l = 40.2$ μm and $2\omega_m = 30$ μm captures all of the peaks for the TEM_{40} and TEM_{02} modes, and is a more useful measure of beam extent[21]. Using this approach, the fluence in this study ranges from 3.1 J/cm^2 to 152.2 J/cm^2.

4.3.2 Ablation in Air

Optical and laser confocal microscopy were used to measure the craters. Measurement uncertainty was negligible compared to the statistical uncertainty across shots under same conditions, which was typically around 10%. Optical images were taken at each of the 13 ablation sites per condition, while laser confocal images were taken at every other site. Figure 25 shows optical images chosen to best represent the observed

features of each material and test case. Each image has a field of view of 232 × 232 μm, except for all of Ti and InSb at the two highest fluences (images 5e and 5f), which have increased field of view of 456 × 456 μm to account for larger area of effect.

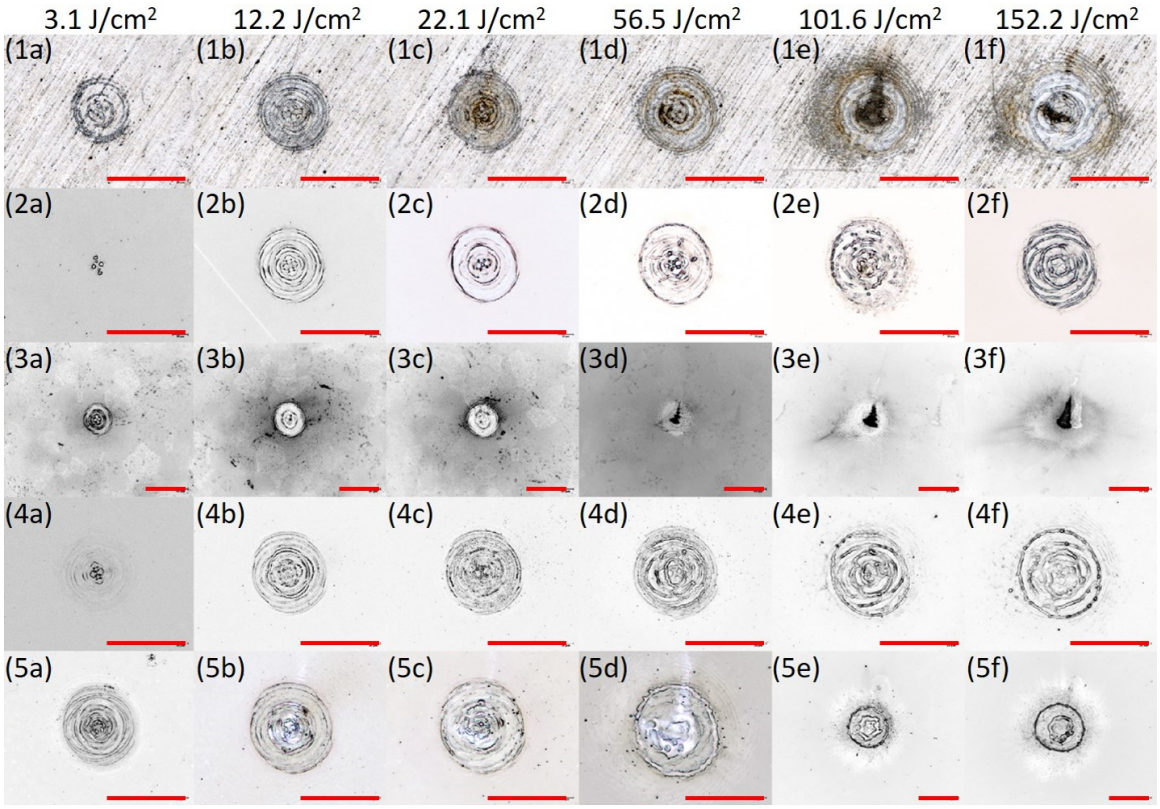

Figure 25. Optical microscopy images of laser ablation with λ = 1064 nm, τ_p = 28 μs, $\omega_0 \approx 6.7$ μm, F : varied, Material: Al (row 1), Si (row 2), Ti (row 3), Ge (row 4), InSb (row 5), P = 1 atm, T = 300 K. Red lines in each image are 100 μm in length.

The optical microscopy images show surface features such as diffraction rings, scorch marks, sub-micron droplets, melt displacement, and splatter, as shown in Figure 26. The diffraction rings are consistent with the 22.6 mm circular aperture of the waveplates, and similar effects were seen after 80 ps ablation of steel in Reference [48]. Scorch marks might imply the presence of hydrocarbons on the surface, but a more detailed explanation is not known at this time. A sharp scorch feature can be seen in images 1e and 1f as well as 3d-f of Figure 25. The cause of this feature is unknown. On Al, it is accompa-

nied by broad scorching around the crater, while on Ti, the scorch mark appears with a spatially similar but lighter marking. On both Al and Ti, the sharp scorch mark also coincides with marked asymmetry of the surface features. InSb shows a similar feature in 5d, but the scorching is light and there is no increase in asymmetry like with Al and Ti. Droplets appear to have been re-deposited in solid phase with no other signs of liquid attributes, and sub-micron sized droplets are potentially an indication of explosive boiling, or phase explosion[30]. In Figure 26(c) there are approximately 65 droplets with diameter $d < 1$ μm and approximately 20 with $d > 1$ μm. Typical droplet sizes are between 0.5 and 1 μm.

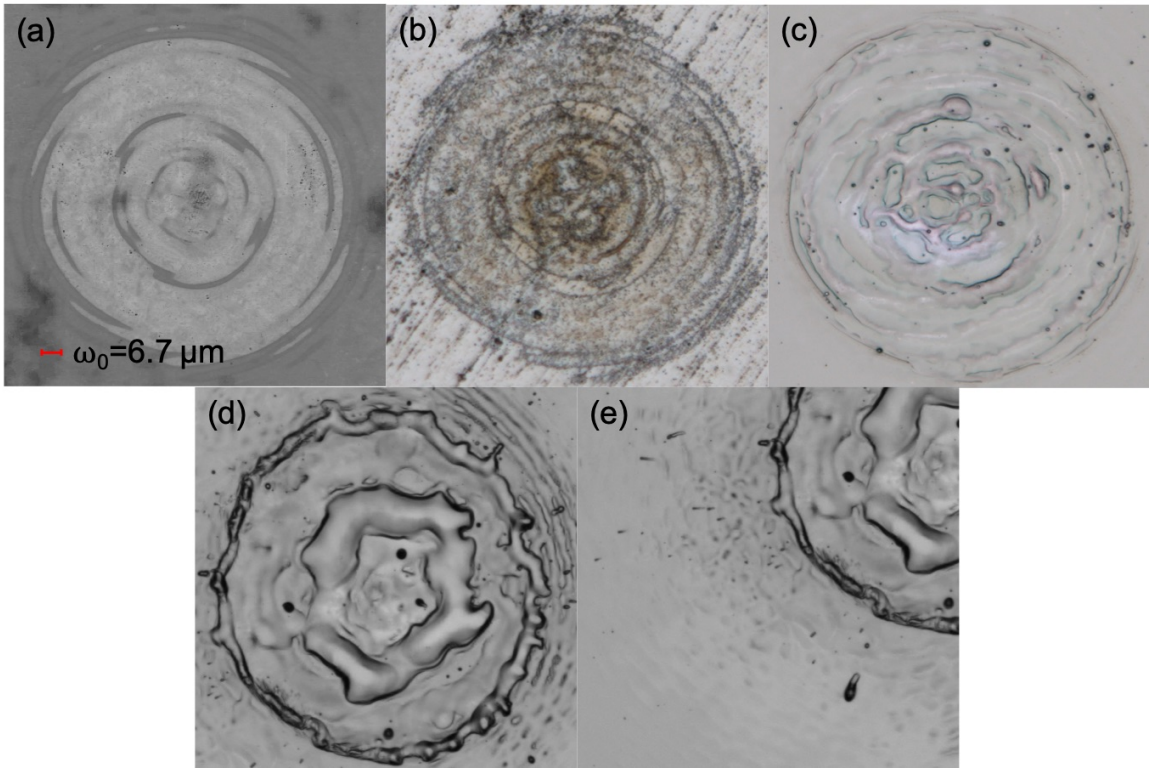

Figure 26. Damage effects from ps laser ablation. $\lambda = 1064$ nm, $\tau_p = 28$ μs, $\omega_0 \approx 6.7$ μm, (a) diffraction rings on Si at $F = 12.2$ J/cm^2, (b) scorch marks on Al at $F = 22.1$ J/cm^2, (c) sub-micron droplets on InSb at $F = 22.1$ J/cm^2, (d) melt displacement on InSb at $F = 101.6$ J/cm^2, and (e) splatter on InSb at $F = 101.6$ J/cm^2, $P = 1$ atm, $T = 300$ K.

Melt displacement presents as a smoothed surface with obvious liquid-phase mo-

tion that has been cooled in place. There may be droplet-like features but they are still connected to the displaced melt front. In Figure 26(d) there are two distinct melt flow rings. The first (inner) ring starts approximately 13 μm from the crater center, and has a thickness of approximately 23 μm. The outer melt ring begins 53 μm from center and is nearly 5 μm thick. Finally Figure 26(e) shows splatter evidenced by droplets (the largest being just over 3 μm in diameter and almost 90 μm from crater center) that were clearly disconnected from the melt front and re-deposited some distance away still in the liquid phase. Splatter will often include liquid-phase tails showing the path of ejection, with higher aspect ratio splatter indicating higher ejection velocities. Comparable size splatter features (i.e. a few microns in diameter and tens of microns from crater center) have been seen in nanosecond ablation in Si, with increasing irradiance leading to splatter being thrown further from the crater with longer liquid-phase tails[29].

At low fluences, the damage outside of the central area was mostly superficial for all materials, and the deepest portion of the crater corresponded to the peaks of the TEM_{02} mode. At higher fluences the deepest portion of the crater was still in this central region for all materials, but the specific mode features were distorted by melt displacement. The high fluence spots on InSb include a smooth central crater with no trace of the beam spatial profile. The laser confocal microscope measurements provide three-dimensional spatial profiles of the craters. Figure 27 shows a two-dimensional slice across the TEM_{40} mode in Figure 24, showing the crater depth profile with maximum crater depth, h_m (dashed line), volume of the crater below the surface, V_- (blue fill), and volume of material above the surface, V_+ (red fill). Figure 28 shows the maximum crater depth, h_m, for each material.

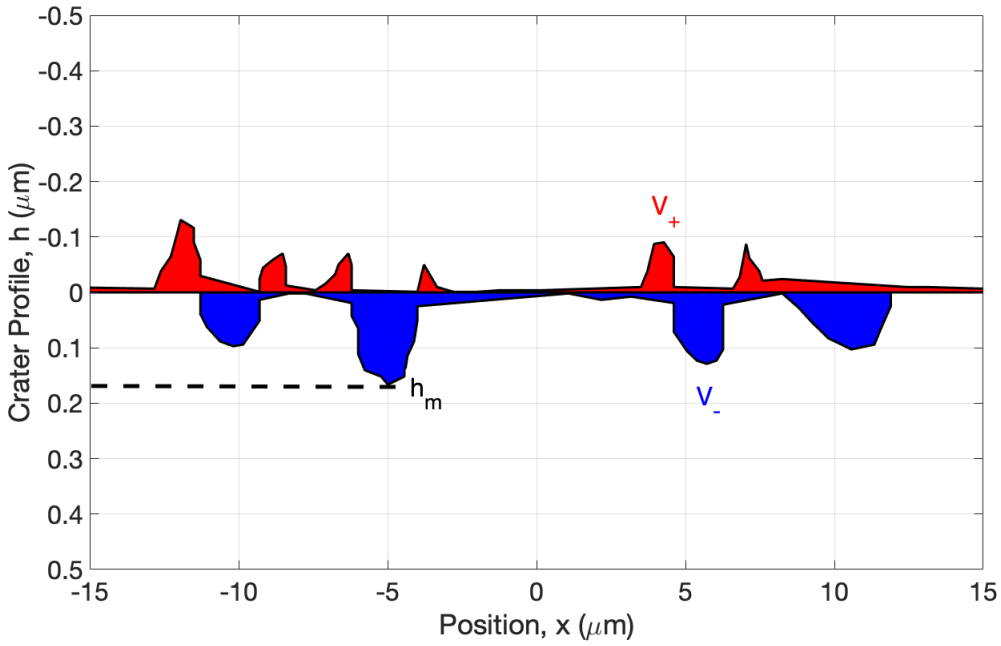

Figure 27. Measured crater depth profile. $\lambda = 1064$ nm, $\tau_p = 28$ μs, $\omega_0 \approx 6.7$ μm, $F = 3.1$ J/cm^2, Material: Si, $P = 1$ atm, $T = 300$ K.

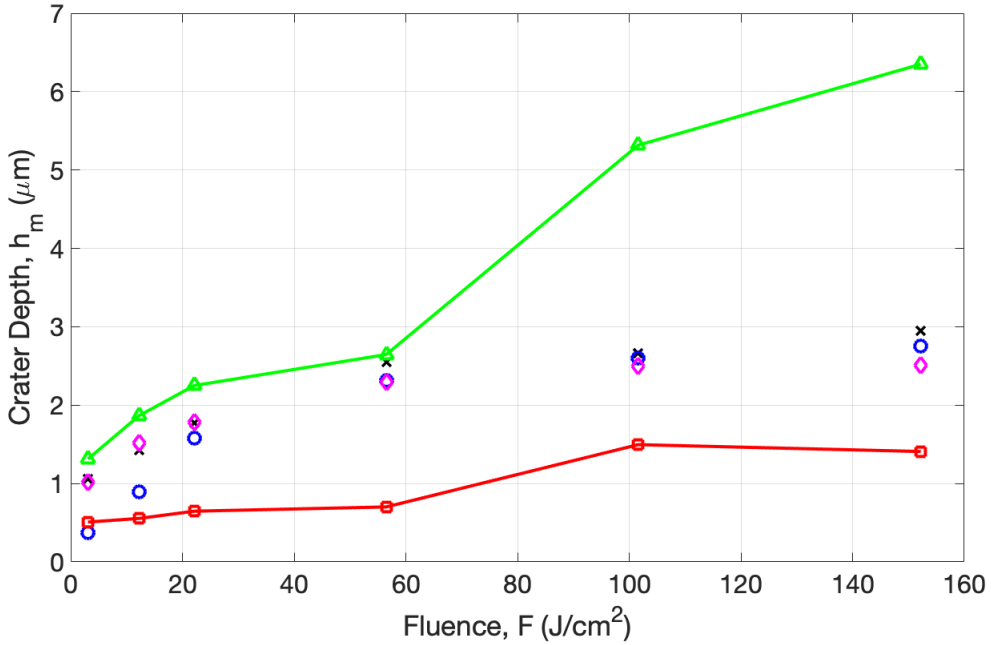

Figure 28. Measured crater depths, h_m. $\lambda = 1064$ nm, $\tau_p = 28$ μs, $\omega_0 \approx 6.7$ μm, F : varied, Material: Al (×), Si (○), Ti (□), Ge (♢), InSb (△), $P = 1$ atm, $T = 300$ K.

With the exception of the minimum crater depth of 370 nm occurring on Si at a fluence of 3.1 J/cm^2, all of the crater depths were between Ti (red line) and InSb (green line). Si has the highest initial growth rate at low fluence, while Ti has the lowest. The maximum crater depth was 6.35 μm on InSb with a fluence of 152.2 J/cm^2. From the lowest to highest fluence (an increase of approximately 49×), max crater depth increased on InSb and Ti by a factor of 4.8 and 2.9, respectively. This plateauing is well known in the nanosecond regime, and was seen in Chapter 3 at a pulse duration of 84 ps, as well.

Table 4 shows relevant length and fluence scales to help interpret the crater measurements: the covalent radius in solid phase (r_a), absorption depth (α^{-1}), thermal diffusion length ($L = \sqrt{\kappa t}$), thermal diffusion time ($t_d = d^2/\kappa$), melt fluence threshold (F_m), and heat of vaporization (L_v).

In terms of atomic layers ablated (i.e. h_m/r_a), the minimum was 3×10^3 occurring on Ti at a fluence of 3.1 J/cm^2, and the maximum was 4.5×10^4 on InSb at a fluence of 152.2 J/cm^2. Si has the largest absorption depth (at room temperature) and the smallest crater depth, h_m, at the lowest fluence. The high initial slope for Si is likely due to the well-known sharp increase of absorption coefficient with temperature[47]. Al has the smallest absorption depth, but also the highest reflectivity. The thermal diffusion length of Ti is the smallest by a factor of 2, and the craters were almost a factor of 2 smaller as well. However, InSb had the largest h_m by far, and its thermal diffusion length is comparable to Ge. With the exception of Ti, the crater depths do scale somewhat similarly

Table 4. Solid-phase material parameters and relevant physical scales

	Al	Si	Ti	Ge	InSb	Source
r_a (pm)	121	111	160	120	141	[57]
α^{-1} (nm)	8	1×10^6	21	714	233	[58, 59, 60, 61, 42]
L (nm), $t_p = 28$ps	24.5	23	7	15.5	17.5	calculated
t_d (ps), $d = 1$ μm	725	825	9275	1775	1450	calculated
F_m (mJ/cm^2), $t_p = 28$ps	5.3	19.1	2.7	0.6	2.2	calculated
L_v (kJ/g)	10.5	12.8	8.85	4.57	1.86	[62, 63, 63, 63, 62]

to thermal diffusion time, but still no clear trend. The lowest fluence is higher than the melt threshold (calculated from one-dimensional energy balance) for all materials. The heat of vaporization will be discussed later in terms of the ablation efficiency.

The crater depths of Al, Si, and Ge are very similar in both magnitude and plateauing with increasing fluence. The plateauing is indicative of a decrease in ablation efficiency, e.g. more photons are needed to remove one additional atom from the material. Ti and InSb, however, show threshold behavior between a fluence of 56.5 and 101.6 J/cm^2, where h_m increases by 113% and 101%, respectively. In Figure 25, these fluences correspond to the onset of significant scorching on Ti and dramatically increased melt displacement on InSb.

Before further evaluating the hole depths and associated phenomenology, it is worth examining the crater volumes. Figures 29 and 30 show the measured volume below the surface, V_-, and volume above the surface, V_+, respectively. In contrast with hole depth, the volume below the surface and the volume above the surface increased linearly for each material. InSb exhibits larger volume growth rate, consistent with larger hold depths. However, Ti has larger crater volume than Al, Si, and Ge for each fluence, despite having significantly more shallow craters. The trends are similar for Al, Si, and Ge, just as with crater depth. The slope for V_+ is inversely proportional to material surface tension (see Table 6), and the slope for V_- is inversely proportional to the enthalphy $H = \rho C T_m + L_m$ (see Table 3). At the higher fluences, the ratio V_+/V_- is approximately 0.7 for all materials (except Ti), which will be discussed in greater detail later. The craters on Ti had substantially higher statistical uncertainty than the other materials, especially at the lower fluence points, so it will be omitted from most of the remaining analysis.

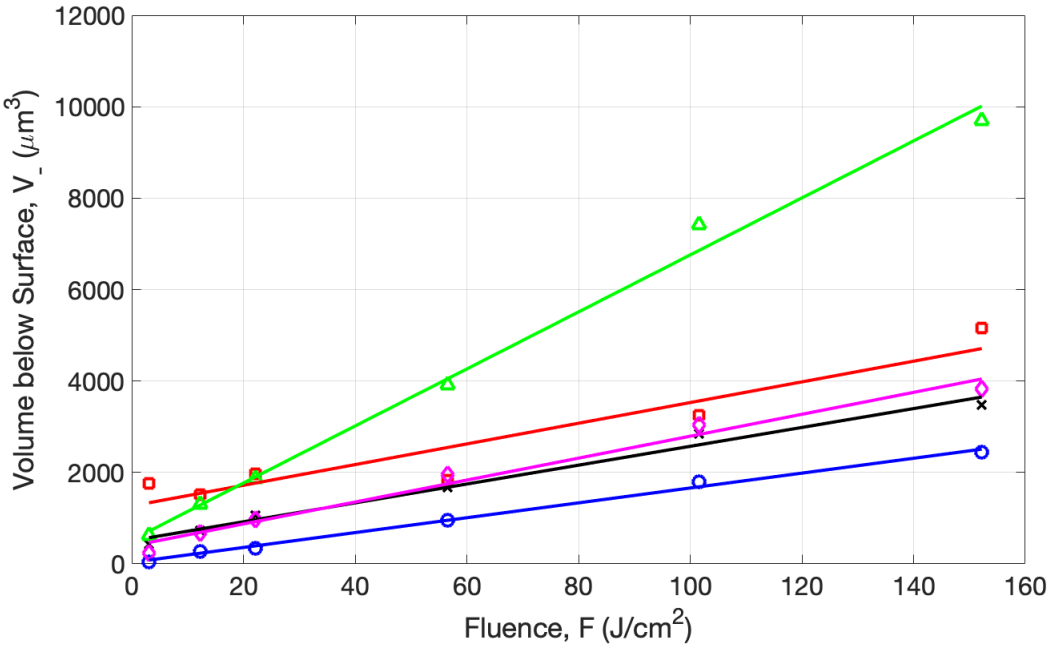

Figure 29. Measured crater volume below surface, V_{-}. $\lambda = 1064$ nm, $\tau_p = 28$ μs, $\omega_0 \approx 6.7$ μm, F : varied, Material: Al (×), Si (○), Ti (□), Ge (◊), InSb (△), $P = 1$ atm, $T = 300$ K.

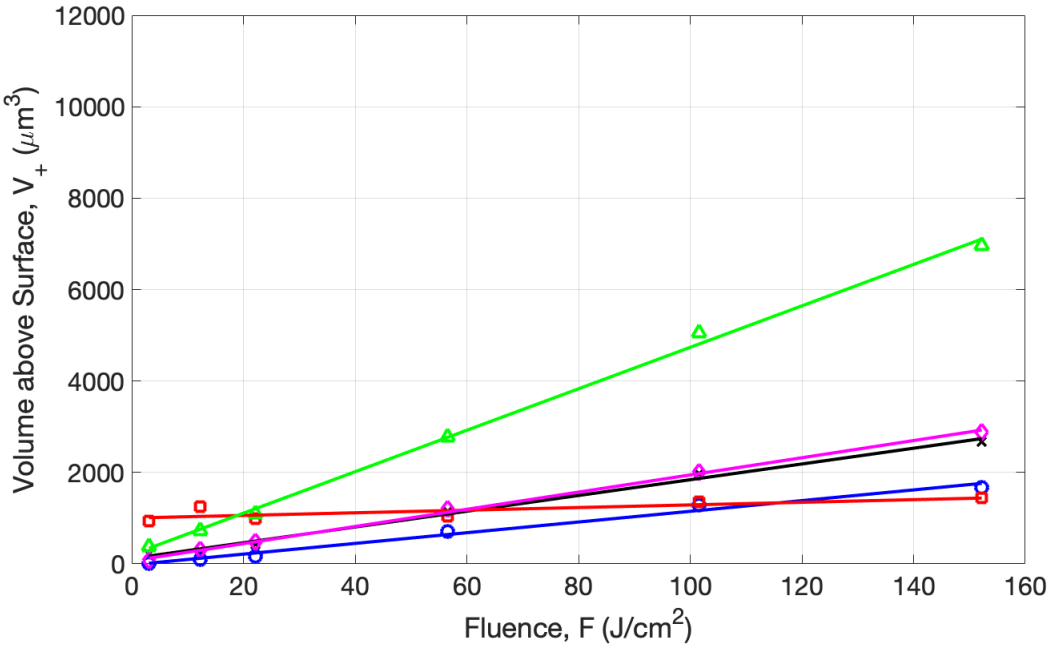

Figure 30. Measured crater volume above surface, V_{+}. $\lambda = 1064$ nm, $\tau_p = 28$ μs, $\omega_0 \approx 6.7$ μm, F : varied, Material: Al (×), Si (○), Ti (□), Ge (◊), InSb (△), $P = 1$ atm, $T = 300$ K.

4.3.3 Ablation in Vacuum

Ge was also ablated in vacuum, and background pressure was varied from 2.2×10^{-3} to 6 Pa ($2.2 \times 10^{-8} - 6 \times 10^{-5}$ atm or $1.6 \times 10^{-5} - 6 \times 10^{-2}$ Torr). Figure 31 shows high fluence craters formed in vacuum and air. At the lowest pressure, the low fluence shots on Ge appeared visually similar to the low fluence shots at ambient air pressure. At higher fluences, the craters in vacuum show more droplets and less well-defined melt flow rings. In vacuum, some melt flow appears to have re-solidified radially, while some melt appears to have left the surface in the normal direction. The craters in air show much smoother melt features with less well-defined directions. The crater depths (h_m) in vacuum and air are similar up to approximately 20 J/cm^2, at which point the craters in vacuum grow to nearly 17% deeper, as shown in Figure 32. Within the experimental uncertainty, h_m in vacuum is less than 17% greater than in air. In both vacuum and air, h_m plateaus with increasing fluence, approaching 3 μm and 2.5 μm, respectively. The mean free path in air at standard temperature and pressure is approximately 68 nm, while in vacuum it is approximately 100 mm. The plume stopping distance also scales inversely with background pressure[64]. Thus, the difference between craters formed in air and vacuum are expected to be due to plume confinement and recondensation effects, as will be discussed later.

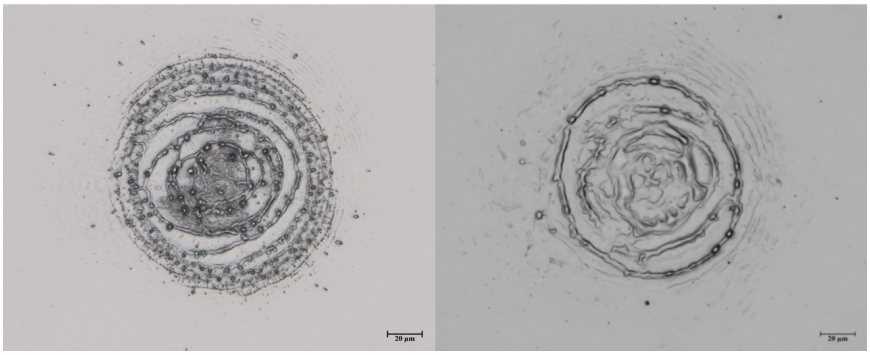

Figure 31. Optical microscopy of craters. $\lambda = 1064$ nm, $\tau_p = 28$ μs, $\omega_0 \approx 6.7$ μm, (left) $F = 122.5$ J/cm^2 and (right) $F = 152.2$ J/cm^2, Material: Ge, (left) $P = 2.2 \times 10^{-3}$ atm and (right) $P = 1$ atm, $T = 300$ K.

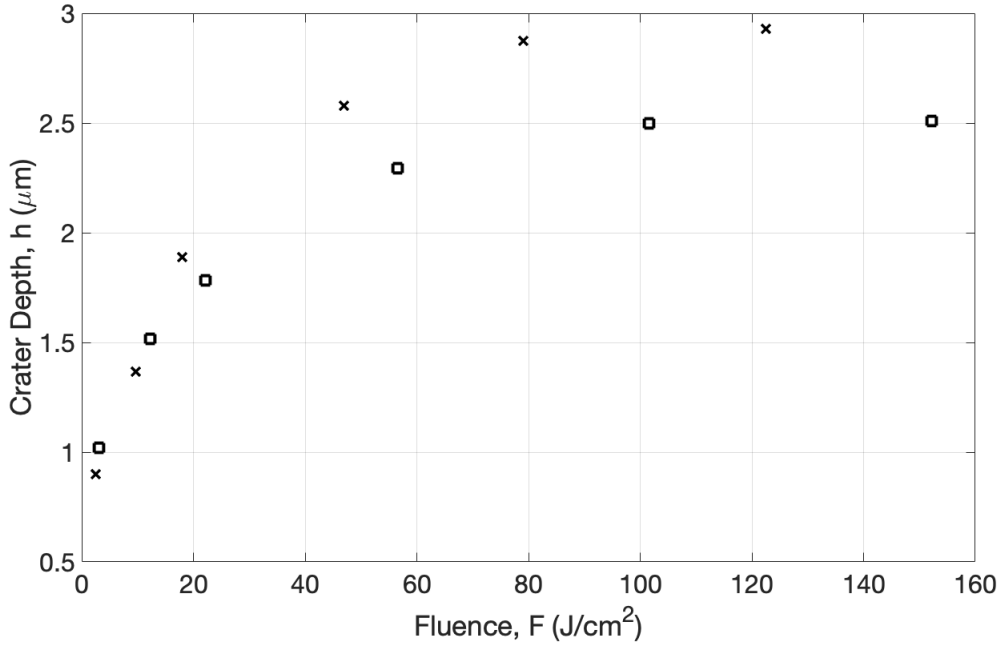

Figure 32. Measured crater depth, h_m. $\lambda = 1064$ nm, $\tau_p = 28$ μs, $\omega_0 \approx 6.7$ μm, F : varied, Material: Ge, (□) $P = 1$ atm and (×) $P = 2.2 \times 10^{-3}$ atm, $T = 300$ K.

Figures 33 and 34 show the crater volume beneath the surface, V_-, and volume above the surface, V_+, as a function of fluence in air and vacuum. The volume above and below the surface grows approximately linearly with fluence for all materials in air, with the slopes for volume below surface being higher. However, in vacuum, V_- grows faster at low fluences than in air. V_- also appears to plateau in vacuum, with the growth rate slowing above $F \approx 40-50$ J/cm^2. The crater volume above the surface, V_+, is comparable in vacuum and air up to $F \approx 40-50$ J/cm^2, at which point V_+ in vacuum grows much slower than in air. Above $F \approx 100$ J/cm^2, V_+ in vacuum is greater than 35% lower than in air. Note that the approximate fluence value above which V_- starts to plateau in vacuum is also where V_+ in vacuum substantially deviates from V_+ in air. Thus, the efficiency of the ablation or mass removal process clearly depends on background pressure as will now be discussed.

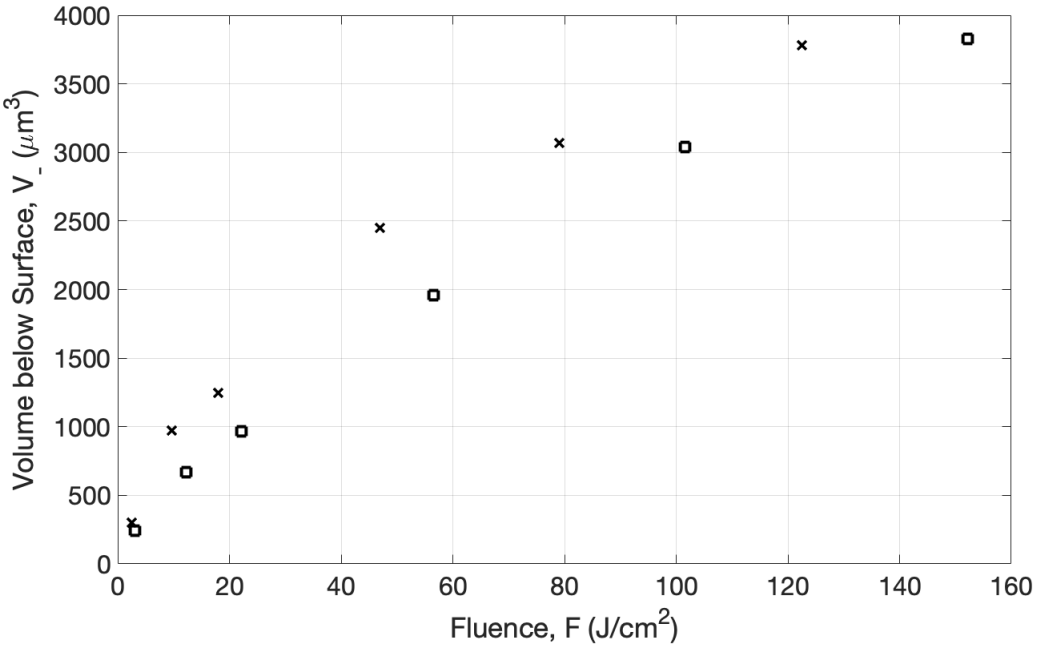

Figure 33. Measured volume below the surface, V_{-}. $\lambda = 1064$ nm, $\tau_p = 28$ μs, $\omega_0 \approx 6.7$ μm, F : varied, Material: Ge, (□) $P = 1$ atm and (×) $P = 2.2 \times 10^{-3}$ atm, $T = 300$ K.

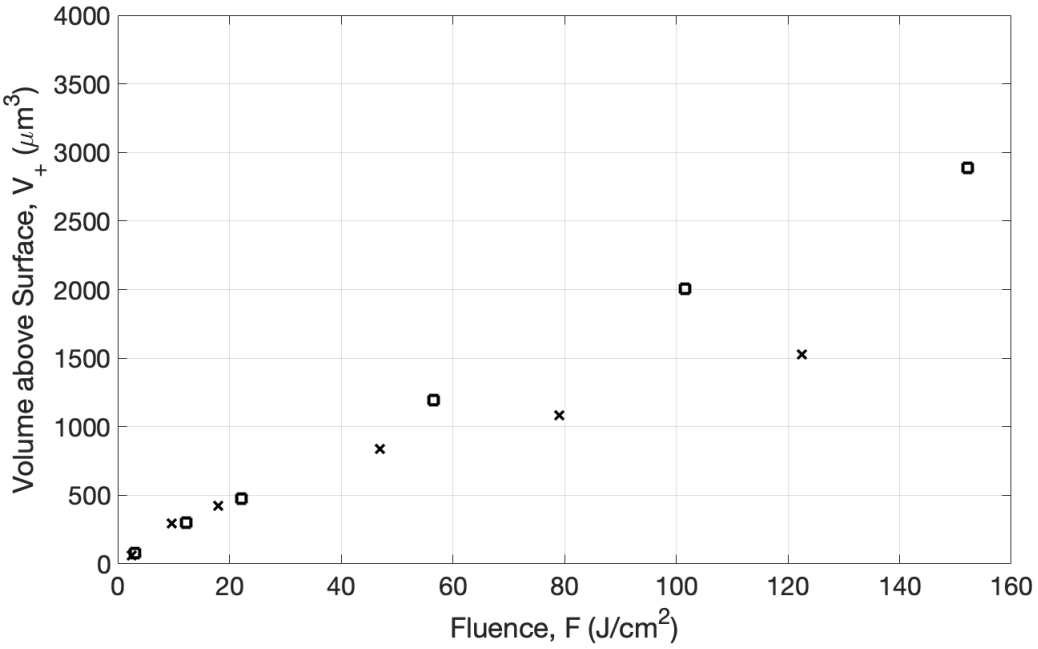

Figure 34. Measured volume above the surface, V_{+}. $\lambda = 1064$ nm, $\tau_p = 28$ μs, $\omega_0 \approx 6.7$ μm, F : varied, Material: Ge, (□) $P = 1$ atm and (×) $P = 2.2 \times 10^{-3}$ atm, $T = 300$ K.

4.3.4 Mass Removal and Ablation Efficiency

The ablation efficiency, defined as atoms removed per incident photon was calculated as

$$\eta = \frac{\text{atoms}}{\text{photon}} = \frac{\rho(V_- - V_+)/(M/N_A)}{E/(h\nu)} \tag{13}$$

where ρ is the solid phase density, V_- and V_+ are the measured volume below and above the surface, M is the molar mass in kg/mol, N_A is Avagadro's number, E is the pulse energy in Joules, h is Planck's constant, and ν is the frequency of the laser light. Figure 35 shows the calculated ablation efficiency for all materials in air except Ti, due to the aforementioned statistical variability in the volume measurements.

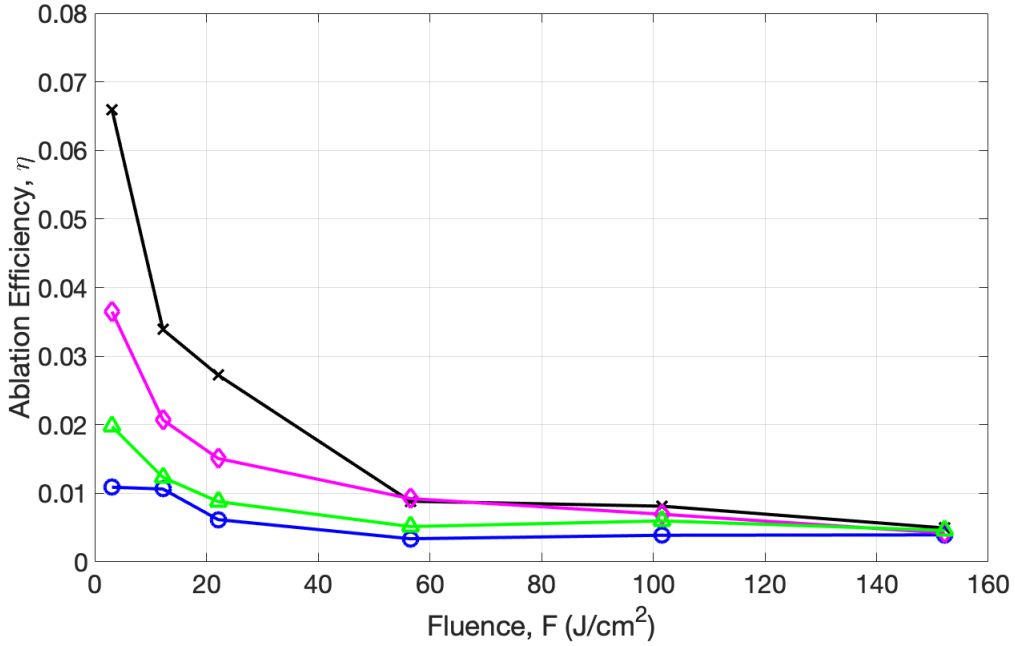

Figure 35. Ablation efficiency, η. $\lambda = 1064$ nm, $\tau_p = 28$ μs, $\omega_0 \approx 6.7$ μm, F : varied, Material: Al (×), Si (∘), Ge (◊), InSb (△), $P = 1$ atm, $T = 300$ K.

It can be seen that Al has the highest efficiency at low fluence, with $\eta = 0.066$ and Si has the lowest with $\eta = 0.011$. At the highest fluence, the ablation efficiency for all materials decreases and approach similar values between $4 - 5 \times 10^{-3}$. An upper bound

on the ablation efficiency can be found by using the heat of vaporization (see Table 4) to convert the measured mass removed to the energy required to remove it purely by evaporation. With this approach, $\eta_{lim} = 26 - 44\%$, which is substantially higher than measured. There is no observed correlation between η and L_v: the heat of vaporization of Si is 5 times greater than InSb, but the efficiency is half. This implies that the primary mass removal mechanism is not vaporization alone, as will be discussed later.

The ablation efficiency at low fluence is inversely proportional to absorption depth, as seen in Figure 36, and proportional to viscosity at high fluence, as shown in Figure 37. It should be noted that these are slight dependencies: absorption depth varies over five orders of magnitude, while the low fluence ablation efficiency only decreases by approximately a factor of six. Furthermore, the nominal liquid phase viscosity of the materials only varies by less than a factor of three, and the high fluence ablation efficiency only increases by about a quarter.

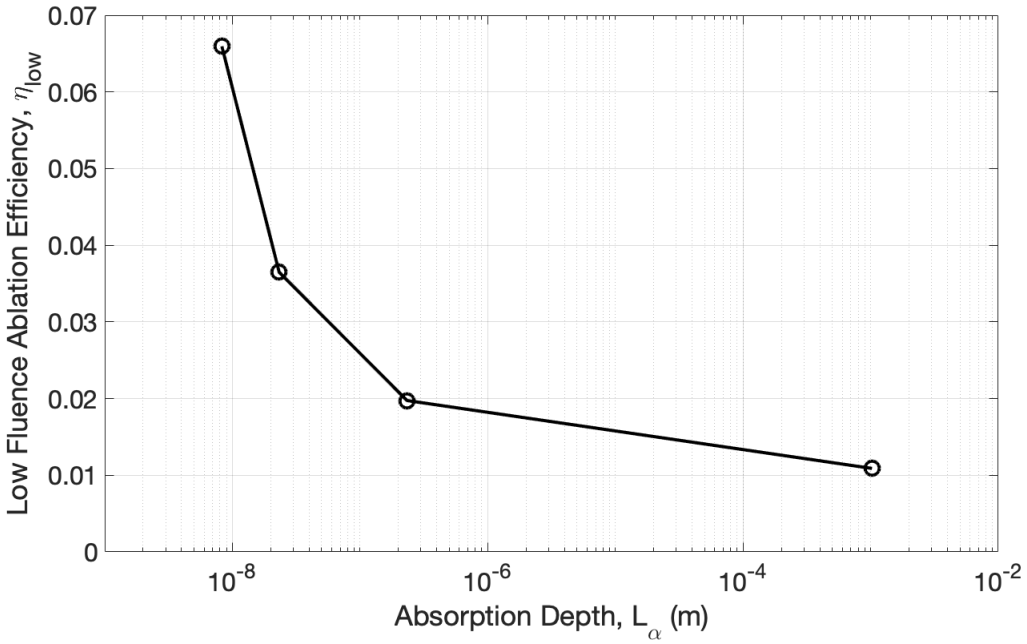

Figure 36. Low fluence ablation efficiency versus optical absorption depth. $\lambda = 1064$ nm, $\tau_p = 28$ μs, $\omega_0 \approx 6.7$ μm, F : varied, Material: varied, $P = 1$ atm, $T = 300$ K.

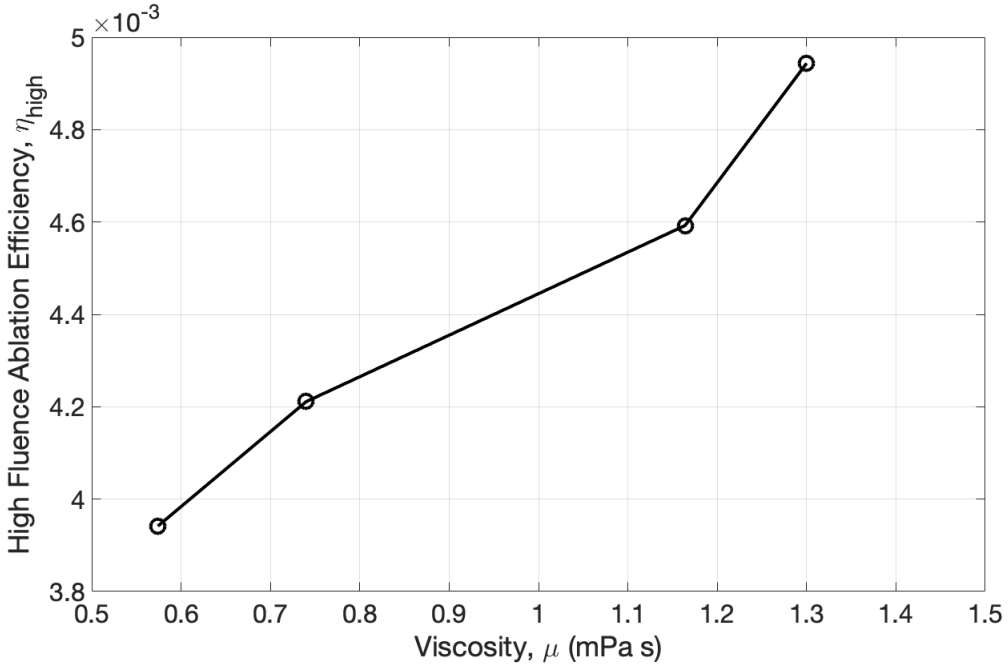

Figure 37. High fluence ablation efficiency versus viscosity. $\lambda = 1064$ nm, $\tau_p = 28$ μs, $\omega_0 \approx 6.7$ μm, F : varied, Material: varied, $P = 1$ atm, $T = 300$ K.

Figure 38 compares the ablation efficiency on Ge in vacuum and air. The efficiency curves in air and vacuum have similar shape, but the efficiency is nearly two times higher on average in vacuum at each fluence. The efficiency is higher in vacuum because there is less material volume above the surface, as shown by the volume ratio V_+/V_- in Figure 39. It can be seen that the volume ratio is very different for each material at low fluence, ranging from 0.17 on Si to 0.62 on InSb. However, at high fluences, the ratio converges for all materials in air to approximately 0.7. The ratio for Ge in vacuum is flatter than in air and is 0.4 at the highest fluence compared to 0.75 in air. Thus, while crater depth and volume below the surface are comparable on Ge in vacuum and air, the almost factor of two difference in the volume ratio is due to the reduction in displaced and redeposited material on the surface.

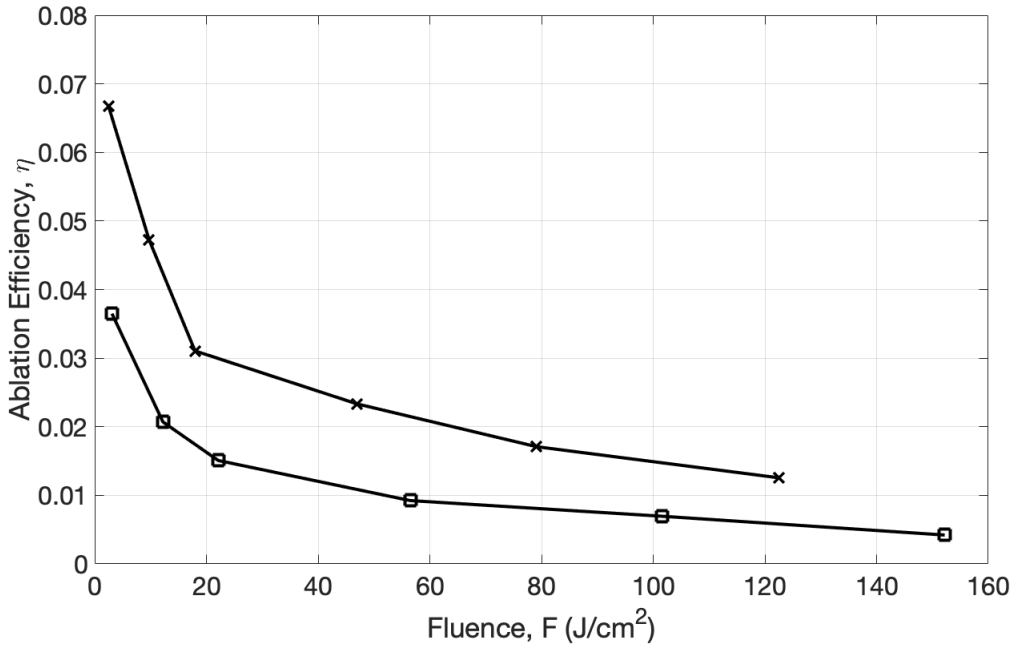

Figure 38. Ablation efficiency, η. $\lambda = 1064$ nm, $\tau_p = 28$ μs, $\omega_0 \approx 6.7$ μm, F : varied, Material: Ge, (□) $P = 1$ atm and (×) $P = 2.2 \times 10^{-3}$ atm, $T = 300$ K.

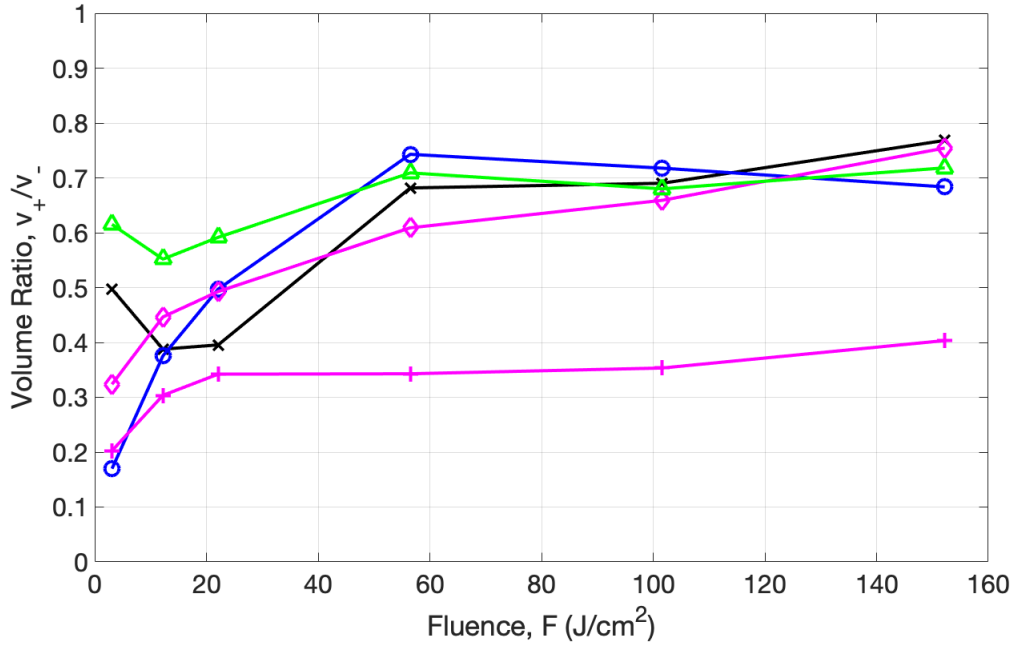

Figure 39. Volume ratio, V_+/V_-. $\lambda = 1064$ nm, $\tau_p = 28$ μs, $\omega_0 \approx 6.7$ μm, F : varied, Material: Al (×), Si (○), Ge (♢, +), InSb (△), $P = 1$ atm and (+) $P = 2.2 \times 10^{-3}$ atm, $T = 300$ K.

4.3.5 Results Summary

Table 5 summarizes the key measured results. Craters were marked by melt displacement, droplets, splatter, and scorch marks at high fluence. Crater depth, h_m, on Ti increased the least with fluence, while h_m on InSb grew the most. In air, V_+ and V_- grew linearly with fluence with slopes inversely proportional to surface tension and volumetric enthalphy, respectively. In vacuum, h_m grew faster than in air above $F \approx 20$ J/cm^2 and plateaus approximately 17% higher, while V_- grows faster initially in vacuum but starts to roll over above $F \approx 40-50$ J/cm^2. At low fluences, V_- is comparable in air and vacuum, but starts to roll over above $F \approx 40-50$ J/cm^2. Ablation efficiency in air is inversely proportional to absorption depth at low fluence and proportional to viscosity at high fluence. The volume ratio, V_+/V_-, increases with fluence and plateaus to ≈ 0.7 for all materials. Ablation efficiency increases in vacuum compared to ambient air, but V_+/V_- decreases and plateaus to ≈ 0.4.

Table 5. Results Summary

	Al	Si	Ti	Ge (air)	Ge (vac)	InSb
min h_m (μm)	1.06	0.37	0.51	1.02	0.9	1.31
max h_m (μm)	2.95	2.76	1.41	2.51	2.93	6.35
min l_a (10^4 layers)	0.8	0.3	0.3	0.8	0.7	0.9
max l_a (10^4 layers)	2.5	2.5	0.9	2	2.4	4.5
min V_- (μm^3)	434	85	1754	245	303	619
max V_- (μm^3)	3474	2509	5151	3828	3784	9692
min V_+ (μm^3)	216	16	1012	125	61	381
max V_+ (μm^3)	2669	1761	1440	2927	1526	6960
min η ($\frac{\text{atoms}}{\text{photon}}$)	0.0049	0.0039	-	0.0042	0.013	0.0046
max η ($\frac{\text{atoms}}{\text{photon}}$)	.066	0.011	-	0.036	0.067	0.02

4.4 Discussion

4.4.1 Non-dimensional Scaling Variables

Before discussing the numerical simulations of the ablation conditions in this study, it is useful to briefly discuss the crater depth results in terms of the non-dimensional variables from Chapter 3. Recall that a set of three variables: h^*, t^*, and f^* were defined as the non-dimensional hole depth, pulse duration, and fluence, respectively, using the one-dimensional heat transfer equation. It was found that for $f^* \gg 1$ and $t^* \ll 1$, $h^* > 1$. As pulse duration decreased, craters many times the thermal diffusion length during the pulse were created.

Figure 40 shows data from the current study converted to the non-dimensional variables, h^* and f^*. The non-dimensional hole depth ranges from 8.1 to 183.4 and non-dimensional fluence from 27.4 to 4092.6. The data was fit to the functional form $h^* = a\left(f^*\right)^b$ (see Chapter 3), with $a = 2.65 \pm 0.9$ and $b = 0.48 \pm 0.05$. The dashed lines are the standard uncertainty on the fit variables.

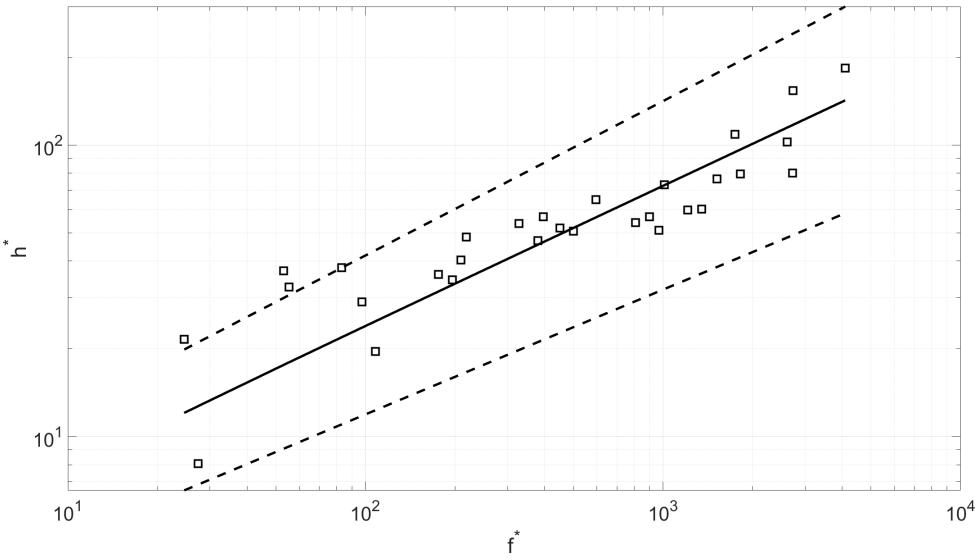

Figure 40. Non-dimensional crater depth, h^*, versus non-dimensional fluence, f^*. λ = 1064 nm, $\tau_p = 28$ μs, $\omega_0 \approx 6.7$ μm, F : varied, Material: varied, $P = 1$ atm, $T = 300$ K.

Figure 41 shows h^* from the current study compared to the aggregate (i.e. all materials grouped together) data set from Chapter 3 (see Figure 21). The 28 ps data (157 ns $< t^* <$ 2 μs using the rectangle with area $A = 4\omega_l\omega_m$ in place of ω_0^2 in Equation 11) continues the trend seen in Figure 22 in Chapter 3, where h^* increases as t^* decreases. The maximum f^* is much lower in the current study compared to Chapter 3, i.e. 4×10^3 versus 2×10^5. However, the maximum h^* is higher here, at 183 versus 48. In Chapter 3, the exponent of the power-law fit was found to be 0.47 ± 0.06 for $t^* < 0.1$ and for $f^* > 10$. Looking only at the 84 ps pulse duration from Chapter 3, the exponent is 0.49 ± 0.09. Within the uncertainty in the fit variables, the 28 ps data in the current study matches the 84 ps data from Chapter 3.

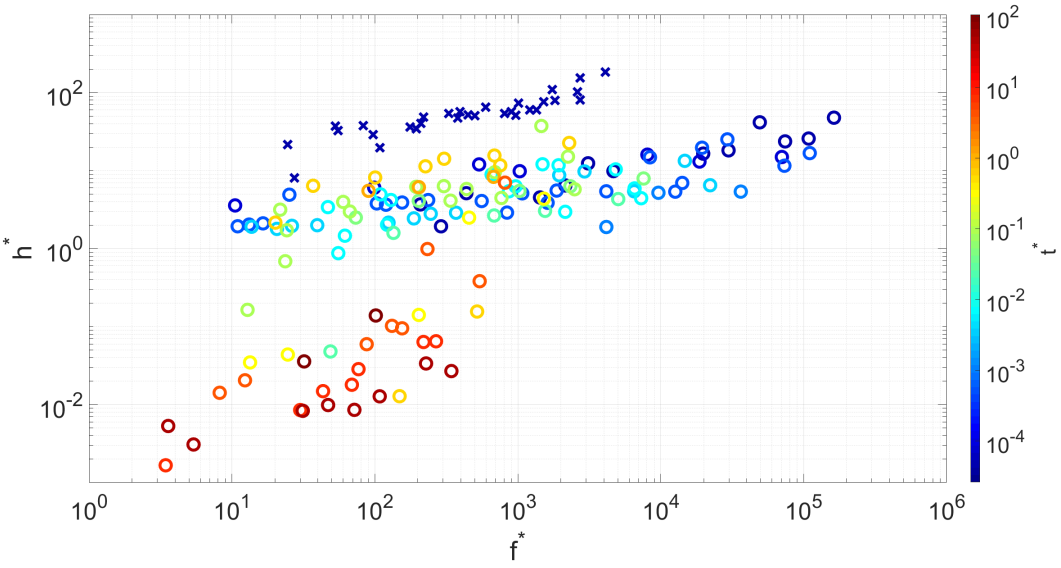

Figure 41. Non-dimensional crater depth, h^*, versus non-dimensional fluence, f^*. λ = 1064 nm, (∘) 26 μs $< t^* <$ 106 s and (×) 157 ns $< t^* <$ 2 μs, (∘) $\omega_0 \approx$ 10 μm and (×) $\omega_0 \approx$ 6.7 μm, F : varied, Material: varied, P = 1 atm, T = 300 K.

The shielding coefficient, defined as b^{-1} in Chapter 3, is shown in Figure 42. The 28 ps data, although multi-mode, follows the trend observed at 84 ps in that shielding is reduced by a factor of approximately 2-3 from the peak for each material. It will

be seen in the next section that while shielding explains the reduction in ablation efficiency seen with increasing fluence under most experimental conditions, other physical mechanisms, such as melt re-flow, can occur in the absence of shielding and cause similar plateauing effects. Furthermore, when compared with single mode TEM_{00} ablation, the multi-mode beams in the current study show increased plateauing, corresponding to a lower value for b, and a higher value for b^{-1}. Thus, the modality of the beam affects the slope of the red circles in Figure 41, with multi-mode beams producing a smaller slope than single mode beams.

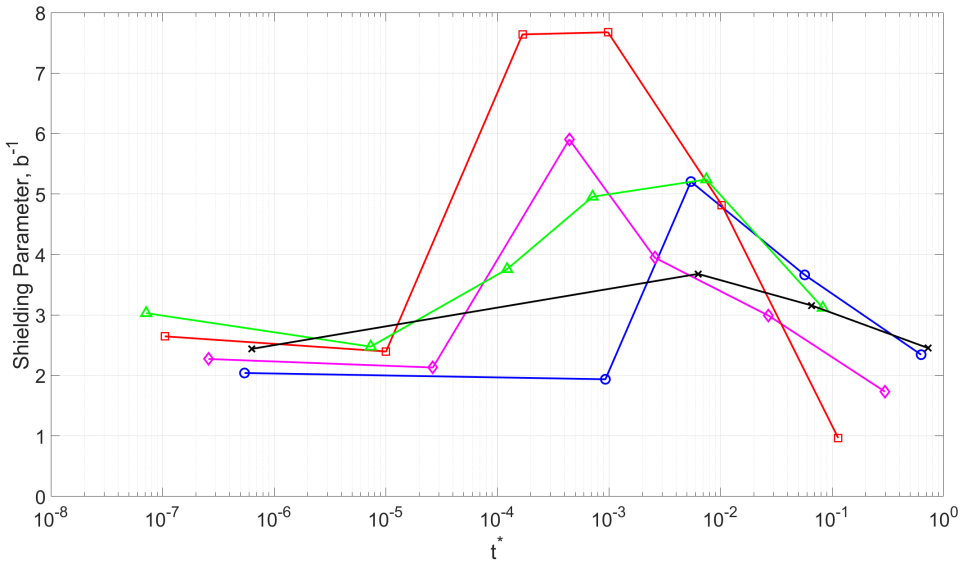

Figure 42. Shielding parameter, b^{-1}, versus non-dimensional pulse duration, t^*. $\lambda = 1064$ nm, τ_p : varied, ω_0 : varied, F : varied, Material: Al (×), Si (○), Ti (□), Ge (◇), InSb (△), $P = 1$ atm, $T = 300$ K.

4.4.2 Simulations

In order to fully understand the differences in ablation efficiency across materials and especially on Ge in air and vacuum, the DEIVI simulation environment was used to model the experimental conditions. DEIVI was developed by the Johns Hopkins University Applied Physics Laboratory for the Directed Energy Directorate of the Air Force

Research Laboratory based on phenomenology and numerical methods described in References [15, 65, 66, 67, 68]. DEIVI numerically solves a set of coupled equations governing: material heating, phase change, evaporation, recoil pressure, plasma formation, plasma shielding, melt flow, and moving interface between different phases[69]. The discretized radially-symmetric condensed phase and gas dynamics are fully coupled with an artificially thin Knudsen layer[65, 67, 68]. Key time-resolved outputs include: the spatial locations of the phase boundaries; plume speed, temperature, and pressure; and melt flow speed and direction.

The laser radiation has normal incidence with no focusing of the beam, and absorption in the material (condensed, liquid, and gas phases can absorb the laser energy) is described by Beer's law. Heat transfer in the material is modeled using the Fourier heat conduction equation with convective transport, and is solved in both liquid and solid phases. The volumetric enthalpy formulation is used to solve for H and T in both phases simultaneously. The melt phase flow is described by the incompressible viscous Navier-Stokes equation, and the pressure driving the flow is taken to be the maximum of the recoil pressure from evaporation and the pressure in the plume. The gasdynamics are modeled with the Euler equations assuming local thermodynamic equilibrium. The plume is assumed to contain only the ablated atomic and ionic species, and the material does not mix with the ambient background gas, i.e. there are no chemical kinetics modeled in the plume. The boundary of the gas dynamics grid is transparent to the plume. At the discontinuity between the melt phase and the plume, a Knudsen layer approach is used as described in Reference [15]. Recondensation effects are not included, and the Knudsen layer conditions are functions only of surface temperature and density. The pressure across the layer is found via the ideal gas law. The background pressure only affects the gas dynamics and not the condensed phase, since the recoil pressure from evaporation is greater than the ambient background pressure for all cases simulated.

The plume is assumed to be ionized by thermal collisions, and photoionization is not included. The ionic population is given by the Saha equation, and inverse Bremsstrahlung is the mechanism by which laser light is absorbed in the plume. Phase explosion is modeled by DEIVI, but it is not included in this analysis. There is not convincing visible evidence of phase explosion in the craters, and the homogeneous nucleation times for the materials of interest are not precisely known. Thus it was decided to set the homogeneous nucleation time to be greater than the simulation run time and thereby not include phase explosion effects. The geometry is assumed to be axially symmetric, and the number of points and grid spacing can be independently specified for both the condensed phase grid and the gas dynamics grid. DEIVI implements an adaptive time step to satisfy the Courant-Friedrichs-Lewy stability condition for heat transport, viscous and convective melt flow, and capillary wave speed effects. User-specified temporal and spatial fluence distributions are integrated between each time step in order to supply the correct fluence to the surface grid cells.

One final limitation needs mentioned and regards splatter. The condensed phase grid is doubled in DEIVI to extend above the material interface in order to account for displaced melt effects. Under very intense laser irradiation, the melt can have a high velocity and be ejected far from the crater. Not only does this high melt speed drive up computation time (by reducing the time step as previously mentioned), but the melt is artificially reflected at the boundary of the condensed phase grid. The grid can be enlarged, but computational resource limitations constrain this approach. Grid size (including the temporal aspect) is primarily limited by computer memory and run time is typically dependent on single-core processor clock speed.

Material properties in DEIVI can be temperature-independent or values can be interpolated from user-provided inputs. The solid phase material parameters are given in Table 3 in Chapter 3, and Table 6 lists relevant liquid-phase properties of each material

in this study.

Table 6. Liquid-phase material properties used in DEIVI simulations

	Al	Si	Ti	Ge	InSb
Density, ρ ($kg{\cdot}m^{-3}$)	2375	2570	4000	5600	7030
Thermal Conductivity, K ($W{\cdot}m^{-1}{\cdot}K^{-1}$)	90	56	27	39	18
Heat Capacity, C_p ($J{\cdot}kg^{-1}{\cdot}K^{-1}$)	1127	1037	938	379	283
Viscosity, η (mPa·s)	1.3	0.57	3.0	0.74	0.619
Surface Tension, μ (Pa·m)	0.87	0.874	1.557	0.6	0.29
References	[70, 71]	[72]	[73, 74]	[72]	[72, 75]

Nominal solid phase material parameters were used for $T < T_m$ and constant liquid phase parameters were used for $T > T_m$, evaluated at just below the vaporization temperature. For Si, an absorption coefficient of 10^3 cm^{-1} was used to account for the rapid increase in absorption with temperature[47]. A 16 μm×16 μm grid with uniform spacing of 4 cells/μm and a simulation duration of 300 ns were used after convergence tests were run. The spatial grid was refined until the solution (e.g. crater depth) stabilized, and the max simulation time was increased until no cell contained melt-phase material. The gas dynamics grid was set to the same spatial extent since long term plume evolution far from the material surface was not of interest in this study. The grid spacing corresponded to 250 nm between grid points, which means the laser light was absorbed within the first cell for all materials except Si. The grid spacing is also larger than the thermal diffusion length during the pulse for all materials. The grid spacing is $\sim 3\lambda$ at ambient pressure. There were typically 8 grid points across the crater at higher fluences. At these conditions, simulation run times would approach 24 hours or more, and the requisite convergence tests add even more time. Thus, realistic tradeoffs between simulation resolution and run time were made, and very high resolution runs were not

performed at the time of this writing.

The incident fluence spatial distribution from Figure 27 and a 28 ps full-width half-max Gaussian temporal pulse profile were used. Some minor conversions must be made in order to match fluence in the simulation to measured fluence. First, it was assumed that half of the incident energy was contained in each mode, the measured fluence is divided by 2 before simulating in DEIVI. Second, DEIVI uses the half-width at half-max to define the spatial extent of the fluence distribution, whereas the measured fluence uses the $1/e$ point, so the measured fluence is further divided by $(2.355/2)^2$. Finally, DEIVI normalizes the fluence assuming a TEM_{00} distribution, which can be accounted for by multiplying the measured fluence by a factor of $\omega_l/\omega_0 = \sqrt{2l+1}$. Thus, the conversion is $F_{DEIVI} = F_{meas}/8.32$. Simulations are primarily run with $F < 60$ J/cm^2, because as will be seen, around that fluence, the effects of the TEM_{02} mode and splatter effects become significant for the materials in this study. Above this fluence, the assumption of the radially symmetric beam, the run time increase associated with melt ejection, and the artificial interaction between the melt phase and the simulation boundary reduce the utility of a comparison between simulated and measured data.

Figure 43 shows the low fluence craters on Si produced in DEIVI. The crater pattern matches the incident irradiance pattern, as shown in Figure24. The crater shapes show very good agreement (< 5% normalized root-mean-square deviation) at low fluence and at larger radial distances (i.e. $r > 7$ μm). The inner crater shows signs of displaced melt, and the outer crater is asymmetric, matching the fluence distribution. Since DEIVI models a radially symmetric beam, it does not include contributions from the TEM_{02} mode, which affect the lobe closer to the beam center.

The simulated craters at a fluence of 12.2 J/cm^2, shown in Figure 44, match the order of the measured depths (i.e. Ti is the shallowest and InSb is the deepest). Though the maximum crater depth does not exactly agree with measured data, the relative features

of the different materials do. InSb shows the most displaced melt, while Ti shows the least, which is in agreement with Figure 25. Furthermore, the maximum crater depth, h_m, is similar for Al and Ge, in accordance with Figure 28.

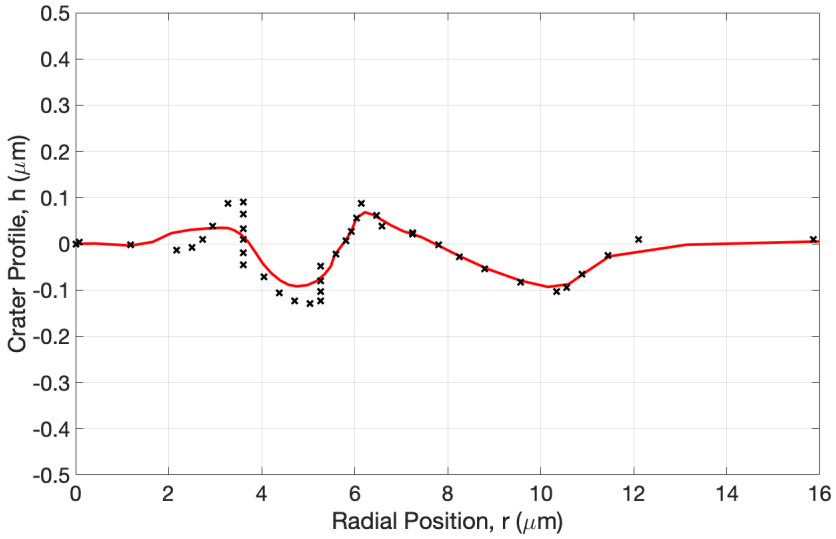

Figure 43. Simulated (red) and measured (×) craters. $\lambda = 1064$ nm, $\tau_p = 28$ μs, $\omega_0 \approx 6.7$ μm, $F = 22.1$ J/cm^2, Material: Si, $P = 1$ atm, $T = 300$ K.

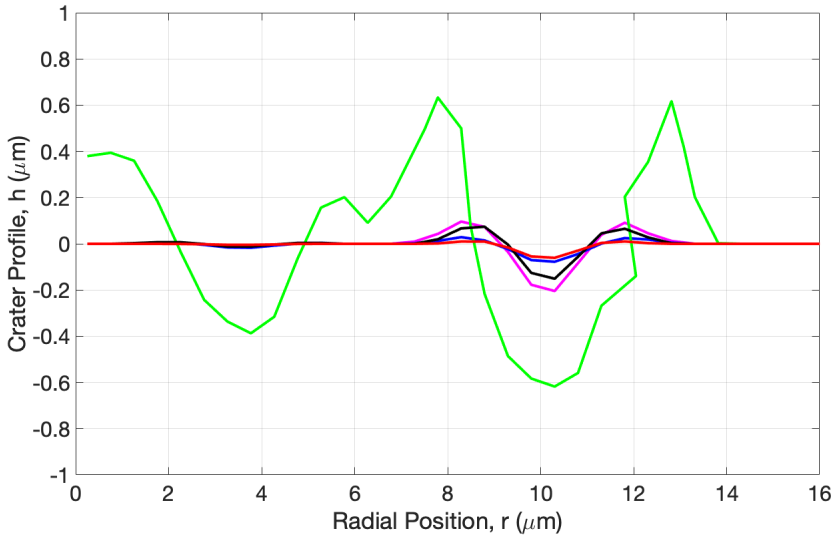

Figure 44. Simulated craters. $\lambda = 1064$ nm, $\tau_p = 28$ μs, $\omega_0 \approx 6.7$ μm, $F = 12.2$ J/cm^2, Material: Al (-), Si (-), Ti (-), Ge (-), InSb (-), $P = 1$ atm, $T = 300$ K.

Since only one mode is simulated, the melt flow effects from the TEM_{02} mode are not included. Furthermore, the TEM_{02} has fewer lobes than the TEM_{40} mode, so the energy is more concentrated. The craters are made at the site of each lobe and are primarily formed by recoil-induced melt displacement. Since each lobe is not completely symmetric, melt flow occurs primarily from the outer lobe into the inner lobe. These effects due to the multi-mode structure of the beam cause a plateauing of crater depth at a lower fluence compared to a TEM_{00} mode, as shown in Figure 45.

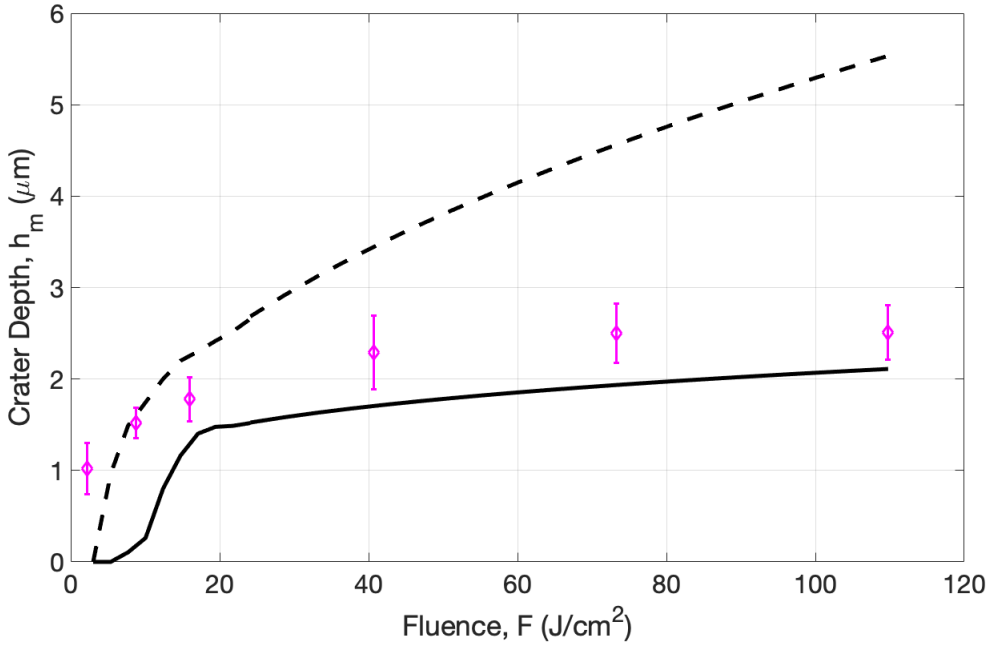

Figure 45. Simulated crater depths using (dashed line) TEM_{00} and (solid line) TEM_{40} modes, and (♢) measured crater depth, h_m. $\lambda = 1064$ nm, $\tau_p = 28$ μs, $\omega_0 \approx 6.7$ μm, F : varied, Material: Ge, $P = 1$ atm, $T = 300$ K.

The multi-mode beam appears to have a higher threshold for significant mass removal, with a 1 μm crater being formed at a fluence of $F \approx 19$ J/cm^2 compared to a 1 μm crater being formed with the TEM_{00} beam at a fluence of $F \approx 7.5$ J/cm^2. The TEM_{00} ablation also shows faster growth with increasing fluence and less plateauing compared to the TEM_{40} mode. The measured data shows plateauing more consistent with the multi-

mode case than the single mode case. The plateauing is partially caused by melt re-flow into the crater and is exacerbated by the multi-mode structure of the fluence distribution. The severity of the melt re-flow effects (e.g. the ratio of volume flowing back into the crater to the total volume of the crater) scales inversely with crater size. Thus, the simulated crater depths plateau at lower fluences than the measured data due to the melt re-flow affecting smaller widths of the TEM_{40} lobes.

In order to compare the difference in craters formed in air versus vacuum, the temporal evolution of the crater needs to be assessed. Figure 46 shows the instantaneous evaporated density at time t and maximum crater depth as a function of time for different incident fluence values on Ti in air. The laser pulse is centered at $t = 100$ ps. Melt flow starts due to the recoil pressure from the evaporation process, but after evaporation is complete, the melt flows continues inertially, i.e. without the recoil pressure source term in the Navier-Stokes equation.

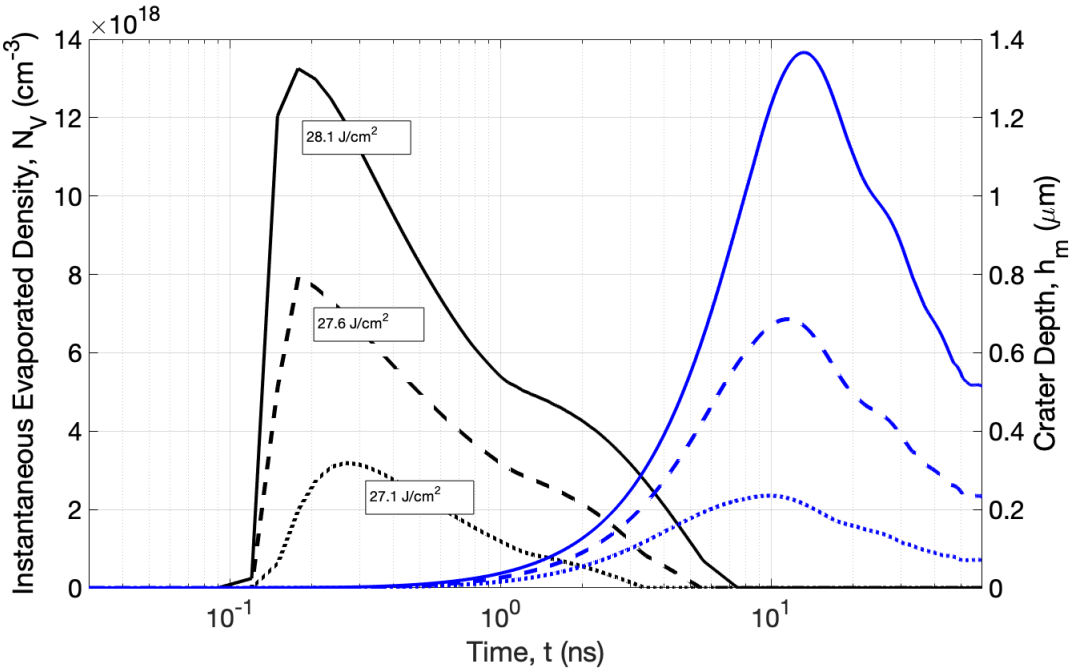

Figure 46. Instantaneous evaporated density (left axis, black lines) and crater depth (right axis, blue lines). $\lambda = 1064$ nm, $\tau_p = 28$ μs, $\omega_0 \approx 6.7$ μm, F : varied, Material: Ti, $P = 1$ atm, $T = 300$ K.

The plateauing of crater depth with fluence is partially due to melt flow back into the crater, which does not occur as much with a Gaussian TEM_{00} fluence distribution. The amount of re-flow is proportional to the material surface tension, with InSb having the lowest surface tension and the largest increase in crater volume with increasing fluence (see Figure 29).

The noticeable plateauing of hole depth cannot be due to plasma shielding alone, since the plasma initiation from the early ejection of electrons is expected to produce only weak absorption, if any at all[6]. Furthermore, the bulk of plasma shielding occurs from the plume of vaporized material, which does not form until several hundred picoseconds after the initial plasma initiation[6]. Under the current conditions, additional pulse energy causes a higher recoil pressure and more melt re-flow effects, whereas for longer pulse durations and shorter wavelengths, additional laser energy is converted primarily to plume kinetic energy[14]. Thus the multi-mode beam is much less efficient than the single mode TEM_{00} beam.

As previously mentioned, DEIVI does not include recondensation effects, so simulations in air and vacuum produce nearly identical craters. However, the recondensation, or backstreaming coefficient, can be caculated using the Knudsen layer jump conditions and including negative evaporation velocities, following Reference [76]. Using this approach, the recondensation coefficient for Al was found to be 18.4%. Another approach assuming a one-dimensional expansion into vacuum yields a recondensation coefficient of approximately 10%[77]. Thus, crater depths in air would be approximately 10-20% lower than in air.

The Knudsen layer jump conditions in DEIVI were modified to include a 20% reduction in evaporation across the layer, and the resulting crater evolution is shown in Figure 47. With recondensation, there is reduced evaporation as well as reduced crater depth. Physically, the plume is more confined to the surface at higher pressures, with the plume

stopping distance scaling as $(E/p)^{1/3}$, where E is the energy in the plume, and p is the background pressure[64]. Assuming equal energy in the plume at ambient air and vacuum (as previously discussed there is very little laser-plume coupling here), the stopping distance in air is approximately 1000 times shorter than in vacuum. Thus, more matter evaporated into the plume is expected to recondense to the surface. The peak instantaneous evaporation rate is 20% lower (as expected from modifying the jump conditions) and the final crater depth is only 3% lower. Within experimental uncertainty, the crater depths in vacuum are only slightly larger than those in air, and are not inconsistent with the simulated value.

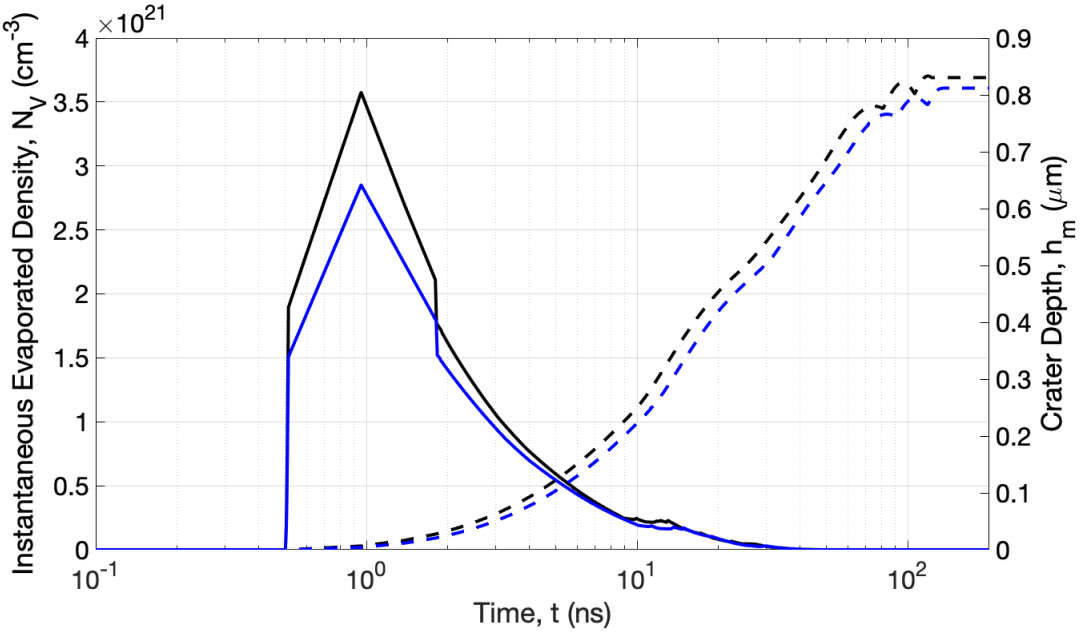

Figure 47. Instantaneous evaporated density (left axis, solid lines) and crater depth (right axis, dashed lines) with (blue lines) and without (black lines) recondensation effects. $\lambda = 1064$ nm, $\tau_p = 28$ μs, $\omega_0 \approx 6.7$ μm, $F = 22.1$ J/cm^2, Material: Ge, $P = 1$ atm, $T = 300$ K.

While the actual recondensation effects are time-dependent, this simple approximation implies that recondensation explains most of the difference between the measured craters on Ge in air and vacuum. Recondensation also explains why the volume ratio V_+/V_- is larger in air than in vacuum: more mass left the wafer entirely via evaporation

in vacuum than in air, and V_+ consisted of recondensed mass in addition to displaced melt. The recondensation effects are expected to be similar for all materials since the volume ratio plateaued to a similar value at high fluences. The increase in efficiency going from ambient air to vacuum is primarily due to reduction in recondensation.

4.5 Conclusion

Low transverse order Gaussian beams at 1064 nm wavelength and 28 ps pulse duration were used to ablate Al, Si, Ti, Ge, and Insb in air, and Ge in vacuum. Crater depths and volumes, as well as volume of material above the surface were measured using a laser confocal microscope. Crater depths were found to plateau with increasing fluence on each material, and crater depths on Ge in vacuum were slightly higher than in air. Crater volume above and below the surface was found to increase linearly with fluence for all materials in air. In vacuum, the volume of material above the surface was less than in air, and increased at a lower rate with increasing fluence. The ratio of volume above the surface to volume below the surface was found to plateau for all materials to approximately 0.7 in air, and 0.4 for Ge in vacuum. The ablation efficiency, defined as atoms removed per incident photon was higher at low fluences, and was proportional to the material optical absorption coefficient. At high fluences, the ablation efficiency on each material was substantially lower, with a very slight dependence on material viscosity. Simulations using the Directed Energy Illumination Visualization tool showed that evaporation was the dominant mass removal mechanism at low fluences, whereas bulk melt flow out of the crater caused by the evaporation recoil pressure dominated at higher fluences. Plateauing of crater depth with fluence was caused by melt re-flow into the crater, which effects smaller crater widths more than larger ones, as evidenced by comparing multi-mode results to TEM_{00} simulations. Recondensation of evaporated material was identified as the main difference between craters formed in air versus vac-

uum, and the Knudsen layer jump conditions were modified to account for an estimated $\approx 20\%$ recondensation rate. The simulations showed a resulting reduction in recoil pressure, which drove less melt out of the crater. Higher resolution simulations and additional experimental data comparing different order modes are needed to further test these explanations.

5. Visible Aluminum Monoxide Emission During Long Pulse mid-Infrared Ablation of Aluminum in Air

The long pulse ablation of aluminum wafers in ambient air using an Er:YAG laser at 2.94 μm wavelength is presented. Visible emission spectra collected during ablation are assigned to the $B^2\Sigma^+ \rightarrow X^2\Sigma^+$ molecular electronic transition of aluminum monoxide (AlO). A rovibronic model including self-absorption within the plume is developed to determine the molecular temperature. A 60.2 μs pulse at a fluence of 249.92 $\pm$ 40 J/cm^2, a temperature of 2843 $\pm$ 32 K and 3013 $\pm$ 30 K was found with the linear and nonlinear models, respectively. A greybody background, with an emissivity of approximately 1.3×10^{-6} was observed, implying a low volume mixing fraction of particulates in the plume. A linear fit of the $\Delta v = -1$ sequence was developed to rapidly analyze hundreds of spectra taken as a background pressure was varied from 400 mbar to 1000 mbar. The AlO temperature is approximately independent of background pressure. Finally, comparisons to other laser ablation studies at shorter wavelengths and shorter pulse durations are made wherever possible.

5.1 Introduction

Pulsed and continuous wave (CW) laser ablation of aluminum has applications in a wide variety of fields, such as thin film deposition and laser sintering [24, 78]. Pulsed ablation of Al and Al_2O_3 targets in low pressure background gases generates plumes with strong shocks, and atomic emission from neutral and ionized aluminum[79]. For example, plume kinetic energies of 50 eV/atom and Mach > 40 arise from significant target shielding, limiting emission to atomic species[14]. For ablation at atmospheric pressures and significant delays of > 10 μs, AlO B-X emission is readily observed[11, 80, 81, 40]. The $\Delta v = 0, \pm 1, \pm 2, \pm 3$ sequences are observed at 450-550 nm and have been used to discern rovibrational product distributions and temperatures[82]. The molecular emis-

sion is favored for plume temperatures of 3000-6000 K[81]. This oxidation influences the atomic stoichiometry and complicates calibration for laser induced breakdown spectroscopy (LIBS) applications.

The oxidation of aluminum during pulsed laser ablation and various combustion applications may proceed via several mechanisms. The direct $Al + O_2 \rightarrow AlO + O$ reaction is nearly isoenergetic and produces ground state $AlO(X^2\Sigma^+)$ primarily in the lowest vibrational levels. Electronically excited $AlO(B^2\Sigma^+)$ may be produced by three body recombination via the AlO_3 complex[83], excitation of AlO(X) by high speed impact in the shock front[11, 80], electron impact [10], or from absorption of thermal photons in an optically thick plume. The visible B-X emission observed during pulsed laser ablation depends on target material, plume confinement, and background gas composition[81].

Most aluminum pulsed ablation studies for near ambient atmospheric pressures have been conducted with Q-switched (~10 ns) Nd:YAG laser sources, yielding peak irradiances of 1-100 GW/cm^2[11, 80, 81, 40]. At these shorter wavelengths the laser radiation couples strongly with the material and the plume, which reduces the impact of thermal effects. AlO(B) is first observed in the shock front, and increases dramatically in the interior of the plume after long delays of 10-50 μs[10]. Most studies examine spatially and temporally averaged spectra, with a few studies dedicated to the temporal evolution of the rovibrational AlO(B,v'J') distributions[11, 10]. While the AlO emission relative to atomic emission grows dramatically with time, the rovibrational temperatures evolve in a narrow band from 4500-3000 K, and somewhat lower than the atomic and ionic temperatures of nearly 7000 K[10]. Rotational and vibrational temperatures can differ for some conditions[80].

The formation mechanism for AlO(B) is not well-established. Varenne et al discussed whether excited AlO is formed via a long-lived intermediary species Al-O-O_2 or via ground state AlO colliding with atomic and molecular oxygen, with the former

mechanism implying that AlO(B) should be produced with its population in a Boltzmann distribution[83]. Kasatani et al measured the AlO(B) population distribution at low pressure during 532 nm laser ablation, and found the vibrational states to be Boltzmann distributed, but also found that $T_{vib} \neq T_{rot}$[80]. Bai et al showed that the most intense molecular AlO emissions observed during 1064 nm laser ablation of aluminum did not correspond to the highest molecular temperature[11]. Further, they measured two distinct, linear cooling regimes including a steep initial drop-off in temperature, followed by a slower cooling period[11]. Both regimes were found to be dependent on laser pulse energy[11]. Hartig et al showed that the atomic aluminum emissions during 10 ns Nd:YAG ablation at 1064 nm were background pressure dependent, and the duration of atomic emissions decreased with increasing pressure[81]. Lam et al showed that during 355 nm 5 ns ablation of aluminum that atomic aluminum is formed first near the surface, with AlO forming on the outside layer of the plume[10]. As the plume expands, AlO emissions can come from deeper inside the plume[10]. Moreover, at longer delay times (e.g. around 100 μs) AlO emissions dominate atomic aluminum emissions[10]. Giacomo and Hermann developed a two-temperature plasma model to describe the emissions of AlO from laser-induced fluorescence (LIF) measurements. As the background pressure increases, the AlO density increases due to higher confinement near the front of the plume[84].

There appear to be no prior studies of Al pulsed ablation at lower irradiance and longer wavelengths. Recent advances in mid-infrared laser sources enable new tools for ablation studies. In the present study, the visible AlO(B-X) emission resulting from ablation in air at λ = 2.94μm with 60 μs pulses and peak irradiance of nearly 10 MW/cm^2 is examined. These less energetic, more thermal ablation conditions provide a means to explore laser wavelength-dependent aspects of the ablation process and plume evolution.

5.2 Apparatus

The experimental apparatus is shown in Figure 48.

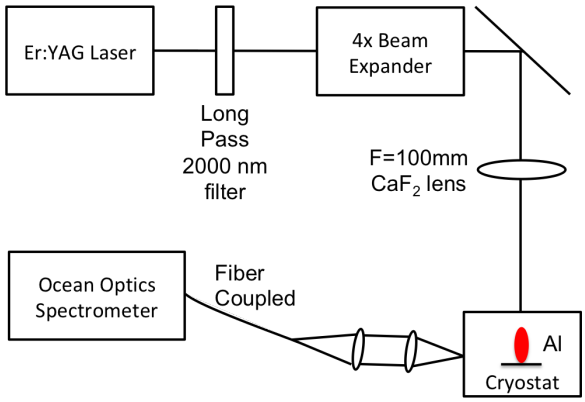

Figure 48. Experimental setup for observing optical emission spectra during pulsed laser ablation of Al.

A Megawatt Lasers flashlamp-pumped Er:YAG laser operating at 2.94 μm with variable pulse duration between 50 and 400 μs, up to 1000 mJ pulse energy, and a 10 Hz repetition rate is sent through a long-pass 2 μm filter to remove residual flashlamp radiation. The beam was characterized along the direction of propagation, z, with a minimum spot radius (at 1/e point) of $\omega_0 = 0.307 \pm 0.023$ mm and $M^2 = 17$, as shown in Figure 49.

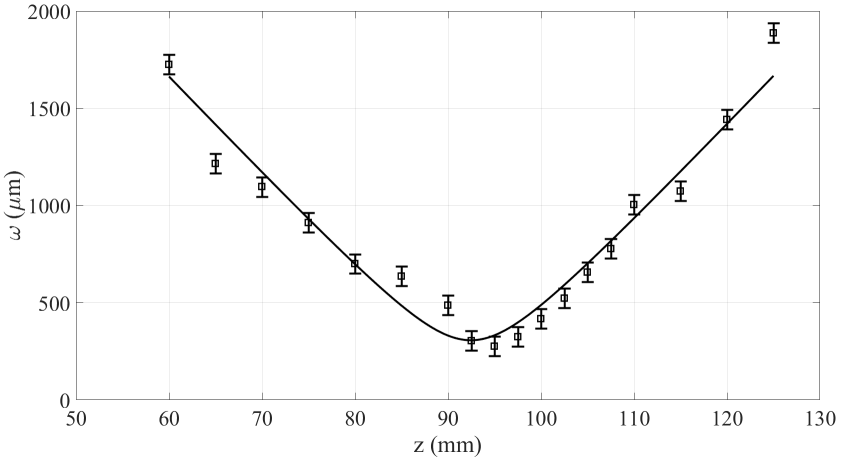

Figure 49. Spatial laser beam beam profile with minimum spot radius $\omega_0 = 0.307 \pm 0.023$ mm and $M^2 = 17$

Pulse-to-pulse energy variation was typically less than 1%. The 100 μs nominal pulse duration was used for this experiment. The temporal pulse profile was measured to have a full-width half-max (FWHM) of 60.2 μs and is shown in Figure 50.

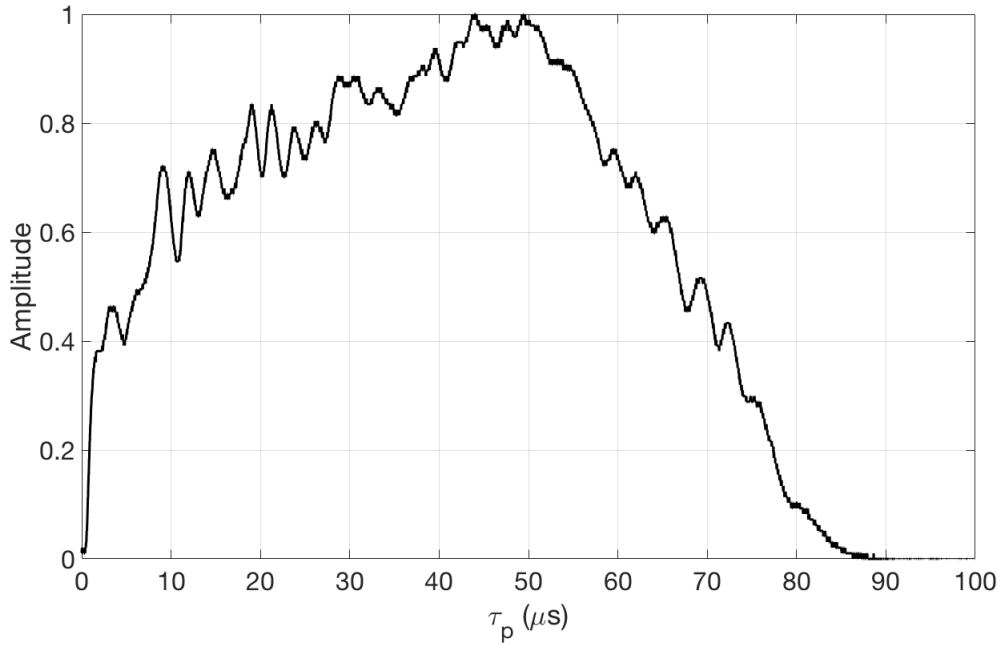

Figure 50. Temporal laser pulse profile with 60.2 μs FWHM

With the spot size and pulse duration characterized, the maximum fluence was found to be 249.9 J/cm^2 and peak irradiance was 4.15 MW/cm^2. The visible emission spectra are collected with an f/4 lens and fiber-coupled to an Ocean Optics HR4000 Custom spectrometer with optimized detectivity for 350-800 nm and a 0.2 nm slightly asymmetric Lorentzian lineshape, which is shown in Figure 51. The relative spectral response was calibrated using a 1500 K blackbody source. With 100 ms integration time and five pulse average, the signal-to-noise ratio was > 125.

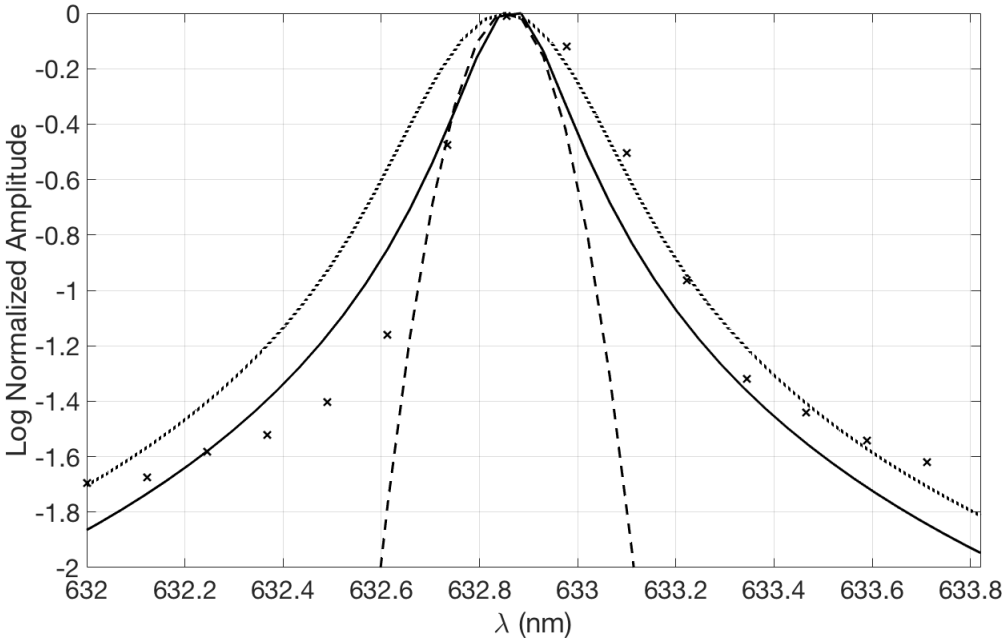

Figure 51. Spectrometer lineshape: measured (x), Lorentzian (-), Gaussian (- -), and Voigt (.-)

The target wafers were 99.9% pure aluminum from MTI Corp with single side polished. The samples were stored in a desiccator, to reduce but not eliminate surface oxidation. The nominal aluminum density of 2.7 g/cm^3, thermal diffusivity of 0.86 cm^2/s and heat of vaporization of 9.46 MJ/kg are assumed. These tests were performed in ambient air at a nominal temperature of 300 K and pressures from 0.4-1 bar. The cryostat was mounted on a translation stage and was moved after 10-100 shots to avoid cratering. Damage sites on the wafer were measured with a Zygo ZeGage white light interferometer with 0.1 nm depth resolution.

5.3 Results

A typical crater formed on the aluminum wafer by 10 coincident pulses is shown in Figure 52.

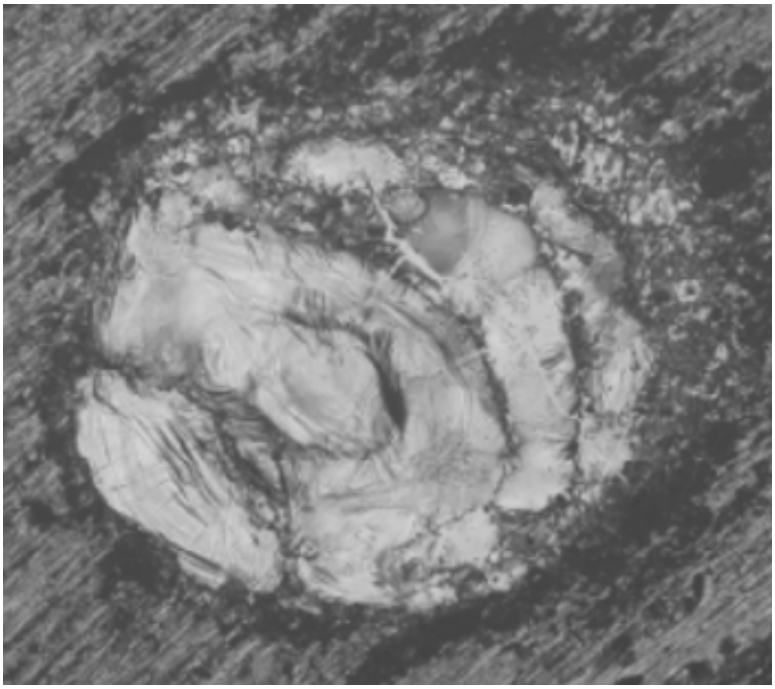

Figure 52. Crater formed from 10 pulses. $\lambda = 2947$ nm, $\tau_p = 60.23$ μs, $\omega_0 \approx 307$ μm, $F = 250$ J/cm^2, Material: Al, $P = 1$ atm, $T = 300$ K.

The crater shows signs of re-solidified melt and essentially no splatter. By one dimensional energy balance, the ablation threshold of aluminum can be calculated as $I_{th} = \rho L_v \sqrt{\kappa/\tau_p}$, where ρ is the density, L_v is the latent heat of vaporization, κ is the thermal diffusivity, and τ_p is the pulse duration. This definition of the ablation threshold leads to $I_{th} = 2.43 \times 10^6$ W/cm^2. With a pulse energy of 740 mJ, a pulse duration of 60.2 μs, and a spot size of 307 μm, the irradiance on the aluminum wafer was 4.15×10^6 W/cm^2, which is only slightly above the ablation threshold. Thus, significant mass removal for a single laser pulse was not expected. Further, it is expected that excess energy likely produced initial plume speed, rather than more atoms removed [14]. The thermal diffusion length can be taken as $L = \sqrt{\kappa t} \approx 72\mu$m using the pulse duration of the laser. With the beam diameter being approximately 614 μm, this implies that there is not much transverse heat conduction. With a 800 μm square field of view, Figure 52 shows that melt features are relatively confined to an area approximately equal to the

beam area. The interferometric image is shown in Figure 53, and the depth profile of the crater is shown in Figure 54.

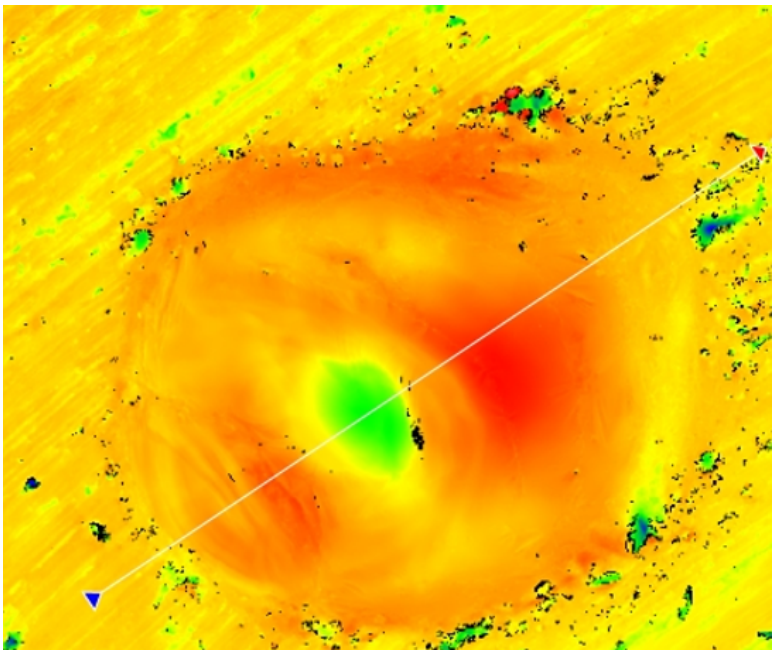

Figure 53. White light interferometric image of ablation crater from 10 shots. $\lambda = 2947$ nm, $\tau_p = 60.23$ μs, $\omega_0 \approx 307$ μm, $F = 250$ J/cm^2, Material: Al, $P = 1$ atm, $T = 300$ K.

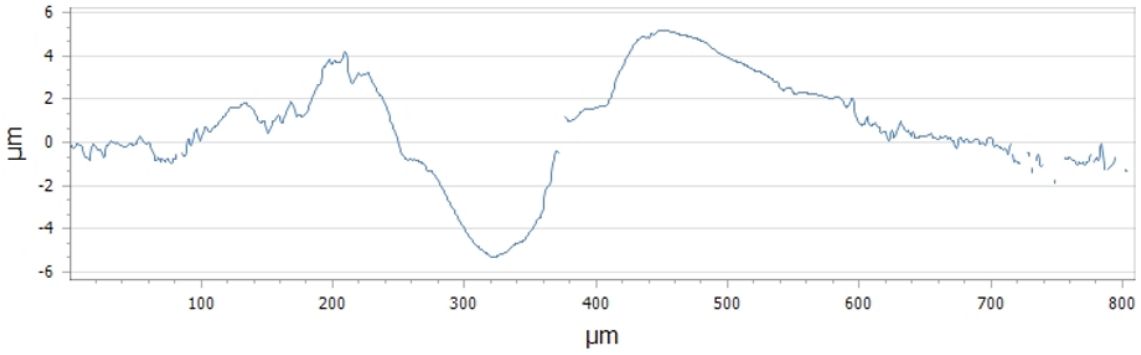

Figure 54. Depth profile of crater from 10 shots. $\lambda = 2947$ nm, $\tau_p = 60.23$ μs, $\omega_0 \approx 307$ μm, $F = 250$ J/cm^2, Material: Al, $P = 1$ atm, $T = 300$ K.

The maximum hole depth after 10 pulses is 5.3 μm. Volume measurements above and below the wafer surface indicate that negligible mass was removed, with $\Delta m \ll 1$ ng.

The low mass removal in these long pulse, long wavelength ablations limits the observed spectral intensity and restricts observations to spatially and temporally averaged results. More discussion on the mass removal will be provided in a subsequent paper.

Figure 55 shows the observed spectra of AlO during ablation of aluminum. The fluence was 249.92 ± 40 J/cm^2 and the pulse duration was 60.2 μs. The integration time was the entire interpulse period.

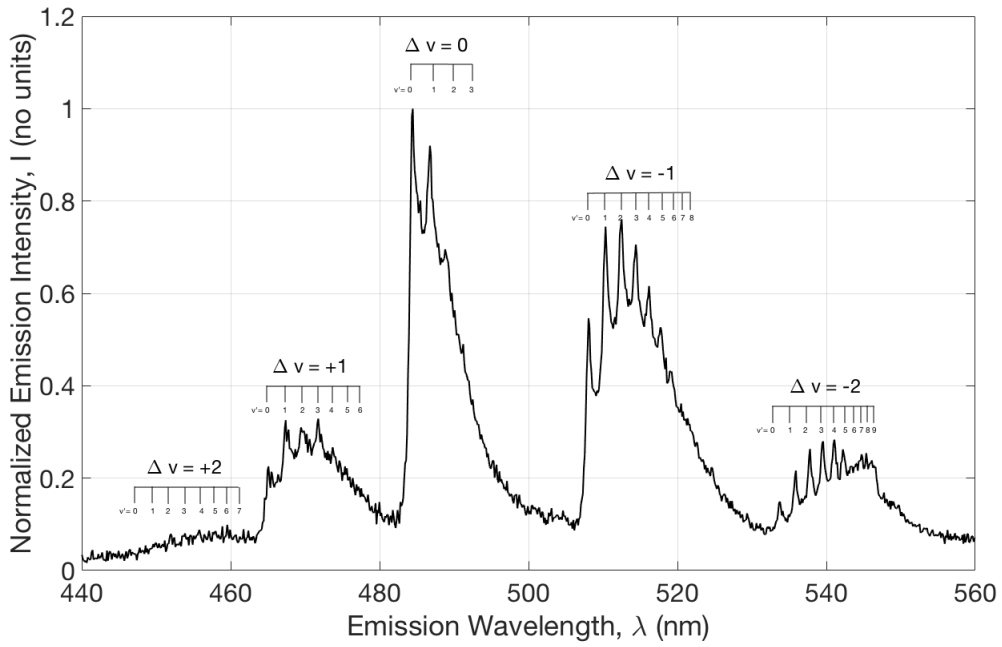

Figure 55. Spatially and temporally integrated emission spectrum from λ = 2947 nm, τ_p = 60.23 μs, $\omega_0 \approx 307$ μm, $F = 250$ J/cm^2, Material: Al, $P = 1$ atm, $T = 300$ K.

The AlO B and X potential energy curves are almost vertical, yielding a set of $\Delta v = \pm 2, \pm 1, 0$ sequences. Emission from a wide range of excited vibrational levels, $v' = 0 - 9$ indicated significantly elevated vibrational temperatures. There is a slight blackbody background approximately 30 times larger than the dark signal of the spectrometer. The atomic $^2S_{1/2} \rightarrow ^2P_{1/2}$ and $^2S_{1/2} \rightarrow ^2P_{3/2}$ lines at 394.4 nm and 396.152 nm, respectively, were occasionally visible. However, when present, the neutral atomic Al lines were weaker than the molecular AlO signal by a factor of ten, and had a signal-to-noise

ratio <2. Thus, there is not enough atomic spectra data to discuss in the current effort. In comparison, UV pulsed ablation at low pressure is dominated by atomic and ion emission[14].

Comparing Figure 55 to aluminum flame signals in Reference [82], it can be seen that the present spectra has less blackbody background, and a higher signal-to-noise ratio. Before fitting the current data to a line-by-line radiative transfer model, it cannot be deduced if the temperature is different. However, the difference in background and signal-to-noise implies less particulates and blackbody emission in the current data when compared to aluminum combustion spectra.

The spatial and temporal averaging done by the large viewing volume of the collection lens and the long integration time of the spectrometer greatly complicate the assignment and interpretation of a temperature. The spectra in Figure 55 contains the entire evolution of the plume, which is a highly nonlinear process.

5.4 Spectral Simulations and Plume Temperatures

In order to interpret the observed spectra, a line-by-line radiative transfer model of the AlO $B^2\Sigma^+ \rightarrow X^2\Sigma^+$ rovibrational emission was developed. The spectroscopic constants for AlO are provided in Table 7[85]. All values have units of wavenumbers, except the equilibrium separation, r_e, which is in Angstroms.

Table 7. AlO spectroscopic constants

Diatomic Constant	$X^2\Sigma$	$B^2\Sigma$
T_e	0	20688.95
ω_e	979.23	870.05
$\omega_e\chi_e$	6.97	3.52
B_e	0.6413	0.6040
α_e	0.0058	0.0044
D_e	1.08×10^{-6}	1.16×10^{-6}
β_e	0	0
r_e	1.6179	1.6670

It is worth noting that more accurate spectroscopic data exists (c.f. References [86, 87]), but the choice was made to formulate the model in terms of Morse potential parameters for simplicity and runtime considerations. The wavelength of the transition is found using the diatomic constants in the usual way[88]. The equilibrium nuclear separation for both states is within 0.05 Angstroms of each other, suggesting the existence of numerous vertical transitions between the two potential energy curves. The Franck-Condon factors used for transitions between $v' = 0-15$ and $v'' = 0-18$ are from Reference [89].

The electronic spin splitting of the P and R branches associated with a $^2\Sigma \rightarrow {}^2\Sigma$ transition is neglected since the rotational spacing (approximately 1.2 cm^{-1} or 0.03 nm) is much finer than the instrument linewidth of 0.2 nm[88]. The Hönl-London factors for the R and P branches are $S^R_{J'J''} = J'$ and $S^P_{J'J''} = J' + 1$, respectively [90]. There is no Q branch for a $\Delta\Lambda = 0$ transition, where Λ is the molecular orbital angular momentum[88]. Although at 3000 K, $J_{max} \approx 41$, rotational levels up to $J = 300$ are included, following Reference [91].

For an optically thin gas, the relative (e.g. normalized by viewing volume and solid angle) spectrally integrated intensity of emissions from a specific upper state (v', J') to a lower state (v'', J'') can be modeled as

$$I(v', J') = D(\lambda) A_{21} \frac{hc}{\lambda} N(v', J') q_{v'v''} S^{\Delta J}_{J'J''} \tag{14}$$

where $D(\lambda)$ is the detector spectral response, A_{21} is the Einstein A coefficient for the transition, h is Planck's constant, λ is the transition wavelength, $N(v', J')$ is the population in the state (v', J') at equal vibrational and rotational temperature $T_{vib} = T_{rot} = T$, $q_{v'v''}$ is the Franck-Condon Factor for the vibrational transition $v' \rightarrow v''$ and $S^{\Delta J}_{J'J''}$ is the Hönl-London Factor for the rotational transition$J' \rightarrow J''$. The radiative lifetime of the upper state is assumed to constant for all vibrational levels, and is taken to be 92.4 ns,

which is the lifetime of the $v = 0$ state of AlO(B) [87]. Reference [87] shows the radiative lifetime increasing slowly with vibrational state ($\sim 4\%$ from $v = 0$ to $v = 2$), which likely causes the model proposed here to overestimate the population in higher lying states, especially in the $\Delta v = -1$ and $\Delta v = -2$ sequences. This in turn could lead to an underestimation of the temperature obtained by fitting the model to the data, but a sensitivity analysis of the vibrational dependence of the radiative lifetime in the model indicates that this difference is approximately 2%.

The observed AlO signal in Figure 55 shows slight self-absorption due to the ground state AlO concentration in the plume. Although the spectra is obviously not very optically thick, any deviation from Equation 14 can affect the temperature from the fit. For an optically thick gas in local thermodynamic equilibrium (LTE) with no other light sources, the emitted intensity is

$$I_\lambda = D(\lambda) B_\lambda(T_{bb})[1 - \exp(-\alpha'_\lambda l)] \tag{15}$$

where $B_\lambda(T_{bb})$ is the Planck distribution at the blackbody temperature T_{bb}, and $\alpha'_\lambda = \alpha_\lambda[1 - \exp(-hc/\lambda kT)]$ is the absorption coefficient corrected for stimulated emission, and l is the path length[91, 92]. The path length was assumed to be 1 mm for the model. For low absorption, Equation 15 reduces to the linear intensity in Equation 14 by expanding the exponential to first order and using Kirchoff's equation $\alpha'_\lambda = E_\lambda / B_\lambda$ [92]. The absorption coefficient $\alpha_\lambda = N\sigma$ can be written as

$$\alpha_\lambda = N(v'', J'') \left[\left(\frac{g'}{g''} \right) \frac{\lambda^2}{4} A_{21} q_{v'v''} S^{\Delta J}_{J'J''} \Delta\lambda \right] \tag{16}$$

where σ is the average absorption cross section at line center, and $\Delta\lambda$ is the Lorentzian instrument linewidth. Finally, an overall greybody background can be added to Equation 15 to account for thermal background effects in the spectra. The measured signal

then becomes

$$I_\lambda = D(\lambda)\left\{B_\lambda(T_{bb})[1-\exp(-\alpha'_\lambda l)]+\epsilon_p B_\lambda(T_p)\right\} \tag{17}$$

where ϵ_p is the relative (after normalizing the spectra and accounting for detector response) emissivity compared to $\epsilon = \alpha$, where α is the molecular absorbance as a function of rotational and vibrational temperature defined in Equation 16, and T_p is the blackbody background temperature of the particulates in the plume, and is potentially difference from the temperature in Equation 15. Thus, the relative emissivity of the blackbody background is an indication of the particulate content of the plume: low ϵ_p indicating low particulate content. The optically thick relative intensity of AlO emissions assuming $T_{rot} = T_{vib} = T_{bb} = 3000$ K is compared to the simulated linear intensity with the same temperature in Figure 56. Both simulated spectra are shown without a greybody background.

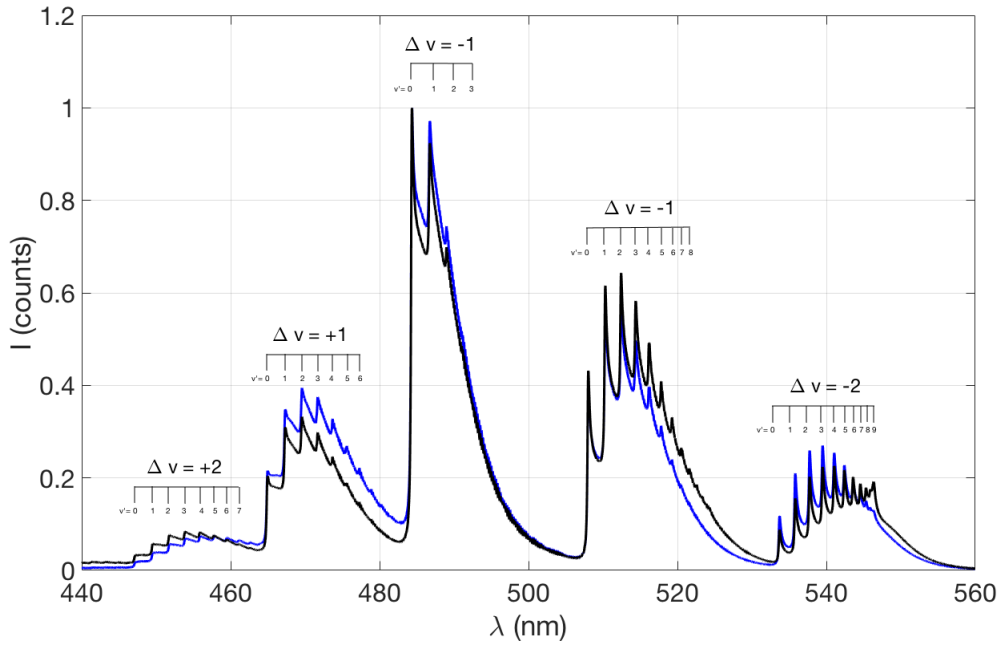

Figure 56. Comparison of optically thin (blue) and optically thick (black) AlO B-X emission spectra with $T_{vib} = T_{rot} = T_{bb} = 3000$ K.

Since both spectra are normalized to their respective maximum value at the $(0,0)-(0,0)$ transition, the degree of trapping can be examined by looking at the other sequences. The $\Delta v = +2$ band head is approximately 83% higher for the optically thin case than for the optically thick; the $\Delta v = +1$ band is almost 6% higher; the $\Delta v = -2$ band is almost 34% higher. The effect of trapping from the $\Delta v = -1$ sequence is less than 1% and thus either an optically thick or thin fit could be used on only the $\Delta v = -1$ sequence. Both the optically thin and thick simulations were fit to the observed data in Figure 55 as shown in Figure 57.

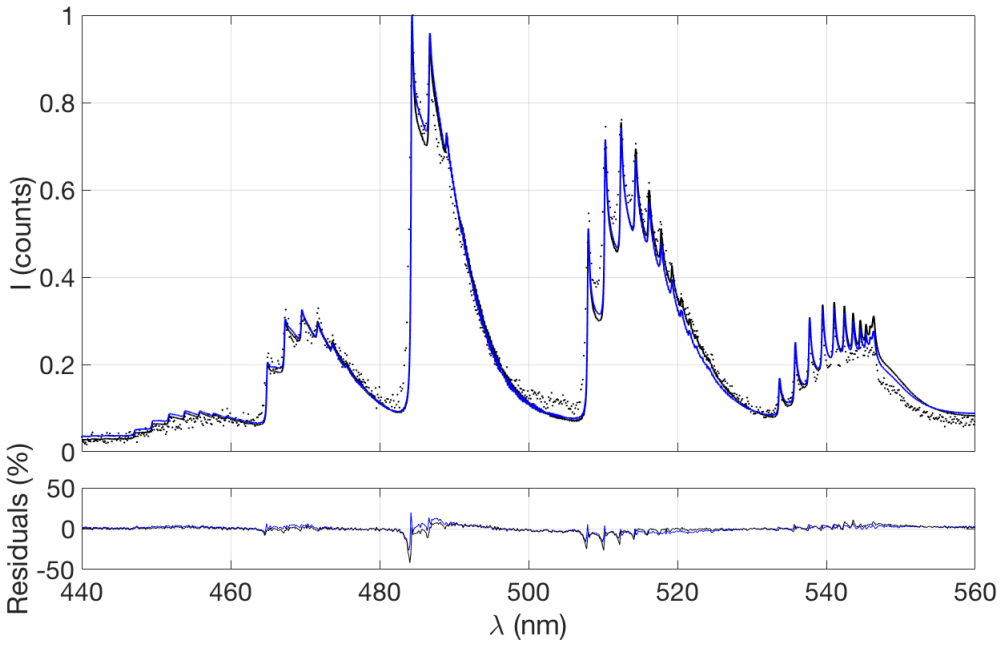

Figure 57. Linear fit (blue) and optically thick fit (black) to the observed spectra (dots) of Figure 55.

The linear fit with rotational and vibrational temperatures constrained to a common value yields a molecular temperature of 2843 ± 32 K, while the optically thick fit provides a temperature of 3013 ± 30 K. Although there is significant structure to the residuals, the fit quality is comparable to work from Bai[11], Parigger[40], and Lam[10]. The optical thickness likely varies with both position in the plume and time delay, so the residu-

als in the current study likely reflect nonlinear intensity averaging resulting from the single-layer, time-independent model. The molecular temperature for both fits are similar, and are higher than the vaporization temperature of aluminum, which is taken to be 2743 K. The blackbody background intensity is $\epsilon_p = 0.088 \pm 0.0068$ and 0.0792 ± 0.0082 for the linear and optically fit, respectively. Using the relative (e.g. normalized by population in the ground state) absorption coefficient of the AlO B-X $(0,0) - (0,0)$ transition, $\alpha = N(v'', J'')\sigma_{\text{abs}} \approx 1.6 \times 10^{-5} = \epsilon_{\text{AlO}}$, the absolute emissivity of the particualtes can be found as $\epsilon = \epsilon_p \epsilon_{\text{AlO}} = 1.3 \times 10^{-6}$. So, the relative greybody emissivity from the optically thick and thin fits are essentially the volume fraction of the particulates. Both fits provide a low particulate volume mixing fraction, implying that the plume is still mostly AlO gas, and not particulates. The agreement of both fits also confirms that the spectra is mostly thin and there is very little optical thickness. In aluminum flame studies, the particulate content is usually much higher, resulting in a larger background signal and higher emissivity[93]. In order to improve model fidelity, an evolving multi-layer radiative transfer model that is benchmarked to detailed plume imaging data would be required, in addition to the more accurate line positions and strengths from Reference [87].

The main difference between the fits is the temperature of the blackbody background. For the linear fit, the blackbody background temperature is found to be 2811 ± 236 K, while the blackbody temperature for the optically thick case is found to be 2447 ± 69 K. In the linear fit, the blackbody background temperature is increased to account for the "tilt" in the spectra, whereas in the optically thick fit, self-absorption produces this effect. When fitting the entire observed AlO spectra from 440 to 560 nm, the optically thick fit is used. However, following the approach of Bai et al, a linear fit can be used on the $\Delta v = -1$ vibrational sequence[11]. It can be seen in Figure 57 that both fits (and residuals) are comparable for the $\Delta v = -1$ sequence.

Using the linear fit of the $\Delta v = -1$ vibrational sequence, the AlO temperature as a function of the oxygen background pressure in the cryostat for laser pulse energy of 740 mJ and pulse duration of 60.2 μs is shown in Figure 58.

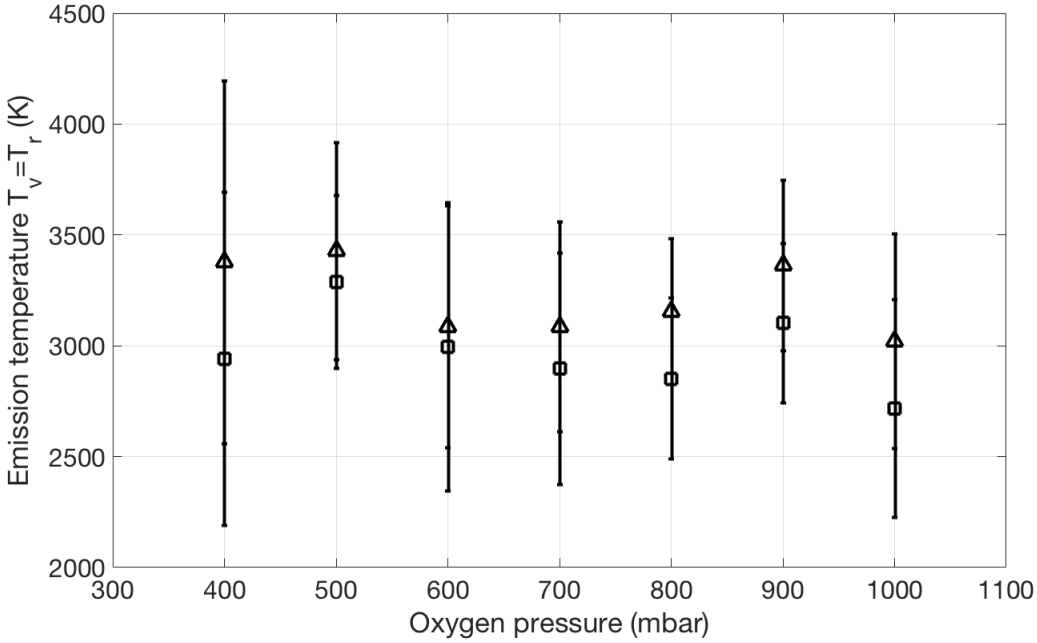

Figure 58. Temperature from (□) optically thick fit of entire observed AlO B-X spectra and (△) optically thin fit of $\Delta v = -1$ sequence. $\lambda = 2947$ nm, $\tau_p = 60.23$ μs, $\omega_0 \approx 307$ μm, $F = 250$ J/cm^2, Material: Al, P : varied, $T = 300$ K.

The spatially and temporally averaged temperature from the rovibrational model is approximately independent of background pressure, at least between 400 and 1000 mbar. The optically thick fit of the entire observed spectra and the optically thin fit of just the $\Delta v = -1$ sequence provided nearly the same temperature, within the standard uncertainty.

5.5 Discussion

The observed spectra are spatially and temporally averaged, which complicates the interpretation of a temperature. In almost all cases, the plume of ejected material dur-

ing laser ablation is spatially inhomogeneous and evolves in time. The non-linear spatial and temporal averaging in this experiment prohibits drawing direct conclusions about the AlO chemical kinetics and time evolution of the plume, but semi-quantitative comparisons to other ablation studies can still be made. It will be assumed that the spectrum is dominated by the brightest portion of the plume during the time interval of highest AlO(B) concentration.

Bai showed that the maximum AlO signal did not coincide with the highest AlO temperature[11]. Thus, lack of temporal resolution prohibits the conclusion that the temperature from the rovibrational fit is the maximum temperature. Lam et al measured the molecular temperature of AlO after 5 ns, 355 nm laser ablation of iron and titanium-doped Al_2O_3 in air to be 4550 ± 455 K at a delay of 40 μs [10]. The temperature decreased slowly to approximately 3000 K at 80 μs delay. The average temperature over all delay times was found to be 3515 ± 352 K [10].

Bai et al measured the time-evolution of the molecular temperature of AlO after 1064 nm laser ablation of aluminum in air with a pulse duration of 4 ns. The AlO temperature was found to be over 6000 K at a delay of 5 μs, and decreased linearly to just over 4000 K 35 μs later for 10 mJ pulse energy[11]. Dors et al used a frequency-quadrupled Nd:YAG laser with 266 nm wavelength and 6 ns pulse duration to ablate Al_2O_3 in air. At a delay of 20 μs, the molecular temperature of AlO was found to be approximately 3400 K[40]. The current results for much lower irradiance, longer wavelength, and longer pulse duration, yield quite similar results to the prior highly energetic studies, which seems to suggest that ablation mechanism and early plume thermalization is not critical to the observed rovibrational distribution of AlO(B). The modest temperature currently observed appears consistent with the asymptotic (steady-state) values reported by Lam, and the observation that AlO is favored with plume temperatures at 3000-6000K[81]. The observed temperature is slightly higher than is seen in combustion studies.

The pulse duration in the present study is much longer than the pulse durations of the aforementioned experiments. Most laser ablation experiments use pulse durations less than 10 ns, whereas the current study used 60 μs. For the same pulse energy, this results in an intensity that is approximately three orders of magnitude lower. The pulse energies used here are much higher (740 mJ versus 10 mJ, for example), but the resulting intensity is much lower (approximately 4 MW/cm^2 versus 4 GW/cm^2). Thus, mass removed per laser shot is much lower, and thus less AlO is likely present in the plume. Since the pulse duration is so long, the additional pulse energy mostly goes into heat conduction in the material, not into the plume. So, more laser pulse energy is not expected to lead to higher AlO temperatures in the plume.

The chemical kinetics of the plume can also be used to help compare the observed spectra to other studies. In order to describe the evolution of the concentration of AlO(B,v'), numerous assumptions are required. The goal is to be able to describe the temperature and AlO(B) concentration with a small set of reaction mechanisms. Thus, it is assumed that the plume is thermalized, the shock front is degraded, and ion content is largely neutralized. At the high pressures in the current study, this likely occurs in less than a microsecond [14]; this onset delay is neglected, and only the decay in the AlO(B) rovibrational temperature is tracked. The production of AlO from neutral Al and background oxygen gas proceeds only after the plume has cooled to approximately 6000 K [11, 81]. Collisional electronic quenching by N_2 and O_2 of the AlO(B) state is included, since quenching rates in ambient air are on the order of $k_q[M] \approx 1 \times 10^8\ s^{-1}$, which is an order of magnitude higher than the spotaneous emission rate. The probability of electronic-translational (E-T) energy transfer can be approximated as $P \sim \log(\Delta E)$, where ΔE is the energy difference between the initial and final states [94]. In this case, the large energy difference between the AlO(B) and AlO(X) states implies a small probability of E-T energy transfer occurring.

The only source of AlO is assumed to be atomic aluminum colliding with molecular oxygen. However, other oxides of the form Al_nO_m can dissociate to form AlO[83]. The model also ignores the actual ablation process, i.e. all species are instantly in a homogeneous mixture at $t = 0$, and there is no mass flow into or out of the interaction volume. As such, there is also no heat transfer from the material to the surrounding air, which is assumed to be at constant pressure, and shielding of the laser pulse is not considered either. Finally, no internal structure of the species is assumed, and the plume is assumed to be in LTE. The following reaction mechanisms are proposed:

$$\mathrm{Al} + \mathrm{O_2} \xrightarrow{k_1} \mathrm{AlO(X)} + \mathrm{O} \tag{18}$$

$$\mathrm{AlO(X)} + \mathrm{M} \xrightarrow{k_2} \mathrm{AlO(B)} + \mathrm{M} \tag{19}$$

$$\mathrm{AlO(X)} + \mathrm{O} \xrightarrow{k_3} \mathrm{Al} + \mathrm{O_2} \tag{20}$$

$$\mathrm{O} + \mathrm{O} \xrightarrow{k_4} \mathrm{O_2} \tag{21}$$

$$\mathrm{AlO(B)} \xrightarrow{A_{21}} \mathrm{AlO(X)} + \gamma \tag{22}$$

$$\mathrm{AlO(B)} + \mathrm{O_2} \xrightarrow{k_{q,\mathrm{O_2}}} \mathrm{AlO(X)} + \mathrm{O_2} \tag{23}$$

$$\mathrm{AlO(B)} + \mathrm{N_2} \xrightarrow{k_{q,\mathrm{N_2}}} \mathrm{AlO(X)} + \mathrm{N_2} \tag{24}$$

The high speed collision between the AlO(X) plume and the background gas, where M = O_2 or N_2, can produce the electronic excitation. One might imagine particulate combustion as a source of AlO(B), but the low volume mixing fraction suggests otherwise, and thus that processes is excluded from this analysis. The collisional excitation rate of AlO(X) by M is assumed to have an activation energy of 247 kJ/mol, which is equal to the difference between the AlO($X, v = 0, J = 0$) and the AlO($B, v = 0, J = 0$) states. The rates for the various mechanisms can be written in Arrhenius form

$$k(T) = A\left(\frac{T}{298\text{K}}\right)^{n} \exp\left(\frac{-E_a}{RT}\right) \tag{25}$$

where E_a has units kJ$\cdot$ mol^{-1} and $R = 8.31 \times 10^{-3}$ kJ$\cdot$ mol$^{-1}\cdot$ K^{-1}. The pre-exponential factor for the collisional excitation of AlO(X) is estimated to be a typical bi-molecular collision rate. The conclusions of the model are insensitive to the specific value of this rate. The Arrhenius parameters for the rate coefficients are provided in Table 8.

Table 8. AlO Kinetics Rate Coefficients

	A	n	E_a	T	Source
k_1	3.32×10^{-11}	-	-	$300-2000$	[95]
k_2	1×10^{-10}	-	247	-	-
k_3	1.93×10^{-11}	-0.5	9.98	$300-2000$	[95]
k_4	9.26×10^{-34}	-1	-	$300-5000$	[95]
k_{q,O_2}	21×10^{-12}	-	-	300	[96]
k_{q,N_2}	20×10^{-12}	-	-	300	[96]

Assuming an exponentially decaying temperature that has been seen following nanosecond NIR ablation of aluminum in air (see Reference [39]), qualitative features of the plume emissions can be deduced from the simple kinetic description provided. From Table 8 it is clear that formation of AlO is favored at temperatures seen late in the plume evolution under typical LIBS conditions. Bauer, et al showed that most of the laser energy during UV ablation goes into kinetic energy of plume (via inverse Bremsstrahlung absorption) rather an internal excitation of the emitting species [5]. A more energetic plume would take longer to thermalize, and thus more atomic and ionic emissions would occur and AlO emissions would appear later. However, the plume here is expected to be less ionized, due to photoionization being much less significant in the mid-infrared. The degree of ionization also decreases rapidly; Lam et al showed that electron number

density decreased two orders of magnitude from 10^{18} cm^{-3} to 10^{16} cm^{-3} in just the first 3 μs after the laser pulse, so less laser-plume coupling is also expected[10]. Thus, the spatially and temporally averaged plume emissions in the current study are dominated by AlO because of this quick thermalization of the plume, which is likely due to reduced laser-plume coupling compared to shorter wavelengths. The fact that the AlO temperature deduced in the current study is similar to other studies with higher irradiance and shorter wavelengths suggests that the long-term plume thermalization does not depend strongly on early plasma effects and laser-plasma interaction. Additional experiments in the mid-infrared with shorter pulse durations are planned to further investigate these effects.

5.6 Conclusion

Long-pulse mid-infrared ablation of aluminum wafers in air produced visible emissions that were identified as the $B^2\Sigma^+ \rightarrow X^2\Sigma^+$ transition of AlO. A linear rovibrational model and a non-linear radiative transfer model were developed to characterize the observed spectra. Molecular temperatures of 2843 ± 32 K and 3013 ± 30 K were obtained for with the linear and nonlinear models, respectively. The spectra were collected over the entire interpulse period of the laser and with a large viewing volume, so these temperatures represent the spatially and temporally averaged AlO temperature. The greybody background emissivity of approximately 1.3×10^{-6} was found. Such a low emissivity suggests a low volume mixing fraction of particulates in the plume. A linear fit of just the $\Delta v = -1$ sequence was used to find the temperature as a function of background pressure, which was varied from 400 to 1000 mbar. The AlO temperature was found to be approximately independent of background pressure over that range. The lack of atomic and ionic emission in the plume suggests that the plume thermalizes quickly and little of the mid-infrared laser energy is coupled into the plasma. The present results at low

irradiance, long pulse duration, and long wavelength are strikingly similar to the more energetic studies, suggesting that the long-term thermalization of the plume becomes largely independent of the ablation process and laser-plume interaction.

6. Spectroscopy of Titanium Monoxide for Characterization of Laser Ablation

Ablation of titanium wafers in air is accomplished with 60-300 μs pulsed, 2.94 μm laser radiation. Titanium monoxide spectra are measured in the wavelength range of 500 nm to 750 nm, and molecular signatures include bands of the $C^3\Delta \rightarrow X^3\Delta$ α, $B^3\Pi \rightarrow X^3\Delta$ γ', and $A^3\Phi \rightarrow X^3\Delta$ γ transitions. The blackbody background signal was found to have a temperature between 2350 K and 2600 K from 1 to 1000 mTorr background pressure. With background pressures $P = 200-1000$ mTorr the total spectrally integrated emission intensity scaled as $P^{1/3}$. The spatially and temporally averaged spectra appear to be in qualitative agreement with previous temporally resolved studies that employed shorter wavelengths and shorter pulse durations than utilized in this work. Simulations in DEIVI show that peak temperature and pressure in the plume are not sufficient to create significant atomic and ionic emissions seen in such other studies. A peak temperature of approximately 4000 K is inline with molecular temperatures at long time delays as measured by Parigger and Giacomo. A simple chemical kinetics model, using the temperature and evaporated Ti volume from DEIVI predicts temporal behavior of the total TiO emission intensity in ambient air that matches the measured signal relatively well.

6.1 Introduction

Titanium monoxide (TiO) emissions have long been of interest in astronomy [97, 98, 99, 100, 101], and recently been studied in numerous laser-induced breakdown spectroscopy (LIBS) experiments [9, 41, 102]. Computed line strengths were utilized to fit experimental TiO γ' emission spectra [9] and discern a temperature of 3600 ± 700 K and 4200 ± 800 K at delays of 52 μs and 72 μs, respectively, after ablation in air using a Q-switched Nd:YAG laser with 1064 nm wavelength and 13 ns pulse duration. Using the same experimental setup [41], fitting of recorded $\Delta v = -1$ sequence data of the γ

band yields a temperature of approximately 5000 K at time delays of 1-2 μs, and a reduced temperature of approximately 2500 K at a time delay of 50 μs. However, the fitted temperature depends on background contributions. In that same study, application of spectroscopic fitting routines to published TiO emission spectra [102] indicates a temperature of 2170 $\pm$ 60 K.

The present study investigates TiO emissions during long-pulse mid-infrared ablation of titanium wafers in air. Spatial and temporal averaging due to long spectrometer integration times and large viewing volumes cause the measured signal to be dominated by the most intense phase of the plume. For mid-infrared ablation of aluminum in air, it was found that the plume was dominated by AlO emission rather than atomic or ionic emissions due to the rapid thermalization of the plume under weak laser-plume coupling at longer wavelengths [103]. It is unknown if the titanium ablation plume will undergo a similar rapid thermalization, since it has a much more complex molecular structure than AlO with numerous excitation and relaxation channels [104]. The purpose of this study is to perform laser ablation of titanium under the same conditions as [103] and semi-quantitatively compare the observed plume emissions to that study as well as previous works at shorter wavelengths and pulse durations.

6.2 Apparatus

A flashlamp-pumped Er:YAG laser device (Megawatt Lasers) operating at 2.94 μm with variable pulse duration between 50 and 400 μs, up to 1 J pulse energy, and a 10 Hz repetition rate is transmitted through a long-pass 2 μm filter to remove residual flashlamp radiation. The beam propagation was characterized with a minimum spot radius of 0.307 $\pm$ 0.02 mm and an M-squared-value of M^2 = 17. Two waveforms with a full-width, half-max (FWHM) of 60 and 320 μs have a steeper leading edge than a Gaussian temporal pulse, and include significant ringing. With the spot size and pulse duration

characterized, the maximum fluence was found to be 250 J/cm^2 corresponding to a peak irradiance of 4.1 MW/cm^2 with the 60 μs pulse, and 0.78 MW/cm^2 with the 300 μs pulse, when focused into a cryostat containing ambient laboratory air. Pulse-to-pulse energy jitter was typically less than 1%. The visible emission spectra are collected with an f/4 lens (perpendicular to the laser path and parallel to the wafer surface) and fiber-coupled to a spectrometer (Ocean Optics HR4000 Custom) that shows an optimized detection range of 350-800 nm. A function generator was used to synchronize the laser and spectrometer for gated measurements. The instrument lineshape of the spectrometer is a slightly asymmetric Lorentzian shape with a 0.2-nm full-width at half-maximum. The relative spectral response was calibrated using a 1500 K blackbody source. With a single 10 μs integration time, the signal-to-noise ratio was 5. With a 100 ms integration time and five-pulse average, the signal-to-noise ratio exceeded 125. The experimental setup is shown in Figure 59.

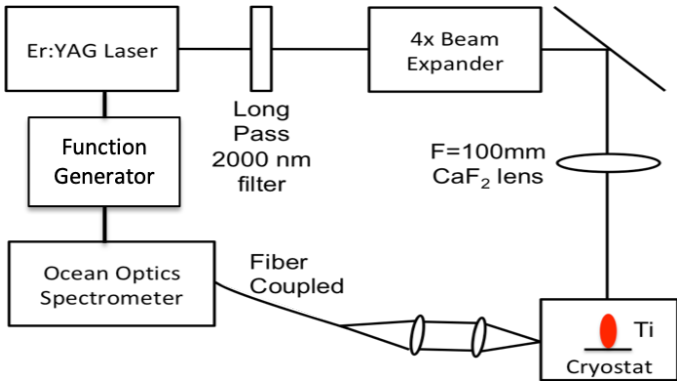

Figure 59. Experimental setup for observing TiO emissions during mid-IR ablation of Ti in air.

The wafers were 99.9% pure titanium (MTI Corporation), single-side polished. The samples were stored in a desiccator, to reduce but not eliminate surface oxidation. The nominal titanium density of 4.5 g/cm^3, thermal diffusivity of 0.072 cm^2/s and heat of vaporization of 8.88 MJ/kg are assumed. The cryostat was mounted on a translation stage and was moved every 2-3 shots to avoid the formation of craters. Damage sites on

the wafer were measured with a white light interferometer (Zygo ZeGage) with 0.1-nm depth resolution.

6.3 Results

6.3.1 Craters

Figures 60(a-g) depict the effects of laser ablation of Ti wafers in ambient laboratory air, and Figure 61 shows the corresponding crater depth profiles. In the experiments, single pulse effects show no splatter and very little melt flow. The occurrence of raised center is likely due to the thermocapillary effect [1]. The features for two shots at 10 Hz repetition rate are similar to the single shot case, but more pronounced in depth and height of the protrusion relative to the crater depth. Using energy balance, the vaporization threshold of titanium can be calculated as $I_v = \rho L_v \sqrt{\kappa / t}$, and the melt threshold is $I_m = \rho L_m \sqrt{\kappa / t}$, where ρ is the density, L_v and L_m are the latent heats of vaporization and melt, respectively, κ is the thermal diffusivity, and t is the pulse duration. This definition yields a peak irradiance vaporization threshold of 1.42 MW/cm^2, which is about twice the irradiance of the 300 μs pulse and approximately one third the irradiance of the 60 μs pulse. Both pulse durations provide an irradiance above the melt threshold, which is found to be 0.07 MW/cm^2. The thermal diffusion length can be taken as $L \approx \sqrt{\kappa t} \approx 20$ μm using the pulse duration of the laser. For a beam diameter of 614 μm, there is not much transverse heat conduction. Figure 60(a) shows that melt features are relatively confined to an area approximately equal to the beam area. The inter pulse period is 100 ms, while the time for heat to conduct a distance equal to the spot diameter is on the order of 1 ms, but the dramatic increase in crater depth from two to three shots indicates the pulse are not completely thermally isolated.

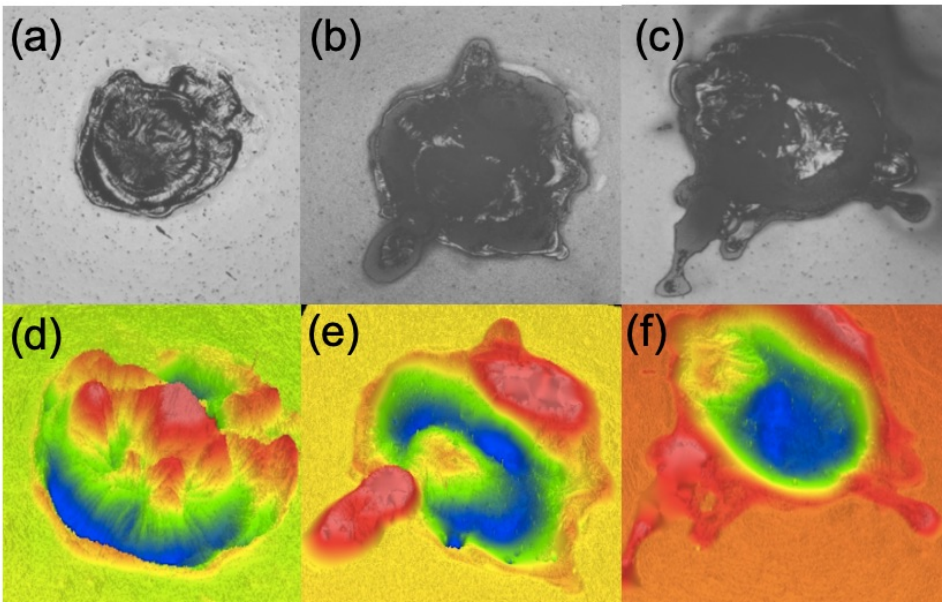

Figure 60. Optical microscopy images of single, double, and triple pulse laser damage (a-c), and white light interferometric images (d-f). $\lambda = 2947$ nm, $\tau_p = 60.23$ μs, $\omega_0 \approx 307$ μm, $F = 250$ J/cm^2, Material: Ti, $P = 760$ Torr, $T = 300$ K.

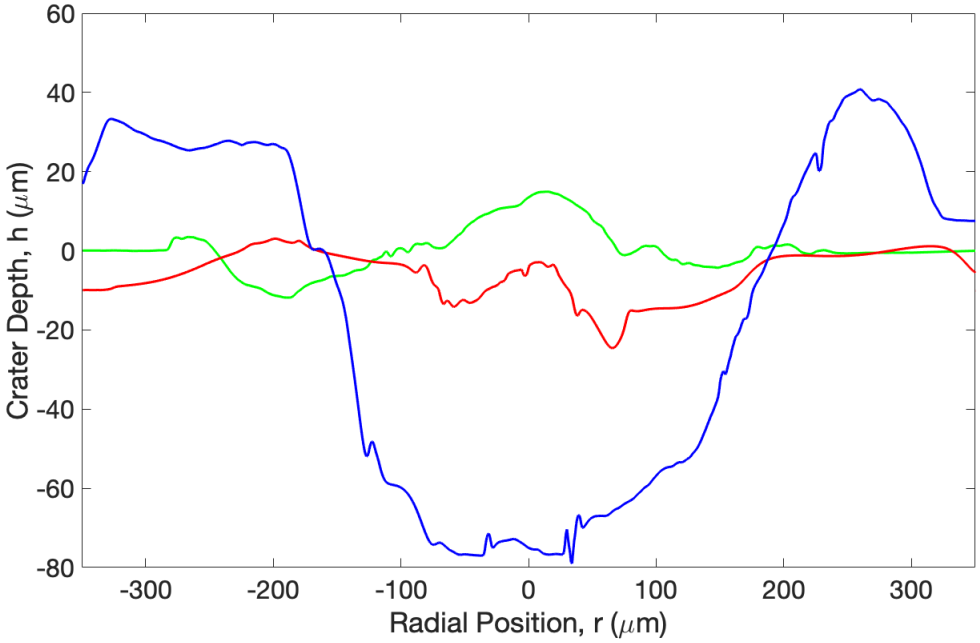

Figure 61. Crater depth profiles. $\lambda = 2947$ nm, $\tau_p = 60.23$ μs, $\omega_0 \approx 307$ μm, $F = 250$ J/cm^2, Material: Ti, $P = 760$ Torr, $T = 300$ K.

6.3.2 Optical Emission Spectra

Figure 62 displays spatially and temporally averaged emission spectra from various TiO bands [105] resulting from 60 μs mid-infrared laser ablation of Ti wafers in air. $\Delta v = \pm 1$ and 0 sequences are observed for the $C^3\Delta \rightarrow X^3\Delta$, $B^3\Pi \rightarrow X^3\Delta$, and $A^3\Phi \rightarrow X^3\Delta$ transitions.

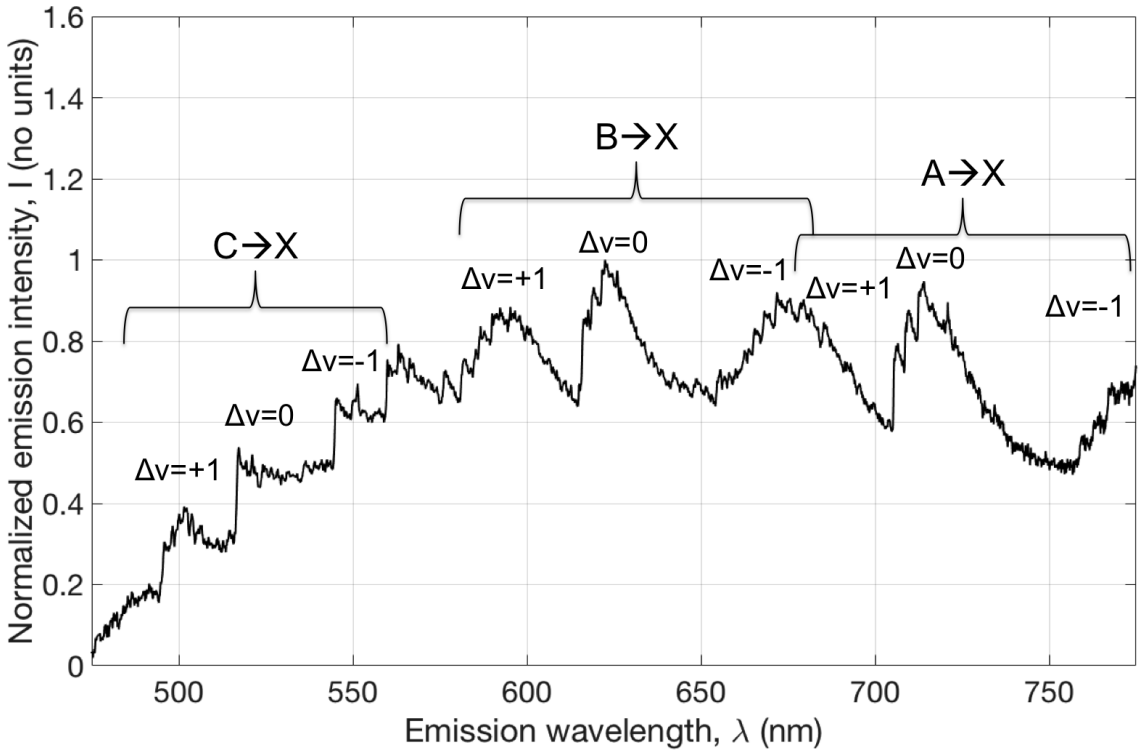

Figure 62. Spatially and temporally averaged TiO emission spectra after laser ablation with $\lambda = 2947$ nm, $\tau_p = 60.23$ μs, $\omega_0 \approx 307$ μm, $F = 250$ J/cm^2, Material: Ti, $P = 760$ Torr, $T = 300$ K.

The spatial and temporal averaging complicates the interpretation of a temperature, since the temperature evolves non-linearly over the lifespan of the plume. At the shortest integration time of 10 μs, which is long compared to atomic and molecular interactions but still shorter than the lifetime of the plume, no atomic or ionic emissions were observed at any delay time relative to the laser pulse. Thus, Figure 62 shows that the plume is likely dominated by TiO molecular emissions rather than atomic or ionic emis-

sions. Figure 63 shows the integrated intensity of the TiO emissions with background pressures between 1 and 1000 mTorr.

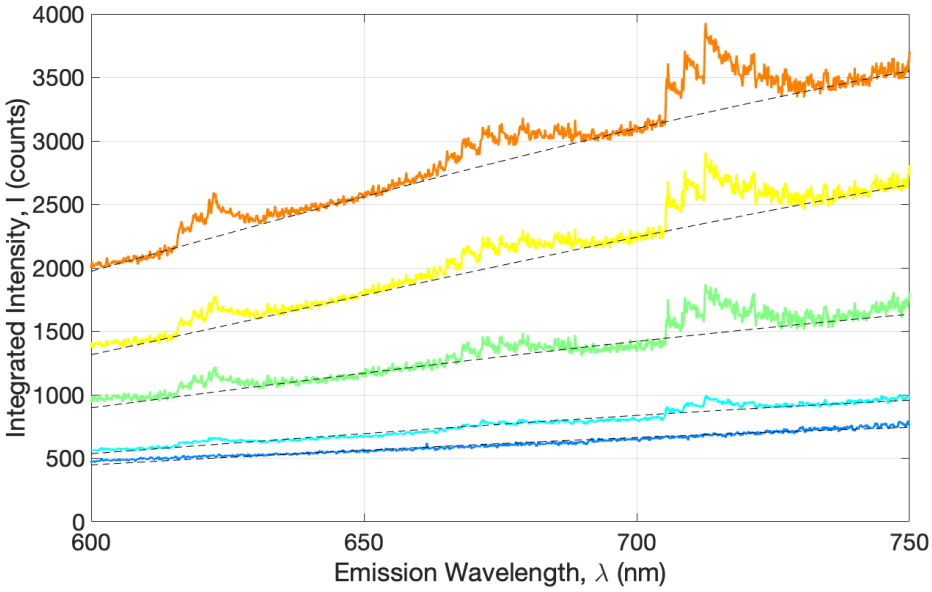

Figure 63. Temporally integrated intensity of TiO emissions. $\lambda = 2947$ nm, $\tau_p = 60.23$ μs, $\omega_0 \approx 307$ μm, $F = 250$ J/cm^2, Material: Ti, $P = 1$ (-), 100 (-), 200 (-), 500 (-), and 1000 mTorr (-), $T = 300$ K. Dashed black lines are blackbody background signal.

The dashed black lines represent a blackbody background with emissivity $\epsilon = A/\lambda$, where A is the amplitude in counts, and λ is the wavelength. Typical background signals in diatomic emission spectroscopy can be fit to linear, quadratic, or blackbody functional forms (see Reference [82]), and combustion studies often assume a blackbody with emissivity of $1/\lambda$ or $1/\lambda^2$ (see Reference [93]). The latter approach was chosen here due to the higher background signal, more reminiscent of aluminum combustion studies[82]. The amplitude of the background, A, scaled from 800 to 3900 as pressure increased from 1 to 1000 mTorr. The background amplitude can have significant impacts on the fitted temperature. For example, in Reference [41], changing the linear background for a normalized TiO emission spectra from 0.2 to 0.3 lowered the fit temperature (i.e. the molecular temperature of TiO, not the blackbody background temper-

ature, but in thermodynamic equilibrium, the two temperatures would be equal) from approximately 5300 K to 3400 K. The background temperature in the current study was between 2350 and 2600 K, with normalized background amplitudes between 0.21 and 1, but care should be taken when interpreting this quantitatively. While there is insight to be gained from the background fit, the current application is to simply background-subtract the spectra in order to compare spectrally integrated emissions at different background pressures. At a background pressure of 1 mTorr, there are no detected TiO emissions. The $\Delta v = 0$ sequence of the TiO $A \rightarrow X$ band is barely discernible at a background pressure of 100 mTorr. By 200 mTorr, the $\Delta v = -1, 0$ sequences of the $B \rightarrow X$ band and the $\Delta v = +1$ sequence of the A band are seen. As pressure is increased to 1000 mTorr, the amplitude of each sequence increases, as does the overall background signal. The spectrally integrated intensity (including background) of TiO emissions as a function of pressure is shown in Figure 64. The signal-to-noise ratio is less than 3 at 1 and 100 mTorr, but after 200 mTorr, the integrated intensity scales as $P^{1/3}$.

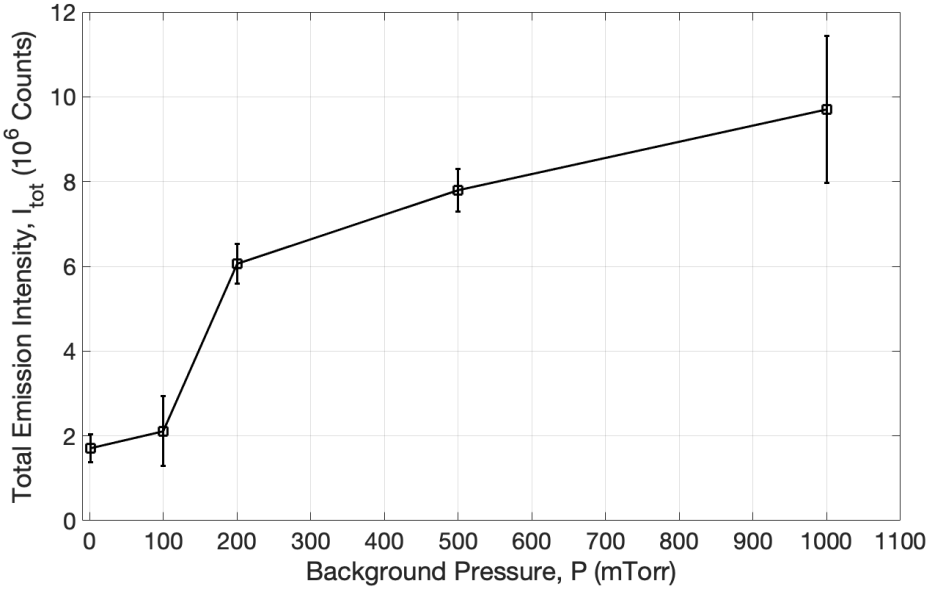

Figure 64. Spectrally integrated intensity of TiO emissions. $\lambda = 2947$ nm, $\tau_p = 60.23$ μs, $\omega_0 \approx 307$ μm, $F = 250$ J/cm^2, Material: Ti, P : varied, $T = 300$ K.

Figure 65 shows the integrated intensities of the three sequences after correcting for the blackbody background.

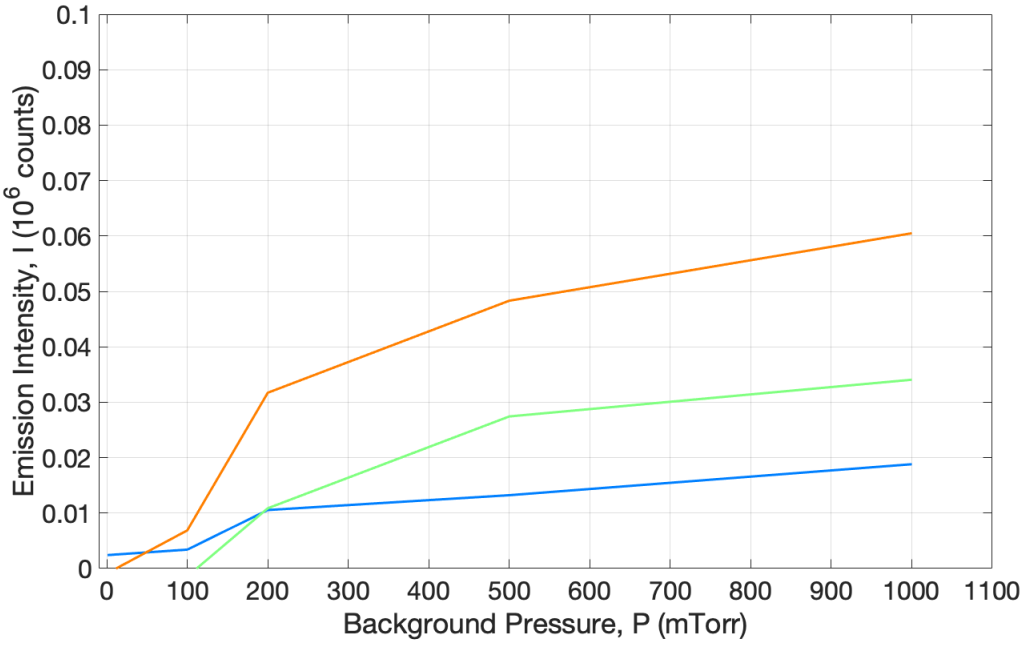

Figure 65. Integrated emission intensity of background-corrected TiO $B \rightarrow X\ \Delta v = 0$ (-), $B \rightarrow X\ \Delta v = -1$ and $A \rightarrow X\ \Delta v = +1$ (-), and $A \rightarrow X\ \Delta v = 0$ (-) emissions. $\lambda = 2947$ nm, $\tau_p = 60.23$ μs, $\omega_0 \approx 307$ μm, $F = 250$ J/cm^2, Material: Ti, P : varied, $T = 300$ K.

The $\Delta v = 0$ sequence of the $A \rightarrow X$ transition accounts for most of the TiO signal, and the total intensity of all the sequences is only 10% of the total integrated intensity (shown in Figure 64) at 1000 mTorr. Thus, from 1 to 1000 mTorr, nearly 90% of the signal intensity increase comes from the blackbody background, rather than from TiO emissions.

For pseudo-time resolved measurements, the 300 μs pulse was used. Even though the irradiance is below the calculated vaporization threshold, mass removal did occur, and the longer pulse duration provides more time steps with the minimum gate of 10 μs. Figure 66 shows the gated spectra measurements with a 50 μs gate and 10 μs gate inset. The laser pulse temporal profile is shown in red.

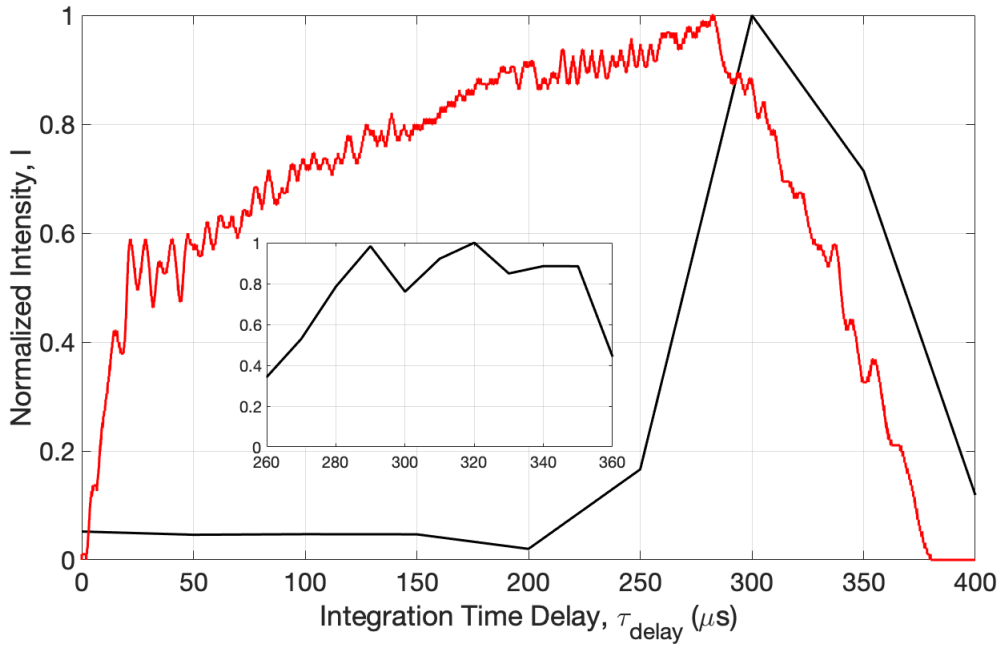

Figure 66. Integrated intensity of TiO emissions with 50 μs gate, and 10 μs gate (inset). λ = 2947 nm, τ_p = 300 μs, $\omega_0 \approx 307$ μm, F = 250 J/cm^2, Material: Ti, P = 760 Torr, T = 300 K. Laser pulse temporal profile in red.

TiO emissions begin around 200 μs delay from the start of the laser pulse and grow to a maximum at 300 μs with the 50 μs gate. The inset showing the measurements using a 10 μs gate indicates that the intensity oscillates several times between 280 and 350 μs. While this is not truly time-resolved spectroscopy, the gating is still short compared to the lifetime of the plume, and thus provides information on its overall evolution.

6.4 Kinetics Model and DEIVI Simulations

To understand the relative intensities of the TiO emissions, their dependence on background pressure, and their temporal evolution, a spatial and temporal chemical kinetics model is needed. As a starting point, spatial evolution of the plume will be deferred until later, and a time-dependent kinetics model will be constructed first. TiO is much more complicated than AlO, but the process can be simplified greatly by only

tracking the population in the electronic level rather than in each rovibrational state. The key mechanisms are shown in Equations 26-30.

$$\mathrm{Ti} + \mathrm{O_2} \xrightarrow{k_1} \mathrm{TiO(X)} + \mathrm{O} \tag{26}$$

$$\mathrm{O} + \mathrm{O} \xrightarrow{k_2} \mathrm{O_2} \tag{27}$$

$$\mathrm{TiO(i)} + \mathrm{M} \xrightarrow{k_{ij}} \mathrm{TiO(j)} + \mathrm{M} \tag{28}$$

$$\mathrm{TiO(j)} + \mathrm{M} \xrightarrow{k_{ji}} \mathrm{TiO(i)} + \mathrm{M} \tag{29}$$

$$\mathrm{TiO} + \mathrm{M} \xrightarrow{k_{dM}} \mathrm{Ti} + \mathrm{O} \tag{30}$$

Equation 26 is the chemical mechanism for the formation of molecular TiO($X^3\Delta$) ground state from the oxidation of the atomic Ti(a^3F) ground state. Equation 27 is the recombination of molecular oxygen, which does not play a significant role here due to the relatively small amount of Ti removed from the surface. This mechanism would be more important if sufficient atomic Ti was in the plume such that the molecular oxygen was appreciably depleted. Equation 28 represents the excitation of TiO from electronic state i to j (e.g. from A to B) via collisions with species M, where M is any atomic or molecular species in the plume. Even though the spectra in Figures 63-66 only include the A→X and B→X transitions, the TiO($C^3\Delta$) will be included as well. Equation 29 is the collisional quenching of excited TiO. Equation 30 is the collisional dissociation of TiO.

The rates in Equations 26-30 are given in Table 9, and assumed to follow an Arrhenius form,

$$k(T) = A\left(\frac{T}{298}\right)^n \exp\left(\frac{E_a}{RT}\right) \tag{31}$$

where the units of A depend on the order of the reaction, and are cm^3/s for bi-molecular reactions, E_a is in kJ/mol, and T is in Kelvin. The values for k_1 are from Reference [106], and k_2 is from Reference [95]. Even though that expression for k_1 is only valid up to 600 K, it does not effect the relative concentrations of the A, B, and C states. The pre-

exponential term for the collisional excitation and quenching rates are assumed to be typical bi-molecular rates.

Table 9. TiO Kinetics Rate Coefficients

	A	n	E_a	T
k_1	1.69×10^{-10}	0	11.6	$300-600$
k_2	9.26×10^{-34}	-1	-	$300-5000$
$k_{XA} = k_{AX}$	2.5×10^{-12}	0	168	-
$k_{XB} = k_{BX}$	2.5×10^{-12}	0	194	-
$k_{XC} = k_{CX}$	2.5×10^{-12}	0	231	-
$k_{AB} = k_{BA}$	2.5×10^{-12}	0	26	-
$k_{AC} = k_{CA}$	2.5×10^{-12}	0	63	-
$k_{BC} = k_{CB}$	2.5×10^{-12}	0	37	-
k_d	1×10^{-12}	0	703	-

The initial conditions of the kinetics model are that at $t = 0$ the concentration of O_2 is that of ambient air and $T = 300K$. The concentration of Ti is calculated using the DEIVI software first described in Chapter 4. The measured spatial and temporal laser beam profile of the 300 μs waveform are used for the laser inputs, and nominal, temperature-independent material parameters from Table 3 in Chapter 3 are used. A grid spacing of 2 cells/μm is used, corresponding to 40 cells across the thermal diffusion length during the pulse, approximately 12 cells along the depth of the crater after one pulse, and approximately 7 cells across the mean free path of the plume at the vaporization temperature of titanium and three times ambient air pressure. The simulation duration is 500 μs. The temperature of the evaporated Ti is taken to be the plume temperature, and the concentration of O_2 and N_2 are assumed to be their respective partial pressures relative to the background pressure.

6.5 Discussion

Figure 67 shows the measured spectrally integrated emission signal (including background) and the simulated plume emission intensity as a function of time. The simulated plume temperature peaks at nearly 4000 K, and the plume pressure peaks at approximately 1.5 times ambient air pressure 290 μs after the laser pulse starts. The growth of the emission signal and even minor oscillations observed with the 10 μs gate are seen in the simulated plume. Changing the initial concentration of molecular oxygen does not affect the total simulated signal, which is likely because because the kinetics model is over simplified.

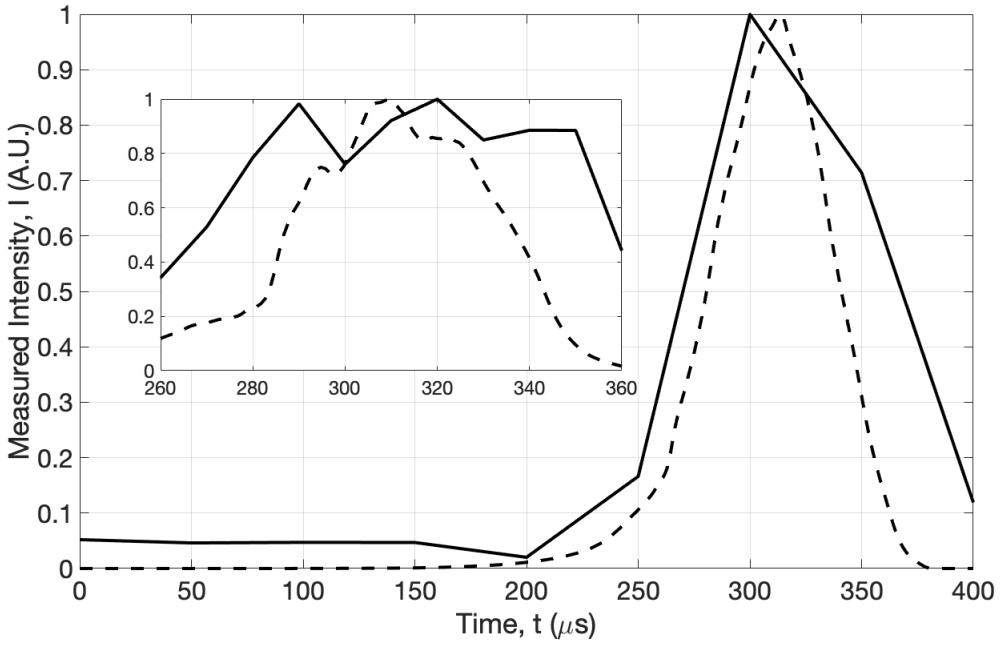

Figure 67. Measured (solid line) and simulated (dashed line) integrated TiO emission intensity with 50 μs gate and 10 μs gate (inset).

The 60-300 μs pulse duration in the current study lead to significantly lower peak irradiance than typically used for time-resolved experiments, and worse signal-to-noise and signal-to-background ratios[9, 41, 102]. However, the spatially and temporally av-

eraged spectra in this study appear qualitatively similar to temporally-resolved spectra recorded in other studies at time delays of several tens of μs after ablation with shorter wavelength and higher peak irradiance. Figure 68 shows the $\Delta v = 0$ sequence of the $B \rightarrow X$ transition spatially and temporally averaged in the current study compared to the 32 μs gated measurement at 75 μs delay from Reference [41] where a 1064 nm Nd:YAG laser with a pulse duration of 13 ns (peak irradiance of 10 TW/cm^2) was used. Parigger et al found the temperature from a fit of diatomic linestrengths to be between $3,434 \pm 714$ K and $5,322 \pm 1190$ K, depending on the background level used[41].

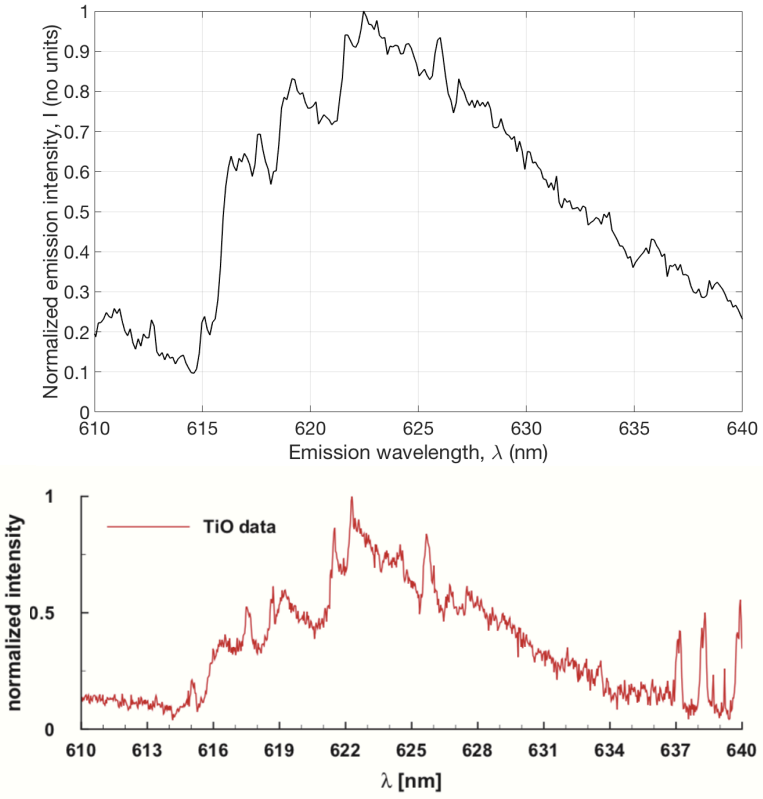

Figure 68. Temporally and spatially averaged emission from the $\Delta v = 0$ sequence of the $B \rightarrow X$ transition in the current study (top) and time-resolved emission at a delay of 75 μs from Parigger et al (bottom).

Figure 69 compares the $\Delta v = -1$ sequence of the $A \rightarrow X$ transition measured in the current study to Reference [102] which used a 532 nm, 7 ns laser with a peak irradiance

of 64 GW/cm^2. Giacomo et al measured the spectra at a delay of 32 μs and a gate width of 2 μs[102]. Parigger et al fit that data using the diatomic linestrength model and found the temperature to be 2170 ± 60 K[41]. The signal-to-noise ratio in the current study makes a direct comparison of this sequence particularly difficult, but that temperature is inline with the blackbody background temperature found in this study.

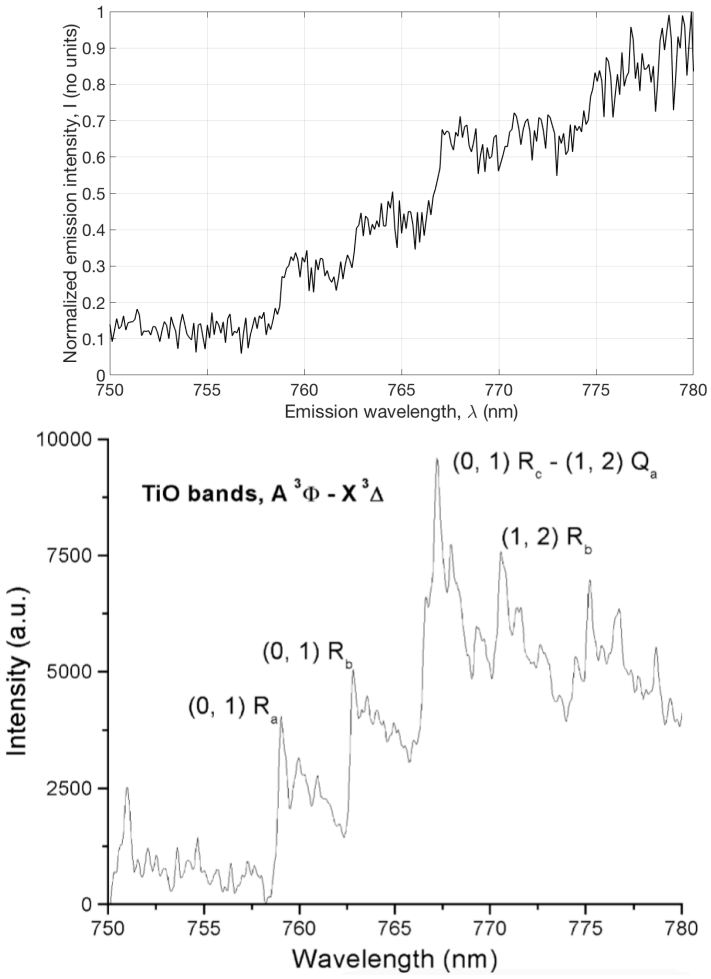

Figure 69. Temporally and spatially averaged emission from the $\Delta v = -1$ sequence of the $A \rightarrow X$ transition in the current study (top) and time-resolved emission at a delay of 32 μs from Giacomo et al (bottom).

Overall, the spectra in the current study, though spatially averaged and with limited time-resolved data, are remarkably similar to spectra observed at long delay times after ablation at much shorter pulse durations and higher irradiances. The simulations

in DEIVI show the peak pressure and temperature in the plume being too low to cause significant atomic or ionic emissions. The conditions at the end of the pulse in this study are more like the plume in nanosecond ablation studies after approximately 50 μs, i.e. after the plume has thermalized and the temperature becomes more conducive to molecule formation. In Chapter 5, it was surmised that the lack of atomic or ionic emissions could indicate that the shock front is comparatively weak and the plume thermalizes rapidly. Here the DEIVI simulations and time-resolved data confirm that is the case for Ti.

6.6 Conclusions

Long pulse mid-IR ablation of Ti in air and vacuum produces TiO emission consisting of the $A \rightarrow X$, $B \rightarrow X$, and $C \rightarrow X$ molecular electronic transitions and associated vibrational sequences. TiO emissions are first identifiable at 100 mTorr, and from 200 to 1000 mTorr, the total TiO signal (including background) increases as the cube root of pressure. The relativey large linewidth of the spectrometer and low signal-to-noise and signal-to-background ratios in the current study preclude detailed rovibrational analysis, and the fitting of simple diatomic model is incredibly more complex for TiO than for AlO. However, the spectra observed in this study are remarkably similar to those seen at long time delays after traditional ablation conditions (> GW/cm^2 peak irradiance, nanosecond pulse duration, ≤ 1064 nm wavelength). Simulations in DEIVI show that peak temperature and pressure in the plume are not sufficient to create significant atomic and ionic emissions seen in such other studies. A peak temperature of approximately 4000 K is inline with molecular temperatures at long time delays as measured by Parigger and Giacomo. A simple chemical kinetics model, using the temperature and evaporated Ti volume from DEIVI predicts temporal behavior of the total TiO emission intensity that matches the measured signal relatively well. However, the pressure-

dependence of the total integrated emission intensity is not captured by the simple kinetics model, which is an area for future development.

7. Conclusions

7.1 Conclusions

Pulsed laser ablation has been studied with the aim of identifying unifying trends and relationships among various experimental conditions. The mid-level focus of this dissertation was to explicitly avoid seeking low-level trends that are only applicable within a narrow subset of laser ablation research and high-level insights that are not of practical utility. To that end, four experiments were performed, sampling many orders of magnitude in laser parameters (28 ps to 300 μs in pulse duration, 3 J/cm^2 to 25 kJ/cm^2 in fluence), material properties (thermal diffusivity from 0.07-0.9 m^2/s, absorption coefficient from $10-10^6$ cm^{-1}), and environmental conditions (background pressure from $10^{-6}-760$ Torr, sample temperature from $77-700$ K). Numerical simulations were also performed in DEIVI, providing insight to experimental data by revealing the numerous physical processes at work.

In Chapter 3, aluminum, silicon, titanium, germanium, and indium antimonide were ablated at 1064 nm in ambient laboratory air with pulse durations ranging from 100 picoseconds to 100 microseconds and characterized with optical and laser confocal microscopy. Highly focused spots of 10 μm produced fluences of 0.004-25 kJ/cm^2 and irradiances spanning 4×10^6-10^{14} W/cm^2. Single pulse hole depths range from 84 nm to 147 μm. A quasi-one dimensional thermal model established a set of non-dimensional variables for hole depth, fluence, and pulse duration. For pulse durations shorter than the radial diffusion time, the hole depth exceeded the thermal diffusion length, and for pulses longer than this critical time, holes much smaller than the thermal diffusion depth were produced. The greatest hole depth was achieved with the 1 μs pulse duration on all materials tested. This corresponds to the condition where the pulse duration is comparable to the radial thermal diffusion time. For all pulse durations, and all

fluences above approximately 100 times the ablation threshold for each material, hole depth scaled approximately as fluence to 0.3-0.4 power. The power-law exponent is inversely proportional to the shielding of the laser pulse by ejected material, and shielding was maximized between 1 and 100 ns pulse duration for each material. Using the thermal scaling variables, the asymptotic crater depth behavior can be described independent of specific materials.

In Chapter 4, the quasi-one dimensional model developed in Chapter 3 was extended to shorter pulse durations, as well as lower background pressures and multimode beams. Low transverse order Gaussian beams at 1064 nm wavelength and 28 ps pulse duration were used to ablate Al, Si, Ti, Ge, and Insb in air, and Ge in vacuum. Crater depths and volumes, as well as volume of material above the surface were measured using a laser confocal microscope. Crater depths were found to plateau with increasing fluence on each material, and crater depths on Ge in vacuum were slightly higher than in air. Crater volume above and below the surface was found to increase linearly with fluence for all materials in air. In vacuum, the volume of material above the surface was less than in air, and increased at a lower rate with increasing fluence. The ratio of volume above the surface to volume below the surface was found to plateau for all materials to approximately 0.7 in air, and 0.4 for Ge in vacuum. The ablation efficiency, defined as atoms removed per incident photon was higher at low fluences, and decreased to approximately 0.004 for all materials at higher fluences.

Simulations using the Directed Energy Illumination Visualization tool showed that bulk melt flow out of the crater caused by the evaporation recoil pressure dominated at higher fluences. Plateauing of crater depth with fluence was caused by melt re-flow into the crater, which effects smaller crater widths more than larger ones, as evidenced by comparing multi-mode results to TEM_{00} simulations. Recondensation of evaporated material was identified as the main difference between craters formed in air versus vac-

uum, and the Knudsen layer jump conditions in DEIVI were modified to account for an estimated ≈ 20% recondensation rate. The simulations showed a resulting reduction in evaporation, which created less recoil pressure, driving less melt out of the crater. Higher resolution simulations and additional experimental data comparing different order modes are needed to further explore the effects of diverse spatial fluence distributions.

In addition to the laser damage experiments in Chapter 3 and 4, optical emission spectroscopy of the plume of ablated material was also studied. The long pulse ablation of aluminum and titanium wafers in ambient air using an Er:YAG laser at 2.94 μm wavelength was performed, and s=visible emission spectra collected during ablation showed molecular electronic transitions of AlO and TiO, respectively. For AlO, the spectra is assigned to the $B^2\Sigma^+ \rightarrow X^2\Sigma^+$ molecular electronic transition. A rovibronic model including self-absorption within the plume was developed to determine the molecular temperature, and a temperature of approximately 3000 K was found from fitting the model to the observed spectra. A greybody background, with an emissivity of approximately 1.3×10^{-6} was observed, implying a low volume mixing fraction of particulates in the plume.

TiO spectra were measured in the wavelength range of 500 nm to 750 nm, and molecular signatures included bands of the $C^3\Delta \rightarrow X^3\Delta\ \alpha$, $B^3\Pi \rightarrow X^3\Delta\ \gamma'$, and $A^3\Phi \rightarrow X^3\Delta\ \gamma$ transitions. The blackbody background signal was found to have a temperature between 2350 K and 2600 K from 1 to 1000 mTorr background pressure. With background pressures $P = 200 - 1000$ mTorr the total spectrally integrated emission intensity scaled as $P^{1/3}$. The spatially and temporally averaged spectra appear to be in qualitative agreement with previous temporally resolved studies that employed shorter wavelengths and shorter pulse durations than utilized in this work. Simulations in DEIVI show that peak temperature and pressure in the plume are not sufficient to create significant atomic and

ionic emissions seen in such other studies. A peak temperature of approximately 4000 K is inline with molecular temperatures at long time delays as measured by Parigger and Giacomo.

The molecular electronic emissions from both AlO and TiO dominate the spatially and temporally averaged signals. In both cases, there is little or no evidence of atomic or ionic emissions, which are prevalent in ablation at shorter wavelengths and shorter pulse durations (i.e. higher irradiance). In both experiments, the temperature inferred from the spectra is similar to the long term plume temperature (e.g. after approximately 50 μs of propagation) from other studies, implying that by the time the plume thermalizes and molecular formation occurs, the exact nature of the ablation process is unimportant. It is concluded that in the present experiments, the combination of longer wavelength and lower irradiance produces a shock front that is dramatically weaker than in traditional experiments. This explains the absence of atomic and ionic emissions, as well as the molecular temperature being so close to the vaporization temperature for each material studied.

In terms of the non-dimensional scaling variables introduced in Chapter 3, the subsequent experiments can be interpreted in a common framework. The key ablation criteria found between 100 ps and 100 μs at 1064 nm in air using a TEM_{00} mode was $f^* >> 1$ and $t^* << 1$ lead to $h^* > 1$. Using higher-order Gaussian modes at a pulse duration of 28 ps, this criteria was again observed, and it was found that the higher modality of the incident beam decreased the exponent of the power-law fit to crater depth versus fluence. The resulting shielding parameter was comparable to that seen at 100 ps, implying that the scaling variables still work down to 28 ps, which is near the threshold for applicability of a thermal description of ablation. It is concluded that for a constant fluence (well above threshold), as t^* decreases, h^* increases, and the slope of the h^* versus f^* line is a function of laser beam mode structure.

The long-pulse mid-IR ablation of Al and Ti can also be interpreted in terms of the non-dimensional variables. For both cases, $f^* \approx 1$ and thus significant mass removal was not expected. The observed spectra can then be interpreted in this context as well: $f^* >> 1$ and $t^* << 1$ are also necessary conditions for creation of a strong shock front. Mass removal and spectroscopic signal attributes are undoubtedly related, but the novel conclusion here is that the same simple 1-dimensional thermal scaling of laser and material parameters provides a framework to interpret spectroscopic data as well as crater formation.

There is still much work to be done in order to fully populate the space of potential scaling variables, trends, and heuristics across relevant regimes in laser ablation. However, this dissertation provides a robust starting point for laser ablation researchers looking to: 1) optimize laser damage effects (either minimize or maximize), 2) compare laser damage experiments on different materials at different wavelengths, or 3) build intuition on what to expect before starting an experiment under an entirely different set of conditions. The next section includes a recommendation of additional experimental and theoretical works.

7.2 Way Forward

Perhaps the most accessible and important next step is high-resolution DEIVI simulations of the cases in Chapter 3. Computational limitations and run time constraints precluded doing so in this dissertation. However, it is expected that significant insight would be gained, as it was in the much more limited scope of Chapter 4. In that same light, additional DEIVI simulations of the long pulse mid-infrared ablation of metals would potentially make up for the lack of spatially and temporally-resolved emission spectroscopy data. A simple chemical kinetics models could be integrated into DEIVI, since the code already spatially and temporally tracks the number density of species

in the plume. Again using DEIVI, simulations of additional non-TEM_{00} fluence distributions could strengthen the conclusions drawn in Chapter 4. Additional wavelengths should be modeled in DEIVI, seeing that it is significantly easier than finding (functioning) lasers at wavelengths of interest.

As for experiments, damage testing of more materials in the same experimental apparatus (preferably the same one as Chapter 3, or at least as close as feasible) would help validate and verify the thermal scaling variables. For example, thermal diffusivity is a key factor in the non-dimensional scaling variables, so materials with higher (e.g. copper, gold, or carbon) and lower (e.g. inconel or silicon dioxide) values than the present study should be investigated. Extremely fine steps in fluence, background pressure, and sample temperature would dramatically increase the accuracy of the insights drawn in Chapters 3 and 4.

Finally, hundreds of incredibly high-resolution optical and laser confocal microscopy images are available for quantitative analysis. Chapter 4 provided a small preview of the level of detail in these images, and there is still much more that could be learned. Splatter and other crater features can be studied using numerous image processing techniques (such as histogram of oriented gradients) and machine learning tools (such as stacked sparse autoencoders). The material samples from Chapters 3 and 4 could also be analyzed using surface-enhanced Raman spectroscopy to investigate phase changes during ablation (e.g. formation of amorphous silicon). There is clearly no shortage of ideas for additional studies, and it is the sincere hope of the author that this dissertation provides a useful contribution to the future of laser ablation research.

Bibliography

1. D. Bauerle, *Laser Processing and Chemistry*. Springer, 2nd ed., 2011.

2. M. Stafe, A. Marcu, and N. N. Puscas, *Pulsed Laser Ablation of Solids*, vol. 53 of *Springer Series in Surface Sciences*. Berlin: Springer, 2014.

3. A. E. Hussein, P. K. Diwakar, S. S. Harilal, and A. Hassanein, "The role of laser wavelength on plasma generation and expansion of ablation plumes in air," *Journal of Applied Physics*, vol. 113, no. 14, p. 143305, 2013.

4. N. Bulgakova, A. Bulgakov, and L. Babich, "Energy balance of pulsed laser ablation: thermal model revised," *Applied Physics A*, vol. 79, pp. 1323–1326, Sep 2004.

5. W. Bauer, G. Perram, and T. Haugan, "Plume dynamics from uv pulsed ablation of al and ti," in *Laser-Induced Damage in Optical Materials 2016*, vol. 10014, p. 100140S, International Society for Optics and Photonics, 2016.

6. S. S. Mao, X. Mao, R. Greif, and R. E. Russo, "Initiation of an early-stage plasma during picosecond laser ablation of solids," *Applied Physics Letters*, vol. 77, pp. 2464–2466, Oct 2000.

7. X. Wang, Z. H. Shen, J. Lu, and X. W. Ni, "Laser-induced damage threshold of silicon in millisecond, nanosecond, and picosecond regimes," *Journal of Applied Physics*, vol. 108, no. 3, p. 033103, 2010.

8. D. A. Cremers and L. J. Radziemski, *Handbook of Laser-Induced Breakdown Spectroscopy: Second Edition*. Wiley, 03 2013.

9. A. C. Woods, C. G. Parigger, and J. O. Hornkohl, "Measurement and analysis of titanium monoxide spectra in laser-induced plasma," *Opt. Lett.*, vol. 37, pp. 5139–5141, Dec 2012.

10. J. Lam, V. Motto-Ros, D. Misiak, C. Dujardin, G. Ledoux, and D. Amans, "Investigation of local thermodynamic equilibrium in laser-induced plasmas: Measurements of rotational and excitation temperatures at long time scales," *Spectrochimica Acta Part B: Atomic Spectroscopy*, vol. 101, pp. 86 – 92, 2014.

11. X. Bai, V. Motto-Ros, W. Lei, L. Zheng, and J. Yu, "Experimental determination of the temperature range of AlO molecular emission in laser-induced aluminum plasma in air," *Spectrochimica Acta Part B: Atomic Spectroscopy*, vol. 99, no. Supplement C, pp. 193 – 200, 2014.

12. C. J. Druffner, G. P. Perram, and R. R. Biggers, "Time-of-flight emission profiles of the entire plume using fast imaging during pulsed laser deposition of $YBa_2Cu_3O_{7-x}$," *Review of Scientific Instruments*, vol. 76, no. 9, p. 093101, 2005.

13. C. Phelps, C. J. Druffner, G. P. Perram, and R. R. Biggers, "Shock front dynamics in the pulsed laser deposition of $YBa_2Cu_3O_{7-x}$," *Journal of Physics D: Applied Physics*, vol. 40, pp. 4447–4453, jul 2007.

14. W. Bauer, G. P. Perram, and T. Haugan, "Comparison of plume dynamics for laser ablated metals: Al and Ti," *Journal of Applied Physics*, vol. 123, no. 9, p. 095304, 2018.

15. C. J. Knight, "Theoretical modeling of rapid surface vaporization with back pressure," *AIAA journal*, vol. 17, no. 5, pp. 519–523, 1979.

16. J. I. Pankove, *Optical Processes in Semiconductors*. Dover Publications, Inc., 1971.

17. J. R. Meyer, F. J. Bartoli, and M. R. Kruer, "Optical heating in semiconductors," *Phys. Rev. B*, vol. 21, pp. 1559–1568, Feb 1980.

18. J. T. Verdeyen, *Laser Electronics*. Prentice Hall, 1995.

19. J. Meister, C. Apel, R. Franzen, and N. Gutknecht, "Influence of the spatial beam profile on hard tissue ablation Part I: Multimode emitting Er:YAG lasers," *Lasers in Medical Science*, vol. 18, pp. 112–118, May 2003.

20. J. F. Ready, *Effects of High-Power Laser Radiation*. New York: Academic Press, 1971.

21. W. H. Carter, "Spot size and divergence for hermite gaussian beams of any order," *Applied optics*, vol. 19, no. 7, pp. 1027–1029, 1980.

22. V. Lednev, S. M. Pershin, and A. F. Bunkin, "Laser beam profile influence on libs analytical capabilities: single vs. multimode beam," *Journal of Analytical Atomic Spectrometry*, vol. 25, no. 11, p. 1745, 2010.

23. S. Bardy, B. Aubert, L. Berthe, P. Combis, D. Hébert, E. Lescoute, J.-L. Rullier, and L. Videau, "Numerical study of laser ablation on aluminum for shock-wave applications: development of a suitable model by comparison with recent experiments," *Optical Engineering*, vol. 56, no. 1, p. 011014, 2016.

24. D. Chrisey and G. Huber, *Pulsed Laser Deposition of Thin Films*. Hoboken: John Wiley & Sons Inc., 1994.

25. J. Zhang, H. Jiao, B. Ma, Z. Wang, and X. Cheng, "Laser-induced damage of nodular defects in dielectric multilayer coatings," *Optical Engineering*, vol. 57, no. 12, p. 121909, 2018.

26. A. M. Rubenchik, I. A. Vaseva, M. P. Fedoruk, and S. K. Turitsyn, "Laser space debris cleaning: elimination of detrimental self-focusing effects," *Optical Engineering*, vol. 58, no. 1, p. 011003, 2018.

27. C. Li, Y. Zhao, Y. Cui, X. Peng, C. Shan, M. Zhu, J. Wang, and J. Shao, "Comparison of 355-nm nanosecond and 1064-nm picosecond laser-induced damage in high-reflective coatings," *Optical Engineering*, vol. 57, no. 12, pp. 1 – 6 – 6, 2018.

28. W. Marine, N. M. Bulgakova, L. Patrone, and I. Ozerov, "Insight into electronic mechanisms of nanosecond-laser ablation of silicon," *Journal of Applied Physics*, vol. 103, no. 9, p. 094902, 2008.

29. D. Karnakis, "High power single-shot laser ablation of silicon with nanosecond 355nm," *Applied Surface Science*, vol. 252, no. 22, pp. 7823 – 7825, 2006.

30. J. H. Yoo, S. H. Jeong, R. Greif, and R. E. Russo, "Explosive change in crater properties during high power nanosecond laser ablation of silicon," *Journal of Applied Physics*, vol. 88, no. 3, pp. 1638–1649, 2000.

31. C. Porneala and D. A. Willis, "Time-resolved dynamics of nanosecond laser-induced phase explosion," *Journal of Physics D: Applied Physics*, vol. 42, no. 15, p. 155503, 2009.

32. A. H. A. Lutey, "An improved model for nanosecond pulsed laser ablation of metals," *Journal of Applied Physics*, vol. 114, no. 8, p. 083108, 2013.

33. Y. Zhang, D. Zhang, J. Wu, Z. He, and X. Deng, "A thermal model for nanosecond pulsed laser ablation of aluminum," *AIP Advances*, vol. 7, no. 7, p. 075010, 2017.

34. N. Bulgakova and A. Bulgakov, "Pulsed laser ablation of solids: transition from normal vaporization to phase explosion," *Applied Physics A*, vol. 73, pp. 199–208, Aug 2001.

35. Y. Zhou, B. Wu, S. Tao, A. Forsman, and Y. Gao, "Physical mechanism of silicon ablation with long nanosecond laser pulses at 1064nm through time-resolved observation," *Applied Surface Science*, vol. 257, no. 7, pp. 2886 – 2890, 2011.

36. A. S. et. al., "Experimental investigations of laser ablation efficiency of pure metals with femto, pico, and nanosecond pulses," *Applied Surface Science*, vol. 138, pp. 311–314, 1999.

37. S. Çelen, "On mechanism of explosive boiling in nanosecond regime," *Applied Physics B*, vol. 122, p. 168, Jun 2016.

38. C. Sawyer, K. Iyer, X. Zhu, M. Kelly, D. Luke, and D. Amdahl, "Two-dimensional laser-induced thermal ablation modeling with integrated melt flow and vapor dynamics," *Journal of Laser Applications*, vol. 29, no. 2, p. 022212, 2017.

39. D. M. Surmick, *Aluminum Monoxide Emission Measurements Following Laser-Induced Breakdown for Plasma Characterization*. PhD thesis, University of Tennessee, 2014.

40. I. G. Dors, C. Parigger, and J. W. L. Lewis, "Spectroscopic temperature determination of aluminum monoxide in laser ablation with 266-nm radiation," *Opt. Lett.*, vol. 23, pp. 1778–1780, Nov 1998.

41. C. G. Parigger, A. C. Woods, A. Keszler, L. Nemes, and J. O. Hornkohl, "Titanium monoxide spectroscopy following laser-induced optical breakdown," *AIP Conference Proceedings*, vol. 1464, no. 1, pp. 628–639, 2012.

42. J. R. Meyer, M. R. Kruer, and F. J. Bartoli, "Optical heating in semiconductors: Laser damage in Ge, Si, InSb, and GaAs," *Journal of Applied Physics*, vol. 51, no. 10, pp. 5513–5522, 1980.

43. M. N. Slipchenko, J. D. Miller, S. Roy, J. R. Gord, and T. R. Meyer, "All-diode-pumped quasi-continuous burst-mode laser for extended high-speed planar imaging," *Opt. Express*, vol. 21, pp. 681–689, Jan 2013.

44. K.-H. Leitz, B. Redlingshöfer, Y. Reg, A. Otto, and M. Schmidt, "Metal ablation with short and ultrashort laser pulses," *Physics Procedia*, vol. 12, pp. 230 – 238, 2011.

45. M. M. Martynyuk, "Phase explosion of a metastable fluid," *Translated from Fizika Goreniya i Vzryva*, vol. 13, no. 2, pp. 213–229, 1977.

46. H. Carslaw and J. C. Jaegar, *Conduction of Heat in Solids*. New York: Oxford University Press, 2000.

47. G. Jellison Jr and D. Lowndes, "Optical absorption coefficient of silicon at 1.152 μm at elevated temperatures," *Applied Physics Letters*, vol. 41, no. 7, pp. 594–596, 1982.

48. B. N. Chichkov, C. Momma, S. Nolte, F. von Alvensleben, and A. Tünnermann, "Femtosecond, picosecond and nanosecond laser ablation of solids," *Applied Physics A*, vol. 63, pp. 109–115, Aug 1996.

49. B. Salle, O. Gobert, P. Meynadier, M. Perdrix, G. Petite, and A. Semerok, "Femtosecond and picosecond laser microablation: ablation efficiency and laser microplasma expansion," *Applied Physics A*, vol. 69, pp. S381–S383, Dec 1999.

50. L. V. Zhigilei and B. J. Garrison, "Microscopic mechanisms of laser ablation of organic solids in the thermal and stress confinement irradiation regimes," *Journal of Applied Physics*, vol. 88, no. 3, pp. 1281–1298, 2000.

51. L. Zhigilei, "Dynamics of the plume formation and parameters of the ejected clusters in short-pulse laser ablation," *Applied Physics A: Materials Science & Processing*, vol. 76, pp. 339–350, Mar 2003.

52. P. Lorazo, L. J. Lewis, and M. Meunier, "Thermodynamic pathways to melting, ablation, and solidification in absorbing solids under pulsed laser irradiation," *Physical Review B*, vol. 73, no. 13, p. 134108, 2006.

53. Z. Kuang, W. Perrie, D. Liu, S. Edwardson, J. Cheng, G. Dearden, and K. Watkins, "Diffractive multi-beam surface micro-processing using 10ps laser pulses," *Applied Surface Science*, vol. 255, pp. 9040–9044, Aug 2009.

54. G. Zhu, D. Whitehead, W. Perrie, O. Allegre, V. Olle, Q. Li, Y. Tang, K. Dawson, Y. Jin, S. Edwardson, L. Li, and G. Dearden, "Thermal and optical performance characteristics of a spatial light modulator with high average power picosecond laser exposure applied to materials processing applications," *Procedia CIRP*, vol. 74, pp. 594 – 597, 2018. 10th CIRP Conference on Photonic Technologies [LANE 2018].

55. J. M. Vadillo, C. C. García, S. Palanco, and J. J. Laserna, "Nanometric range depth-resolved analysis of coated-steels using laser-induced breakdown spectrometry with a 308 nm collimated beam," *Journal of Analytical Atomic Spectrometry*, vol. 13, no. 8, pp. 793–797, 1998.

56. L. Cabalín and J. Laserna, "Atomic emission spectroscopy of laser-induced plasmas generated with an annular-shaped laser beam," *Journal of Analytical Atomic Spectrometry*, vol. 19, no. 4, pp. 445–450, 2004.

57. B. Cordero, V. Gomez, A. E. Platero-Prats, M. Reves, J. Echeverría, E. Cremades, F. Barragán, and S. Alvarez, "Covalent radii revisited," *Dalton Trans.*, pp. 2832–2838, 2008.

58. A. D. Rakić, "Algorithm for the determination of intrinsic optical constants of metal films: application to aluminum," *Appl. Opt.*, vol. 34, pp. 4755–4767, Aug 1995.

59. C. Schinke, P. Christian Peest, J. Schmidt, R. Brendel, K. Bothe, M. R. Vogt, I. Kroger, S. Winter, A. Schirmacher, S. Lim, H. T. Nguyen, and D. MacDonald, "Uncertainty analysis for the coefficient of band-to-band absorption of crystalline silicon," *AIP Advances*, vol. 5, no. 6, p. 067168, 2015.

60. P. B. Johnson and R. W. Christy, "Optical constants of transition metals: Ti, V, Cr, Mn, Fe, Co, Ni, and Pd," *Phys. Rev. B*, vol. 9, pp. 5056–5070, Jun 1974.

61. W. Dash and R. Newman, "Intrinsic optical absorption in single-crystal germanium and silicon at 77 k and 300 k," *Physical review*, vol. 99, no. 4, p. 1151, 1955.

62. Y. Zhang, "Corrected values for boiling points and enthalpies of vaporization of elements in handbooks," *Journal of Chemical & Engineering Data*, vol. 56, 01 2011.

63. J. A. Dean, *Lange's handbook of chemistry*. New york; London: McGraw-Hill, Inc., 1999.

64. N. Arnold, J. Gruber, and J. Heitz, "Spherical expansion of the vapor plume into ambient gas: an analytical model," *Applied Physics A*, vol. 69, pp. S87–S93, Dec 1999.

65. C. J. Knight, "Transient vaporization from a surface into vacuum," *AIAA Journal*, vol. 20, no. 7, pp. 950–954, 1982.

66. S. Anisimov, "Vaporization of metal absorbing laser radiation," in *30 Years Of The Landau Institute - Selected Papers*, pp. 14–15, World Scientific, 1996.

67. J. Ho, C. Grigoropoulos, and J. Humphrey, "Computational study of heat transfer and gas dynamics in the pulsed laser evaporation of metals," *Journal of Applied Physics*, vol. 78, no. 7, pp. 4696–4709, 1995.

68. J. Ho, C. Grigoropoulos, and J. Humphrey, "Gas dynamics and radiation heat transfer in the vapor plume produced by pulsed laser irradiation of aluminum," *Journal of Applied Physics*, vol. 79, no. 9, pp. 7205–7215, 1996.

69. A. Chatterjee, M. E. Decoster, A. M. Mark, X. Zhu, and K. A. Iyer, "Directed energy illumination visualization (DEIVI) physics-based laser ablation models and software user manual version 3.2," tech. rep., The Johns Hopkins University Applied Physics Laboratory, Laurel MD, 2018.

70. M. Leitner, T. Leitner, A. Schmon, K. Aziz, and G. Pottlacher, "Thermophysical properties of liquid aluminum," *Metallurgical and Materials Transactions A*, vol. 48, no. 6, pp. 3036–3045, 2017.

71. M. J. Assael, K. Kakosimos, R. M. Banish, J. Brillo, I. Egry, R. Brooks, P. N. Quested, K. C. Mills, A. Nagashima, Y. Sato, *et al.*, "Reference data for the density and viscosity of liquid aluminum and liquid iron," *Journal of physical and chemical reference data*, vol. 35, no. 1, pp. 285–300, 2006.

72. S. Nakamura and T. Hibiya, "Thermophysical properties data on molten semiconductors," *International Journal of Thermophysics*, vol. 13, pp. 1061–1084, Nov 1992.

73. P.-F. Paradis, T. Ishikawa, and S. Yoda, "Non-contact measurements of surface tension and viscosity of niobium, zirconium, and titanium using an electrostatic levitation furnace," *International journal of thermophysics*, vol. 23, no. 3, pp. 825–842, 2002.

74. P.-F. Paradis and W.-K. Rhim, "Non-contact measurements of thermophysical properties of titanium at high temperature," *The Journal of Chemical Thermodynamics*, vol. 32, no. 1, pp. 123–133, 2000.

75. Y. Sato, T. Nishizuka, T. Takamizawa, T. Yamamura, and Y. Waseda, "Viscosity of molten GaSb and InSb," *International journal of thermophysics*, vol. 23, no. 1, pp. 235–243, 2002.

76. A. Miotello, A. Peterlongo, and R. Kelly, "Laser-pulse sputtering of aluminium: gas-dynamic effects with recondensation and reflection conditions at the knudsen layer," *Nuclear Instruments and Methods in Physics Research Section B: Beam Interactions with Materials and Atoms*, vol. 101, no. 1-2, pp. 148–155, 1995.

77. R. Kelly and A. Miotello, "Laser-pulse sputtering of atoms and molecules part ii. recondensation effects," *Nuclear Instruments and Methods in Physics Research Section B: Beam Interactions with Materials and Atoms*, vol. 91, no. 1-4, pp. 682–691, 1994.

78. C. R. Deckard, "Selective laser sintering," Master's thesis, University of Texas at Austin, December 1988.

79. S. S. Harilal, C. V. Bindhu, M. S. Tillack, F. Najmabadi, and A. C. Gaeris, "Internal structure and expansion dynamics of laser ablation plumes into ambient gases," *Journal of Applied Physics*, vol. 93, no. 5, pp. 2380–2388, 2003.

80. K. Kasatani, H. Higashide, H. Shinohara, and H. Sato, "Chemiluminescent reactions studied by laser ablation. detection of AlO $B^2\Sigma^+$ in the Al + O_2 system," *Chemical Physics Letters*, vol. 174, no. 1, pp. 71 – 74, 1990.

81. K. Hartig, B. Brumfield, M. Phillips, and S. Harilal, "Impact of oxygen chemistry on the emission and fluorescence spectroscopy of laser ablation plumes," *Spectrochimica Acta Part B: Atomic Spectroscopy*, vol. 135, pp. 54 – 62, 2017.

82. C. G. Parigger and J. O. Hornkohl, "Computation of the *AlO* $B^2\Sigma^+ \rightarrow X^2\Sigma^+$ emission spectra," *Spectrochimica Acta Part A: Molecular and Biomolecular Spectroscopy*, vol. 81, no. 1, pp. 404 – 411, 2011.

83. O. Varenne, P.-G. Fournier, J. Fournier, B. Bellaoui, A.-I. Faké, J. Rostas, and G. Taieb, "Internal population distribution of the B state of AlO formed by fast ion beam bombardment or laser ablation of an Al_2O_3 (Al) surface," *Nuclear Instruments and Methods in Physics Research Section B: Beam Interactions with Materials and Atoms*, vol. 171, no. 3, pp. 259 – 276, 2000.

84. A. D. Giacomo and J. Hermann, "Laser-induced plasma emission: from atomic to molecular spectra," *Journal of Physics D: Applied Physics*, vol. 50, no. 18, p. 183002, 2017.

85. K. Huber and G. Herzberg, *NIST Chemistry WebBook, NIST Standard Reference Database Number 69, Eds. P.J. Linstrom and W.G. Mallard*, ch. Constants of Diatomic Molecules (data prepared by J.W. Gallagher and R.D. Johnson, III). Gaithersberg MD, 20899: National Institute of Science and Technology, (retrieved October 9, 2017) 2017.

86. A. T. Patrascu, C. Hill, J. Tennyson, and S. N. Yurchenko, "Study of the electronic and rovibronic structure of the $X^2\Sigma^+$, $A^2\Pi$, and $B^2\Sigma^+$ states of AlO," *The Journal of Chemical Physics*, vol. 141, no. 14, p. 144312, 2014.

87. A. T. Patrascu, S. N. Yurchenko, and J. Tennyson, "Exomol molecular line lists - IX. the spectrum of AlO," *Monthly Notices of the Royal Astronomical Society*, vol. 449, no. 4, pp. 3613–3619, 2015.

88. G. Herzberg, *Molecular Spectra and Molecular Structure Vol 1 - Spectra of Diatomic Molecules*. Malabar, Florida: Krieger Publishing Company, second ed., 1989.

89. H. Liszt and W. Smith, "RKR Franck-Condon factors for blue and ultraviolet transitions of some molecules of astrophysical interest and some comments on the interstellar abundance of CH, CH+ and SiH+," *Journal of Quantitative Spectroscopy and Radiative Transfer*, vol. 12, no. 5, pp. 947 – 958, 1972.

90. P. F. Bernath, *Spectra of Atoms and Molecules*. Oxford University Press, second ed., 2005.

91. H. Partridge, S. R. Langhoff, B. Lengsfield III, and B. Liu, "Theoretical study of the alo blue-green ($B^2\Sigma^+ \rightarrow X^2\Sigma^+$ band system," *Journal of Quantitative Spectroscopy and Radiative Transfer*, vol. 30, no. 5, pp. 449–462, 1983.

92. J. Arnold, E. Whiting, and G. Lyle, "Line by line calculation of spectra from diatomic molecules and atoms assuming a voigt line profile," *Journal of Quantitative Spectroscopy and Radiative Transfer*, vol. 9, no. 6, pp. 775 – 798, 1969.

93. C. G. Parigger, A. C. Woods, D. M. Surmick, A. Donaldson, and J. L. Height, "Aluminum flame temperature measurements in solid propellant combustion," *Applied Spectroscopy*, vol. 68, no. 3, pp. 362–366, 2014. PMID: 24666953.

94. J. T. Yardley, *Introduction to Molecular Energy Transfer*. Academic Press, 1980.

95. N. Cohen and K. R. Westberg, "Chemical kinetic data sheets for high temperature chemical reactions," *Journal of Physical and Chemical Reference Data*, vol. 12, no. 3, pp. 531–590, 1983.

96. A. Salzberg, D. I. Santiago, F. Asmar, D. N. Sandoval, and B. R. Weiner, "Collision-induced electronic quenching of aluminum monoxide," *Chemical Physics Letters*, vol. 180, no. 3, pp. 161 – 167, 1991.

97. A. Christy, "Quantum analysis of the blue-green bands of titanium oxide," *Physical Review*, vol. 33, no. 5, p. 701, 1929.

98. C. N. Kei-ichi, H. Saitoh, and H. Ito, "The electronic transition moment function for the $C^3\Delta \rightarrow X^3\Delta$ system of TiO," *Journal of Molecular Spectroscopy*, vol. 226, no. 1, pp. 87–94, 2004.

99. K. Lodders, "Titanium and vanadium chemistry in low-mass dwarf stars," *The Astrophysical Journal*, vol. 577, no. 2, p. 974, 2002.

100. B. Krupp, J. Collins, and H. Johnson, "The effects of TiO opacity on the atmospheric structure of cool stars," *The Astrophysical Journal*, vol. 219, pp. 963–969, 1978.

101. U. G. Jorgensen, "Effects of TiO in stellar atmospheres," *Astronomy and Astrophysics*, vol. 284, pp. 179–186, 1994.

102. A. D. Giacomo, M. Dell'Aglio, A. Santagata, and R. Teghil, "Early stage emission spectroscopy study of metallic titanium plasma induced in air by femtosecond- and nanosecond-laser pulses," *Spectrochimica Acta Part B: Atomic Spectroscopy*, vol. 60, no. 7, pp. 935 – 947, 2005. Laser Induced Plasma Spectroscopy and Applications (LIBS 2004) Third International Conference.

103. T. A. V. Woerkom, G. P. Perram, B. D. Dolasinski, P. A. Berry, and C. D. Phelps, "Visible aluminum monoxide emission during long pulse mid-infrared ablation of aluminum in air," *J. Opt. Soc. Am. B*, vol. 35, pp. B54–B61, Oct 2018.

104. S. R. Langhoff, "Theoretical study of the spectroscopy of TiO," *The Astrophysical Journal*, vol. 481, no. 2, p. 1007, 1997.

105. S. P. Davis, J. Littleton, and J. G. Phillips, "Transition rates for the TiO β, δ, ϕ, γ', γ, and α systems," *The Astrophysical Journal*, vol. 309, pp. 449–454, 1986.

106. M. L. Campbell and R. E. McClean, "Kinetics of neutral transition-metal atoms in the gas phase: oxidation reactions of titanium (a^3F) from 300 to 600 k," *The Journal of Physical Chemistry*, vol. 97, no. 30, pp. 7942–7946, 1993.

REPORT DOCUMENTATION PAGE

Form Approved
OMB No. 0704–0188

1. REPORT DATE *(DD–MM–YYYY)*	2. REPORT TYPE	3. DATES COVERED *(From — To)*
26–08–2019	PhD Dissertation	Oct 2014 — Aug 2019

4. TITLE AND SUBTITLE

ON THE PULSED ABLATION OF METALS AND SEMICONDUCTORS

5a. CONTRACT NUMBER

5b. GRANT NUMBER

5c. PROGRAM ELEMENT NUMBER

6. AUTHOR(S)

Todd A. Van Woerkom

5d. PROJECT NUMBER

5e. TASK NUMBER

5f. WORK UNIT NUMBER

7. PERFORMING ORGANIZATION NAME(S) AND ADDRESS(ES)

Air Force Institute of Technology
Graduate School of Engineering and Management (AFIT/EN)
2950 Hobson Way
WPAFB OH 45433-7765

8. PERFORMING ORGANIZATION REPORT NUMBER

AFIT-ENP-DS-19-S-030

9. SPONSORING / MONITORING AGENCY NAME(S) AND ADDRESS(ES)

Air Force Research Laboratory
2241 Avionics Circ.
WPAFB OH 45433
937-713-4256
charles.phelps@us.af.mil

10. SPONSOR/MONITOR'S ACRONYM(S)

AFRL/RY

11. SPONSOR/MONITOR'S REPORT NUMBER(S)

12. DISTRIBUTION / AVAILABILITY STATEMENT

DISTRIBUTION STATEMENT A:
APPROVED FOR PUBLIC RELEASE; DISTRIBUTION UNLIMITED.

13. SUPPLEMENTARY NOTES

14. ABSTRACT

This dissertation covers pulsed laser ablation of Al, Si, Ti, Ge, and InSb, with pulse durations from tens of picosecond to hundreds of microseconds, fluences from ones of J/cm^2 to over 10,000 J/cm^2, and in ambient air and vacuum. A set of non-dimensional scaling factors was created to interpret the data relative to the laser and material parameters, and it was found that pulse durations shorter than a critical timescale formed craters much larger than the thermal diffusion length, and longer pulse durations created holes much shallower than the thermal diffusion length. Low transverse order Gaussian beams with a pulse duration of 28 ps were used to ablate the materials in air and vacuum. It was found that plateauing of crater depth with increasing fluence was due to melt-reflow into the crater and recondensation of evaporated material. Long pulse mid-infrared ablation of aluminum and titanium in air was found to produce aluminum monoxide and titanium monoxide, respectively. The spectra were similar to those observed in ablation studies using shorter wavelength and higher irradiance lasers, despite the much weak shock front in the current study.

15. SUBJECT TERMS

Pulsed laser ablation, laser damage, laser confocal microscopy, optical emission spectra

16. SECURITY CLASSIFICATION OF:			17. LIMITATION OF ABSTRACT	18. NUMBER OF PAGES	19a. NAME OF RESPONSIBLE PERSON
a. REPORT	b. ABSTRACT	c. THIS PAGE			Dr. Glen Perram, AFIT/ENP
U	U	U	U	154	19b. TELEPHONE NUMBER *(include area code)* 937-255-3636 x4504